Stony Brook University

Breast Tomosynthesis with Amorphous Selenium Digital Flat Panel Detector

A Dissertation Presented

by

Bo Zhao

to

The Graduate School

in Partial Fulfillment of the Requirements

for the Degree of

Doctor of Philosophy

in

Biomedical Engineering

Stony Brook University

December 2007

Stony Brook University

The Graduate School

Bo Zhao

We, the dissertation committee for the above candidate for the

Doctor of Philosophy degree, hereby recommend

acceptance of this dissertation.

Wei Zhao, Ph.D., Dissertation Advisor
Associate Professor, Department of Radiology

Terry Button, Ph.D., Chairperson of the Defense
Associate Professor, Director of Radiology Technology Program, Department of Radiology

Gene Gindi, Ph.D.
Associate Professor, Department of Electrical & Computer Engineering and Radiology

Paul R. Fisher, M.D.
Clinical Associate Professor, Departments of Radiology and Surgery

This dissertation is accepted by the Graduate School

Lawrence Martin
Dean of the Graduate School

Abstract of the Dissertation

Breast Tomosynthesis with Amorphous Selenium Digital Flat Panel Detector

by

Bo Zhao

Doctor of Philosophy

in

Biomedical Engineering

Stony Brook University

2007

Screening mammography has become the most effective technique for early detection of breast cancer. A major limitation of conventional mammography is the overlapping breast structure that obscures the cancer lesion. Breast tomosynthesis, a three-dimensional (3-D) imaging technique, is a promising method to retrieve depth information. Recent developments in digital mammography make this advanced imaging method possible. In breast tomosynthesis, multiple projection images are acquired when the x-ray tube travels within a limited angular range, typically $< 50^{o}$. The projection images are reconstructed into tomographic slices that are parallel to the detector surface. To keep the total dose comparable to that used in mammography, only a fraction of the

conventional mammography exposure is delivered during swift acquisition of each view. The digital detector has to be able to produce high quality images at low exposure and high frame rate. Both the acquisition parameters and reconstruction algorithm will have a direct impact on reconstructed image quality.

The primary objective of this thesis is to investigate breast tomosynthesis from the physics point of view.

Firstly, since the detector for tomosynthesis is modified from that for mammography, the two-dimensional (2-D) imaging performance of the detector was optimized for breast tomosynthesis. The limiting factors that affect breast tomosynthesis were determined using an amorphous selenium (a-Se) Full Field Digital Mammography (FFDM) detector which was characterized at tomosynthesis exposure (as low as 1 mR) by measurement of the resolution and noise characteristics parameters including modulation transfer function (MTF), noise power spectrum (NPS), and detective quantum efficiency (DQE). The high frame rate as experienced in tomosynthesis poses a tremendous challenge to the temporal performance of the detector. The temporal imaging performance was investigated by measurement of the lag and ghosting properties of the detector. The measurement was also performed on a-Se samples in order to understand the inherent physics of lag and ghosting. We concluded that decreasing electronic noise and increasing the x-ray to charge conversion gain in the a-Se layer can be effective methods to improve the detector performance at very low exposures as experienced in tomosynthesis. Careful selection of operation conditions, i.e., electric field and proper reset procedure to clear the trapped charges in the a-Se layer will help improve the temporal performance of the detector.

Secondly, a 3-D cascaded linear system model was developed for breast tomosynthesis to investigate the effects of different imaging system parameters on the reconstructed image quality. The model was validated using linear system parameters of the 3-D NPS and in-plane presampling MTF measured on a prototype breast tomosynthesis system equipped with a-Se digital mammography detector. It was found that the model agreed well with measurement. An ACR phantom was imaged to investigate the effects of limited angular range and detector operational modes on reconstructed image quality. The image quality of the objects (mass and calcifications) on the phantom show good correlation with the quantitative measurement of NPS and MTF. We conclude that the model can be used to accurately predict the imaging performance for varied acquisition and system parameters and ultimately used for the optimization of breast tomosynthesis.

Table of Contents

List of Acronyms

1-D	One-Dimensional
2-D	Two-Dimensional
3-D	Three-Dimensional
Al	Aluminum
ADU	Analog-to-Digital Unit
a-Se	Amorphous selenium
ASF	Artifact Spread Function
BB	Ball-bearing bead
BKE	Background-Known-Exactly
CAD	Computer-aided Diagnosis
Cal	Calcifications
CBCT	Cone beam Computed Tomography
CNR	Contrast-to-Noise Ratio
COR	Center Of Rotation
CsI	Cesium Iodide
CT	Computed Tomography
DQE	Detective quantum efficiency
EHP	Electron hole pair
EM	Expectation maximization
ESF	Edge Spread Function
FBP	Filtered Backprojection

FFDM	Full Field Digital Mammography
FSB	Focal spot blur
FOM	figure of merit
HWHM	Half width at half maximum
IN	Interpolation (filter)
LSF	Line spread function
MASMIP	Molybdenum Anode Spectral Model using Interpolating Polynomials
Mo	Molybdenum
MTF	Modulation transfer function
NEQ	Noise equivalent quanta
NPS	Noise power spectrum
PSF	Point Spread Function
RA	Ramp (filter)
Rh	Rhodium
ROI	Region of interest
SA	Spectrum Apodization (filter)
SBP	Simple backprojection
SDNR	Signal Difference to Noise Ratio
SID	Source to imager distance
SNR	Signal-to-Noise Ratio
SSP	Slice sensitivity profile
ST	Slice thickness (filter)
TFT	Thin film transistor

VOI	Volume of interest
W	Tungsten

List of Figures

List of Tables

Acknowledgments

It is a pleasure to thank the many people who made this dissertation possible.

My deepest gratitude is to my advisor, Dr. Wei Zhao, who is my role model, for her wise advisement and continuous guidance on my Ph.D. research. She impressed me with her wide knowledge and insightful thoughts. Her understanding and encouragement have helped me overcome hardships encountered in both personal life and academic research. I learned a lot from her and I feel very fortunate to have her as my advisor.

I would also like to thank the other members of my Ph.D. committee for carefully reading my thesis and providing me with valuable comments on my thesis research: Dr. Terry Button, Dr. Paul Fisher and Dr. Gene Gindi. I thank Dr. Terry Button for his support, for listening and offering many suggestions and advices over the past six years. I thank Dr. Paul Fisher for many useful discussions and suggestions on my research, which inspired me a lot. I enjoyed working with him during our research collaboration. I thank Dr. Gene Gindi for bringing me to the exciting medical imaging field during the first year lab rotation in graduate school.

I thank our current and previous group members, Rick Lubinsky, Jennifer Segui, Dan Li, Joerg Lehnert, Yue-Houng Hu and Jun Zhou for the many helpful discussions on my research projects during our group meeting. I thank Joerg, Jenn and Hue-Houng for editing and proofreading this thesis. I wish to thank my labmate and close friend, Jenn, who was always beside me when I needed her opinions and supports. I thank my friends from work, Faith, Nand, Michael, Sachin, Mayuresh, Erin, Su, Lili, Dan, Santosh and Jing, who made my graduate school a pleasant one. I would like to thank my good friends

Lijun Shi, Minhong Cai, Fangmin He and Min Zhu for always being there for me during ups and downs of my life. I cherish the many years of friendship with them.

Finally I would like to express my deepest thanks to my family, mom, dad, brother, sister-in-law, my little nephew to be the sunshine of my life and motivations of my studies. Last but not the least I thank my boyfriend Shenglan for his love and for bringing peace to my heart and happiness to my life.

Chapter 1

INTRODUCTION

1.1 Breast imaging using x-ray

Breast cancer is the most common type of cancers and the second leading cause of cancer death for women in the U.S. According to the American Cancer Society[1], breast cancer is the most frequently diagnosed cancer in US women, with 178, 480 new cases of invasive caner and 62, 030 new case of in situ breast cancer are expected to occur during 2007. Approximately 40,000 deaths in women annually in the U.S. are due to breast cancer (only next to lung cancer). The causes of this disease are unknown, therefore early detection and treatment is the only method for reducing mortality from breast cancer. X-ray mammography, i.e., imaging a compressed breast with a low-energy x-ray beam, has been the standard screening method for early detection of breast cancer. Statistics show that on average, mammography can detect 80-90% of breast cancer in women without any symptoms. Sources have shown that mammography has reduced the mortality rate due to breast cancer by 20-30%[2].

1.2 Digital mammography

Conventional screen-film mammography has poor discrimination between breast tissues due to the limited dynamic range of the film. Fortunately, advanced digital mammography, in which traditional screen-film is replaced by a digital mammography detector, demonstrates the possibility of improved diagnosis[3]. There are two types of

detectors available for digital mammography which differ primarily in the method used for x-ray detection[4]. The *direct* detector uses a layer of photoconductor, usually amorphous selenium (a-Se), to convert x-ray photons to charges directly. The *indirect* detector has two conversion steps in x-ray detection: a scintillator (such as cesium iodide (CsI)) first converts x-rays to visible light photons, and then a photodiode converts light photons to charge. For both detectors, the spatial distribution of image charge (i.e. x-ray image) is read out with a thin film transistor (TFT) array[4].

1.3 A-Se digital mammography detector with TFT readout

Our research uses a direct conversion digital detector with a-Se. Shown in Figure 1.1 is the cross-sectional view of the structure. The detector is electroded on the top surface where x-rays enter the structure. The bottom surface of the a-Se is in contact with the TFT active matrix. Each pixel of the active matrix consists of a TFT switch array for image readout, a pixel electrode to collect image charge generated by a-Se, and a storage capacitor for holding the charge before readout. The charge is then read out in a self-scanned manner using the active matrix by turning on the TFTs one row at a time via a common gate line. The applied gate voltage switches on the TFT and permits the transfer of image charge from each pixel onto the data lines (perpendicular to gate line) which are connected to external charge amplifiers. A multiplexer converts the parallel amplified signal to a serial output for digitization[5, 6].

During image acquisition, the bias voltage is applied to the electrode on the top surface to establish an electric field. The bias voltage is either positive (Figure 1.1a) or negative (Figure 1.1b). When the x-ray photons interact with the a-Se layer, electron hole

pairs (EHP) are generated. The charges are separated by the applied electric field and travels toward the electrodes. In a positively biased detector as shown in Figure 1.1(a), the electrons move toward the top electrode and holes move toward bottom. Therefore the positive charge is readout by the TFT array. In a negatively biased detector as shown in Figure 1.1(b), the electrons move toward the bottom electrode and are read out by the TFT array. The magnitude and polarity of the high voltage applied across the detector will affect the performance of the detector as will be discussed in Chapter 3.

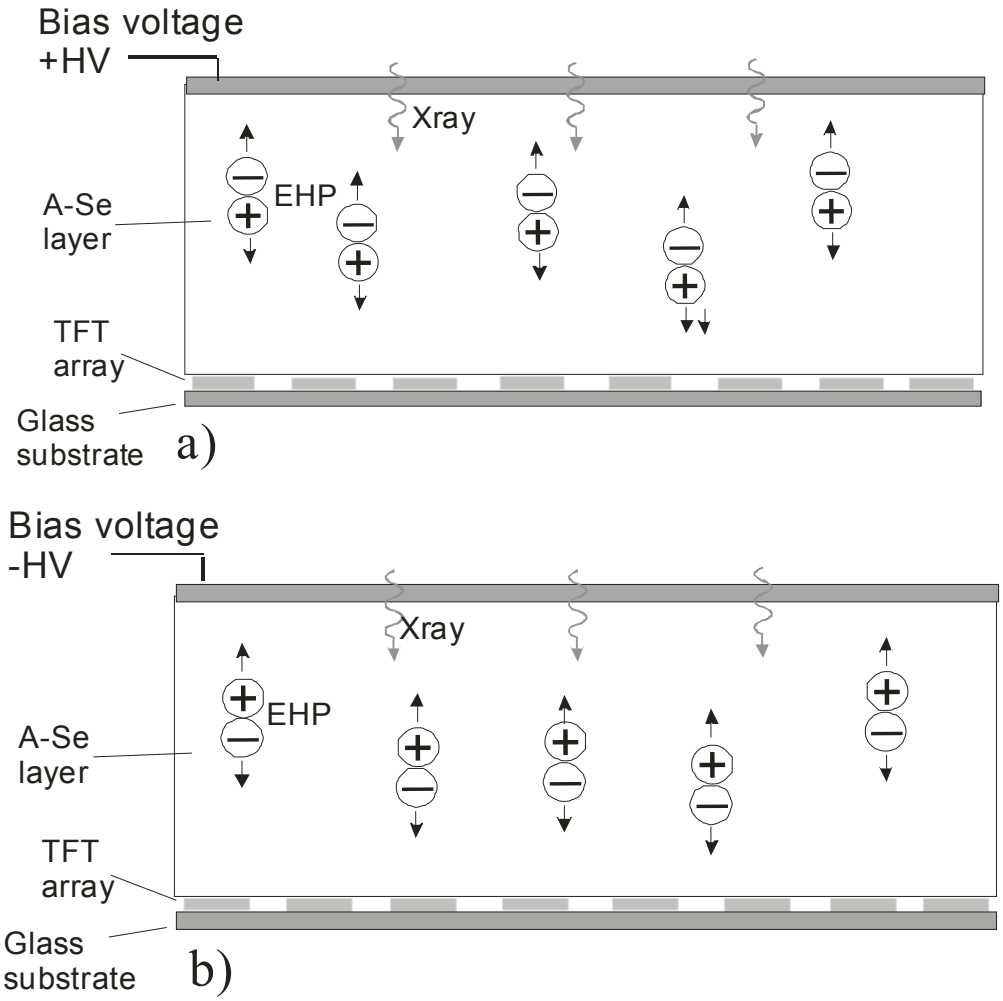

Figure 1.1, Cross-sectional view of the a-Se detector with a) positively biased, b) negatively biased high voltage

One advantage of the direct over the indirect approach is the higher inherent image resolution. Because charge travels along the electric field lines, there is hardly any lateral spreading during the migration toward the TFT array. In the indirect typed detector, the light created in the structured phosphor diffuses as it propagates to the TFT readout, which potentially causes image blurring.

1.4 Three dimensional breast imaging

Although digital mammography has resulted in significantly improved image quality compared with screen-film, there is evidence that 30% of breast cancers are missed in screening mammography especially for women with dense breasts or implants[7]. Breast cancer detection through screening mammography is largely limited by structural noise caused by superimposed breast tissue. A promising solution is three dimensional (3-D) imaging of the breast. Two types of 3-D breast imaging methods have been investigated: cone-beam computed tomography (CBCT)[8] and tomosynthesis[7]. The availability of flat panel imagers for digital mammography has made both techniques possible.

A proposed design for a breast CT system is illustrated in Figure 1.2[8]. The patient lies prone on the table, with breast hanging through a hole in the table. The positioning is similar to that in breast biopsy. During patient scanning, the breast is imaged by half-cone x-ray beams with the tube rotating 180 degrees. Each breast is imaged individually. The x-ray beam in breast CT is more penetrating than that in mammography since the uncompressed breast is much thicker. The digital detector used for acquiring the projection images is operated in fluoroscopy mode. The pixel size is usually a few times larger that that used in mammography.

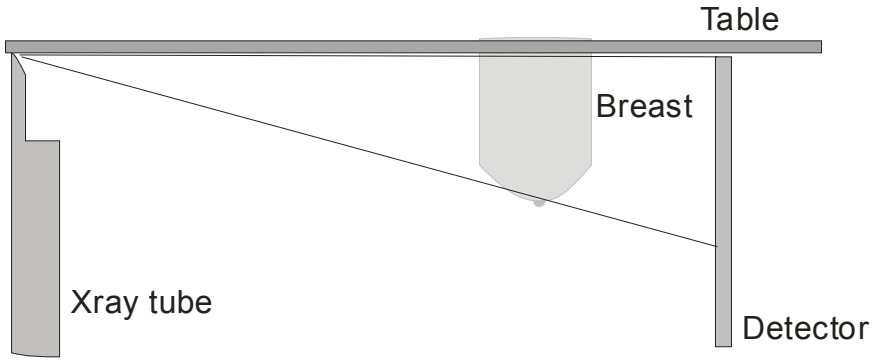

Figure 1.2, Diagram showing the geometry of the proposed breast CT system

Compared with tomosynthesis, CBCT reconstructs the breast into thinner slices, resulting in less structural noise. Since the digital detector in breast CT usually has large pixel size (for example, 300 μm x 300 μm), the image has better contrast. On the other hand, tomosynthesis uses a digital detector similar to those in mammography; therefore provides better in-plane spatial resolution although worse contrast resolution than CT. Optimum tradeoff between the two methods for clinical application remains to be studied. The study in this dissertation will focus on breast tomosynthesis.

1.5 Breast tomosynthesis

Breast tomosynthesis has a limited angle tomographic geometry and was first proposed by Niklason et al[9]. As shown in Figure 1.3, the breast tomosynthesis system is compatible with the existing mammography system. The breast is compressed and positioned using the same method as in screening mammography. The x-ray tube travels in an arc above the breast through a limited angular range and shoots several short pulses at different angles. In order to keep the total exposure equivalent to that used in mammography, only a fraction of the typical mammography dose is delivered for each view. The projection images acquired at different angles are then used for image reconstruction, which allows any cross-section plane of the breast parallel to the detector

to be reconstructed. This is a major advancement compared to projection mammography, in which no depth information is available. Studies have shown that breast tomosynthesis helps reduce the false-positive recall rate[7]. Breast tomosynthesis is especially beneficial for detection of large-area, low-contrast masses, which are always obscured by overlapping breast tissue in screening mammography. This is why breast tomosynthesis is a topic under intensive investigation and development by both research institutions and mammography equipment manufacturers for screening and diagnosis of breast cancer[7, 9, 10].

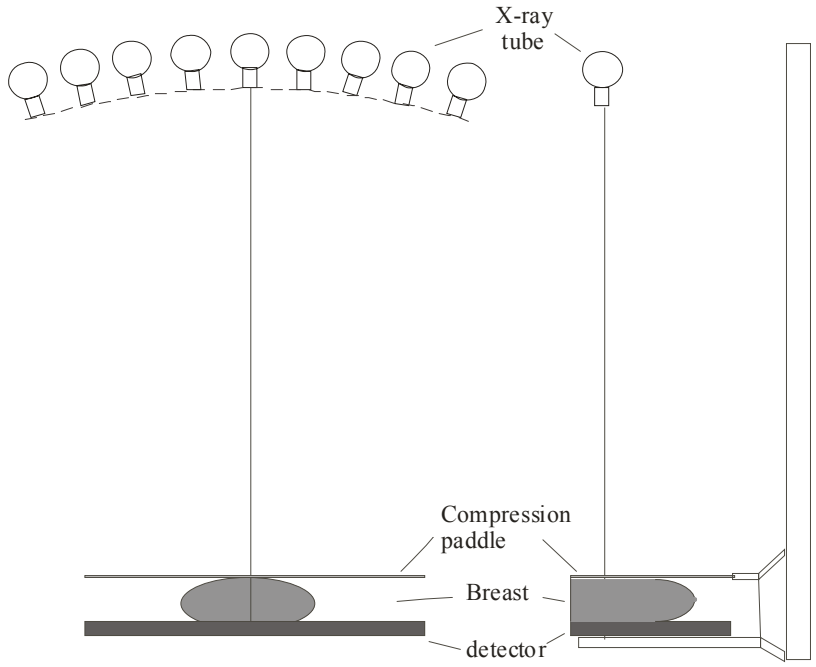

Figure 1.3, Breast tomosynthesis imaging system: (a) front view; (b) side view.

1.6 Important considerations for breast tomosynthesis

Although on the surface breast tomosynthesis only requires minor modification of a screening mammography system by incorporating motion of the x-ray tube gantry and pulsing of the x-ray exposure, it poses tremendous challenge to the imaging performance

of the detector in both image acquisition speed and electronic noise. In addition, since only a limited number of views (typically 11 to 25) are acquired over a limited angular range (typically 30 – 50 degrees), the reconstructed images have significant artifacts. Therefore it is important to optimize the imaging geometry and reconstruction methods to minimize image artifacts. These important considerations for breast tomosynthesis are discussed in the following sections.

1.6.1 Detector design and x-ray spectrum optimization

In screening mammography, the entrance exposure to the detector surface is ~ 20 mR, while in tomosynthesis, each projection image is produced with 1/N (N being the number of views) times the regular mammography dose.

Table 1.1 Imaging conditions and their impact for detector in mammography and breast tomosynthesis

	Detector for mammography	Detector for breast tomosynthesis
Exposure to the detector surface	20 mR	20 mR x 1/N (N⩾11)
Time between views	1 min	0.5~2 s
Impact		Low exposure performance; Temporal performance

Shown in Table 1.1 is a comparison of imaging conditions for mammography and breast tomosynthesis. In mammography, the entrance exposure to the detector surface after an average 4cm breast is ~ 20 mR for one single view. In breast tomosynthesis, the total dose to the breast is usually equivalent to that of single or two views in mammography. This results in an entrance exposure per view < 2 mR. With the increase in view number, which is desirable for image reconstruction, the entrance exposure reduces to 1 mR/view. With a typical digital mammography detector, the image noise at this low dose will be

dominated by the electronic noise rather than the x-ray quantum noise, and causes significant degradation of detective quantum efficiency (DQE), which reflects the efficiency of the detector in utilizing x-rays. To better engineer the detector is one approach to suppress the electronic noise. In addition, the x-ray beam quality can be optimized to increase the contrast to noise ratio (CNR) at a specific electronic noise level. This alleviates the dominance of electronic noise. Studies show that a harder beam may be desirable. One proposed tube setting was tungsten (W) with Rhodium (Rh) filter[11].

In addition to low dose performance, digital detectors designed for tomosynthesis must have good temporal performance. For screening mammography, it takes approximately 1 minute to finish the screening procedure, including <10 s for x-ray imaging time and the rest for patient preparation and image readout. This allows the detector enough time for initialization, image readout and clearing of any residual signal. However in breast tomosynthesis, all the image views have to be acquired within ~20 s in order to minimize artifact resulting from patient motion. The time delay between two consecutive x-ray exposures is only 0.5~2 s. This presents great challenge for the detector temporal performance to minimize attributes such as lag and ghosting.

1.6.2 Geometry

Imaging geometry is the basic system design and is dependent on how the x-ray tube and the detector move. The tomosynthesis imaging geometry can be categorized into two types: complete isocentric and partial isocentric[12]. For a complete isocentric system, as shown in Figure 1.4(a), the detector pivots around the central axis synchronously with the tube. For the partial isocentric system, as shown in Figure 1.4(b), only the x-ray tube will

rotate about the axis while the detector either moves laterally along one plane or remains stationary. In breast tomosynthesis, the breast will be placed either at a short distance from the detector or directly on top of it depending on the geometry used.

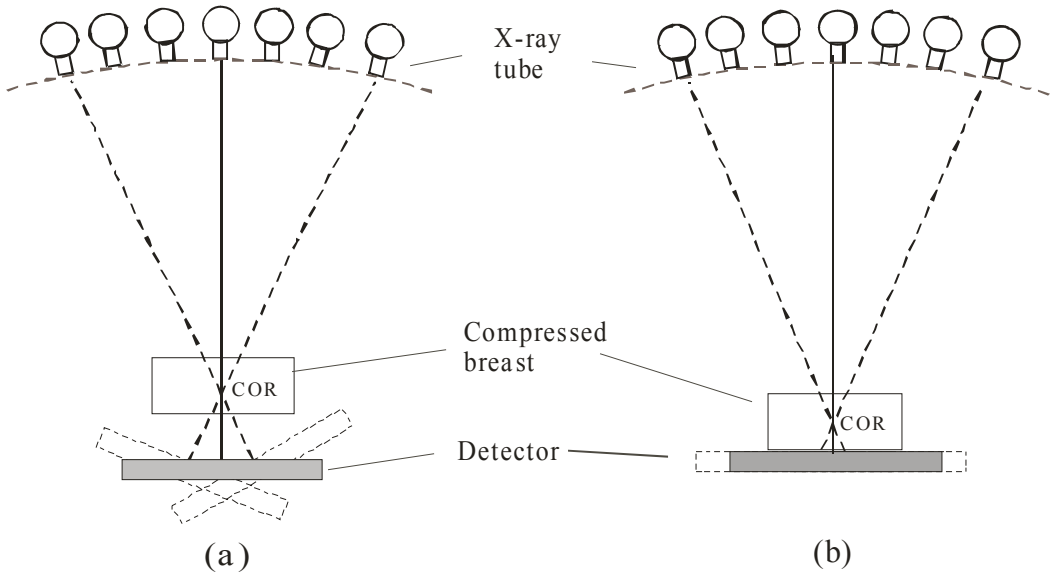

Figure 1.4, Tomosynthesis geometries: (a) Complete isocentric (b) Partial isocentric

Magnification is determined by the source to imager distance (SID), position of the center of rotation (COR) and the breast. Magnification determines the entrance exposure to the breast and the extent of focal spot blur (FSB). The angular range and the number of views are two parameters important for image acquisition. The tube can travel either in step-and-shoot or continuous modes. The step-and-shoot mode presents a challenge in the mechanical design and can easily cause system instability if scan time is short. Because patient motion is unavoidable under long scan time and causes artifacts in reconstructed images, continuous tube motion with pulsed x-ray exposures is more widely employed for practical use. The continuous tube motion, however, causes focal spot movement during x-ray exposure, therefore introducing additional FSB into the system. Previous research has demonstrated that FSB could be a serious problem unless restricted to a

sufficiently low level[10, 13]. This poses the problem of how to evaluate and reduce the effect of FSB in tomosynthesis systems.

1.6.3 Reconstruction method

There are several reconstruction methods for tomosynthesis[12]. Both analytical, such as filtered backprojection (FBP), and iterative, such as expectation maximization (EM), reconstruction methods have been applied to tomosynthesis. FBP is a standard CT reconstruction method but modified for use in limited angle reconstruction. One advantage of FBP reconstruction is that it offers an acceptable tradeoff between execution time and reconstructed image quality. Most breast tomosynthesis prototype systems developed within industry use FBP based reconstruction. Because of the limited angular range, which causes incomplete sampling of the 3-D space, the reconstructed image has limited information in the depth (z) direction. Therefore anisotropic voxel size is usually used, with higher resolution (smaller voxel dimensions) in the plane parallel to the detector surface (in-plane resolution) and lower resolution in the direction that is perpendicular to the detector plane (in-depth resolution). Artifact removal is another important aspect for tomosynthetic reconstruction. Modified filters are necessary to reduce the presence of artifacts in the depth direction[14].

1.7 Image quality assessment

The most common metric for image quality assessment is signal to noise ratio (SNR)[15]. The importance of the SNR of an object in image perception was first recognized by Rose[16] for the detection of a uniform object with mean quanta Φ_0 and

area A, and embedded in a uniform background with a mean value of Φ_b. The background has uncorrelated quanta and the noise is Poisson distributed. The contrast of the object C = $(\Phi_b-\Phi_0)/\Phi_b$ and the noise, is determined from the standard deviation $\sigma_b = \sqrt{A\Phi_b}$. The Rose SNR is given by:

$$\mathrm{SNR}_{Rose} = \frac{A(\Phi_b - \Phi_0)}{\sqrt{A\Phi_b}} = C\sqrt{A\Phi_b} \tag{1.1}$$

Rose's criterion states that the threshold of detectability of the object for a human observer is for SNR_{Rose} = 5[16].

Characteristic curves based on Fourier analysis are proposed as useful metrics to describe the imaging performance of the system[15]. The characteristic curves most commonly used to describe detector performance are the modulation transfer function (MTF), noise power spectrum (NPS) and DQE. These characteristics of the detector are determined via experimental measurement.

MTF is a measure of the spatial resolution of the imaging system in the frequency domain. Experimentally it can be measured by placing a pin hole or thin slit onto the detector, the image profiles of which are the point spread function (PSF) or line spread function (LSF). MTF is the Fourier transform of the LSF function. The sources of blur that degrade detector MTF depends on many factors. The interaction, i.e., scatter, between the x-rays and detection media is an inherent source of reduced spatial resolution. In digital systems, the pixel size partially determines the shape of the MTF, which is the product of the inherent MTF and transmission function of the pixel. The pixel aperture function is typically a two-dimensional (2-D) sinc function corresponding to the pixel size. For indirect digital detector, the inherent MTF is a significant contributor to the

system MTF degradation due to the lateral spreading of the light within the phosphor. For the direct digital detector, the inherent MTF is usually very high and therefore pixel size limits the spatial resolution.

NPS is the addition of independent noise sources, the two most important of which are x-ray quantum noise and electronic noise. Ideally quantum noise, described as Poisson white noise, should be the dominant noise source. However, quantum noise may be contaminated by other noise sources such as electronic noise. This makes NPS exposure dependent. At low exposure, NPS may become dominated by fixed pattern noise, i.e., electronic noise in the digital detector. This will subsequently cause degradation in DQE as will be discussed in Chapter 2. Experimentally NPS is measured by acquiring several flat-field images, and the 2-D NPS was calculated as the ensemble average of the Fourier Transform ($|FT|^2$) of each mean subtracted image.

Another useful quantity for detector is DQE. DQE describes the efficiency of the detector in utilizing x-rays and transferring information, i.e., SNR through the system. Mathematically DQE is given by:

$$DQE(f) = \frac{\mathrm{SNR}_{\mathrm{out}}^{\ 2}(f)}{\mathrm{SNR}_{\mathrm{in}}^{\ 2}(f)} \tag{1.2}$$

where for an x-ray imaging system, the $\mathrm{SNR}_{\mathrm{out}}$ is the output SNR, mainly determined by the gain, MTF and NPS. $\mathrm{SNR}_{\mathrm{in}}$ is the input SNR and equivalent to the incident x-ray quanta. More specifically, DQE is calculated from measured MTF and NPS according to the following equation:[15]

$$DQE(f) = \frac{k^2 MTF^2(f)}{NPS(f) q_0} \tag{1.3}$$

where q_0 is the incident x-ray quanta per unit area (in quanta mm^{-2}), and k is the measured sensitivity at a given exposure. DQE is a function of spatial frequency and within a range of 0-1, with higher value indicating better performance. Comparisons based on DQE can indicate which detector makes more efficient use of the incident photons, but such comparison does not necessarily indicate which detector will produce a better image. For DQE to be a valid metric for comparing images produced by different detectors, $SNR_{in}(f)$ for the different systems must be equal. If different kVp settings are used or if the scatter conditions are different, comparisons based on DQE may be misleading[17]. Alternatively the evaluation of image quality may use the noise equivalent quanta (NEQ):

$$NEQ(f) = q_0 DQE(f) \tag{1.4}$$

NEQ is an absolute measure of output image quality. In principle, NEQ can be used to compare an ultrasound system with a positron emission tomographic system[18].

1.8 Chapter outline

In Chapter 1, we introduced the modalities for breast imaging and the technology for x-ray detectors used in digital mammography. We reviewed two 3-D breast imaging methods: breast CT and breast tomosynthesis. Factors that affect the image quality for breast tomosynthesis were discussed.

In Chapter 2, we investigated the imaging performance of the a-Se mammography detector in order to understand the limiting factor for breast tomosynthesis. The detector was characterized by MTF, NPS and DQE at exposures down to the level experienced in

tomosynthesis. The results were compared with that predicted by the model and possible improvements were suggested for breast tomosynthesis.

In Chapter 3, we studied the temporal performance of the a-Se detector, which is one of the important factors that affect tomosynthesis. In order to understand the inherent physics, the study was performed on two electroded a-Se samples. The overall performance was measured on a FFDM detector. Optimization for breast tomosynthesis was proposed.

In Chapter 4, we experimentally characterized the detector performance of a prototype breast tomosynthesis system. The detector performance was evaluated in the context of tomosynthesis acquisition. Physical properties of the detector were characterized using the same parameters in Chapter 2 at different detector and system operational conditions. The temporal performance was measured as a function of exposure in tomosynthesis acquisition modes.

In Chapter 5, we developed a 3-D cascaded linear system model for breast tomosynthesis with FBP reconstruction to investigate the influence of detector performance, imaging geometry and image reconstruction algorithm on the reconstructed image quality. The reconstructed imaging quality was characterized by spatial frequency dependent presampling MTF, NPS and DQE in 3-D. The effect of FSB was discussed.

In Chapter 6, we validated the model by measuring noise and resolution characteristics experimentally on a prototype breast tomosynthesis system. The imaging performance was characterized by 3-D NPS and in-plane MTF and investigated as a function of reconstruction filters and acquisition configurations. An ACR phantom was

imaged to investigate the effects of angular range and detector operational modes on reconstructed image quality.

In Chapter 7, we studied the resolution in the thickness direction theoretically from the linear model. Experimental validation was performed by CT simulation and measurement on the prototype breast tomosynthesis system. Dependence of the resolution on the angular range and view number was investigated.

In Chapter 8, we give an overview regarding future work.

Chapter 2

Impact of Low Dose on Detector Performance

2.1 Introduction

The a-Se detector is susceptible to low dose in breast tomosynthesis. The entrance dose to the detector is as low as 1 mR. Because the detectors used in breast tomosynthesis are modified from mammography detectors, it is helpful to evaluate and understand the imaging performance of an a-Se FFDM detector at dose level as experienced in breast tomosynthesis so that areas of improvement can be identified.

In this chapter we characterized the detector performance by measurement of the MTF, NPS and DQE at various exposures and compared the measured results with that of the cascaded linear system model developed previously[19]. The cascaded linear model was developed for the a-Se detector and validated with experiment[20-23]. The model starts from statistically Poisson distributed x-ray quantum input. Charge generated in the photoconductor layer is calculated from the x-ray photon input multiplied with the charge conversion gain for a-Se. The output signal is then integrated by the pixel electrodes. All calculations are performed in the frequency domain. NPS and MTF at each stage are predicted. DQE is calculated from NPS and MTF. The model is a useful tool to predict detector performance for the provided x-ray spectrum, dose and detector design parameters.

2.2 Experimental setup

The full-field prototype detector has 2816 x 2048 pixels with 85 μm pixel size, which results in an active detector area of 23.9cm x 17.4cm and a Nyquist frequency f_{NY} = 5.88 cycles/mm. A 200 μm thick a-Se layer is deposited onto the TFT array. A high voltage of up to 2000 V was applied to the top electrode of the a-Se layer to establish an electric field E_{Se} during x-ray exposure. The detector is enclosed in a housing with ~ 1 mm thick carbon fiber cover. The x-rays are generated with a Lorad MIII mammography unit, which has a Molybdenum (Mo) target. The x-ray tube voltage was set at 28 kVp during the experiments with Mo filtration selected. A 3.9cm Lucite block was placed at the x-ray tube output to mimic the x-ray attenuation of a breast. The distance between the focal spot and the detector surface was 59.5cm.

Both small (0.1 mm) and large (0.3 mm) focal spots were used to generate x-rays. The large focal spot was used to generate an exposure range of 3.28 to 39.36 mR, and the small focal spot for an exposure range of 0.82 to 15.58 mR. Because of the smaller signal expected for the lower exposures generated with the small focal spot, a higher E_{Se} (10 V/μm) was used compared to that with the large focal spot (E_{Se} =7.5 V/μm). The gain of the charge amplifier was also set at a higher value for the small focal spot which resulted in a reduction in preamplifier noise.

2.3 X-ray exposure and sensitivity

The x-ray exposure for each mAs setting used in the experiment was measured with a Keithley dosimeter (model 35050 A). The mammography specific ion chamber (Keithley 96035 B) was placed at 11 cm above the detector surface, and located at the center of the detector near the chest wall side. The exposure measurement was then converted to the

detector entrance plane using the inverse square law. The pixel x-ray response of the detector at each exposure was calculated by averaging the image value in the ROI (region of interest) with 512 x 256 pixels, centered around the position of the ion chamber.

Figure 2.1 shows the measurements of pixel Analog-to-Digital Unit(ADU) values as a function of x-ray exposure generated with both the large and small focal spots. The best linear fitting to the measured data is also shown in the graphs. The pixel x-ray sensitivity k was determined from the linear fitting as 55 ADU/mR and 104 ADU/mR, respectively, for the large and small focal spots. Due to the higher amplifier gain and the higher E_{Se}, the value of k for the small focal spot is almost twice that for the large focal spot.

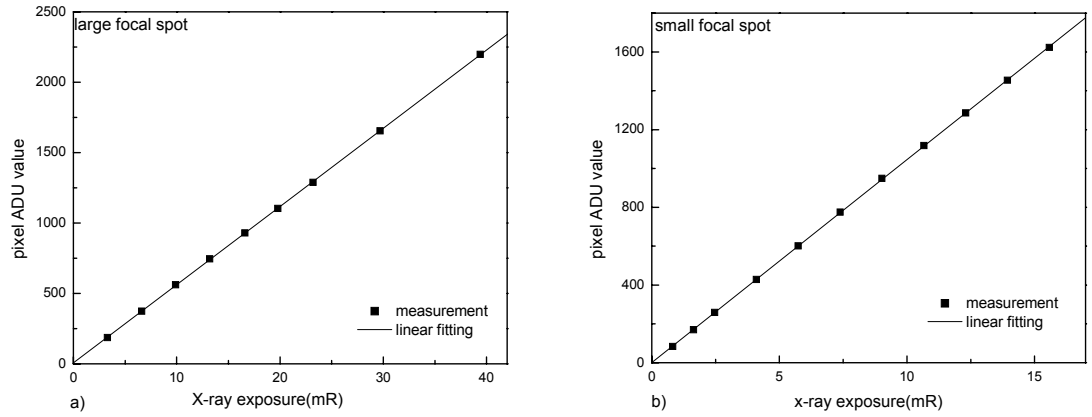

Figure 2.1. Sensitivity of the detector measured with exposures generated using: (a) large focal spot and (b) small focal spot.

2.4 Resolution and fill factor

2.4.1 MTF

The presampling MTF was measured with the slanted slit technique described by Fujita *et al*[24]. A 10 μm wide slit (Nuclear Associate) made with 1.5 mm thick W was placed on the detector surface, with the slit oriented at a small angle (less than 3 degrees) from the gate lines or the data lines. The detector surface area surrounding the slit was

covered by a steel plate in order to avoid direct radiation exposure of the detector and minimize the effect of scatter on the slit image. X-ray images of the slit were taken at 28 kVp and a high exposure of 55.76 mR so that the signal from the slit can overcome electronic noise. The slit images were corrected for offset and gain non-uniformity, as well as non-responsive pixels. The maximum pixel value of each image line (perpendicular to the slit) was determined so that the pixels that crossed the slit could be located. The location of these pixels was then fitted with a straight line in order to determine the position of the slit on the image. Depending on the point of intersection between the slit and the pixels, the image data for each line of the slit image were placed into four different bins. The image data from the four bins were then interleaved to produce a four times oversampled LSF. Then the data for the baseline of the LSF, i.e. data less than 1% of the maximum value of LSF, were fitted with a single exponential decay function in order to reduce the noise for subsequent Fourier transform of the LSF, which produces the MTF. The MTF data was then corrected for the width of the slit by dividing by the aperture function of the 10 μm slit.

The measured presampling MTF in both the gateline (perpendicular to chest wall) and dataline (parallel to the chest wall) directions are shown in Figure 2.2. Also plotted in Figure 2.2 is the modeled presampling MTF obtained using a cascaded linear system model developed previously. The aperture function in the dataline direction is slightly lower than that in the gateline direction due to a non-square pixel, which resulted in a lower MTF in the dataline direction for both the measured and modeled MTF. The deviation of the modeled MTF from the aperture function is due to two factors: (1) K-fluorescence reabsorption; and (2) blur due to charge trapping in a 2 μm blocking layer at

the interface between a-Se and the pixel electrodes. Although reasonable agreement between modeled and measured MTF was achieved, the measured MTF in both directions are slightly below that of the modeled curves, which are probably due to other factors such as scattered radiation that have not yet been included in the model.

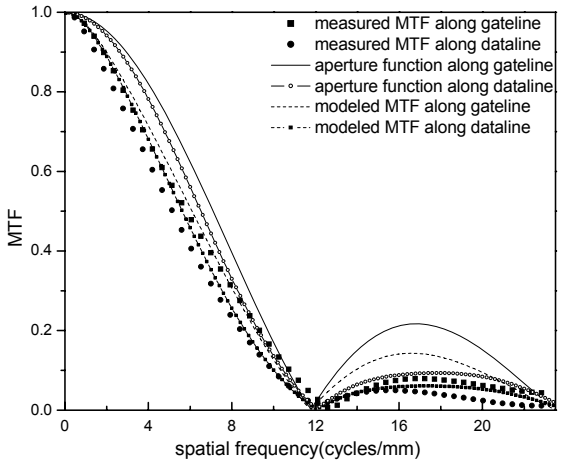

Figure 2.2, Modeled and measured presampling MTF in both the gateline and dataline directions.

2.4.2 Effective fill factor

Fill factor describes the fraction of pixel area sensitive to the incoming x-rays, ideally equivalent to one. However reduced fill factor arises due to incomplete charge collection in the gaps between neighboring pixel electrodes. A-Se direct digital detectors maintain a high geometrical fill factor by a mushroom electrode structure. Additionally, manipulated electric field above the gaps can drive charges to the electrode, resulting in an increased effective fill factor. We used the technique described by Street *et. a*l[25] to estimate the effective fill factor by measuring signal loss in the gap between pixels. The slanted slit images obtained in MTF measurement were used. Signals from all the pixels on the same image line in the direction perpendicular to the slit direction were summed and the results

were plotted as a function of the position of the slit. If image charge is lost in the gap, a drop of the signal is expected.

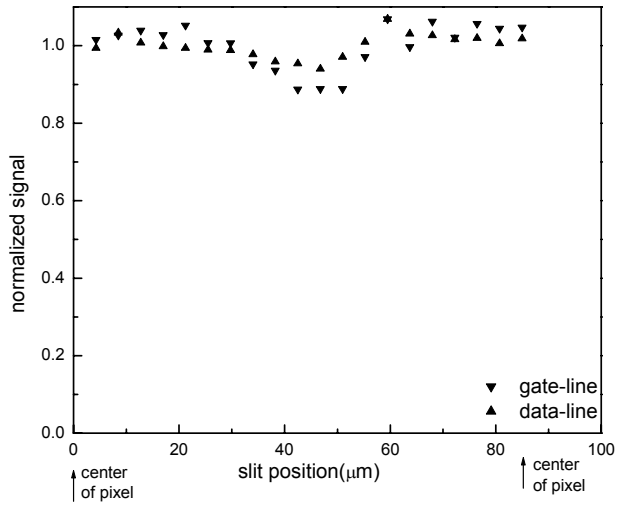

Figure 2.3, Normalized integrated signal as a function of slit position in both the gateline and dataline directions.

Plotted in Figure 2.3 is the normalized signal integral of each image line as a function of slit position. The integrated signal was normalized by the mean of the signals when the slit is near the center of the pixel electrodes. The results in Figure 2.3 exhibit a drop of signal in the gap between two pixels, which suggests incomplete charge collection. This is different from what was observed before in a small area prototype detector, where complete charge collection was achieved. This is to be expected because no preconditioning process was applied to the full-field detector where trapped charge could be built up between pixel electrodes to steer the charge in the gap toward the pixel electrodes.[26] However since the minimum signal in the gap is 90% and 95% in gateline and dataline directions, respectively, the charge loss in the gap is not significant. Due to the finite width of the slit, it is difficult to obtain an accurate estimate of the effective fill-factor f_e, hence we assumed f_e =1 in our linear system model. This should be a reasonable

assumption because the first zero of the modeled MTF (as shown in Figure 2.2) matches closely with that of the measured data.

2.5 NPS

NPS was measured for x-ray exposures ranging from 0.82 to 39.36 mR. A set of eight x-ray images was obtained for each exposure. The same 512 x 256 pixel ROI as that used in the sensitivity measurement was chosen for the NPS calculation. The ROI was free from line defects or clusters of pixel defects. Because of the small area of the ROI, the effect of radiation non-uniformity (heel effect) was negligible. It has been shown by different investigators that gain correction could have a degradation effect on DQE measurement due to the noise in the gain table[27-29]. In order to explore the inherent DQE of the detector and separate the effect of gain correction; we used two methods to calculate the NPS and compared the results. One method is to use the corrected images (with offset and gain correction), and the other is to use the subtraction of two raw images (without offset or gain correction) and divide the resulting NPS by two. We refer to these two methods as corrected and difference image methods, respectively. With the difference image method, we subtracted two subsequent raw images and obtained a total of four noise images. With the corrected image methods, all eight corrected images were used. Each noise image was divided into 128 x128 pixel sub-images, which resulted in 32 and 64 sub-images for the difference and corrected image methods, respectively. The 2-D NPS was calculated using the technique described by Dobbins. *et al*. using the formula:[30]

$$NPS(u,v) = \frac{d_x d_y}{N_x N_y} < |FT(u,v)|^2 > \quad (2.1)$$

where$< |FT(u,v)|^2 >$ represents the ensemble average of the square of the magnitude of the Fourier transform of each sub-image, N_x and N_y are the number of elements in the x and y directions, respectively, and d_x and d_y are the pixel pitch in the x and y directions (85 μm in our case). Then the one-dimensional (1-D) NPS representing the central slice of the 2-D NPS was derived from the 2-D NPS. In order to avoid the noise spikes on the central slices (usually due to fixed pattern noise of the system), thick slices consisting of eight lines on either side of the central axes were used to calculate the 1-D NPS. For each NPS value at frequency *(u,v)* in a thick slice, the frequency value was computed as $\sqrt{u^2 + v^2}$ and the results were then interleaved to obtain the final 1-D NPS.

The results of NPS measurement at exposures generated using the large and small focal spots are shown in Figure 2.4 (a) and (b), respectively. For clarity of graphing, we will only show results obtained in the gateline direction. Shown in Figure 2.4 (a) are the NPS measured at exposures of 3.28, 9.84 and 39.36mR using both the corrected and difference image methods. It shows that the NPS calculated using the corrected image method is higher than that obtained using the difference image method, which means that the noise introduced by the gain correction is higher than the noise due to the gain difference between the pixels in the ROI. For the present work, we will use the NPS calculated using the difference image method to derive the DQE since it is closer to the intrinsic DQE of the detector.

Figure 2.4(b) shows the NPS measurement obtained using the difference image method at 0.82, 10.66 and 15.58 mR using the small focal spot. Plotted in the same graph

is the NPS of the electronic noise. At the lowest x-ray exposure (0.82 mR), the contribution of the electronic noise to the total NPS is more than 50%, and the system falls short of quantum noise limitation. At higher exposure (10.66 mR) where the x-ray quantum noise is clearly dominating, the NPS shows a drop at high spatial frequency, which shows the intrinsic NPS characteristics of the detector. The NPS at f_{NY} is ~ 70 % of the NPS (0).

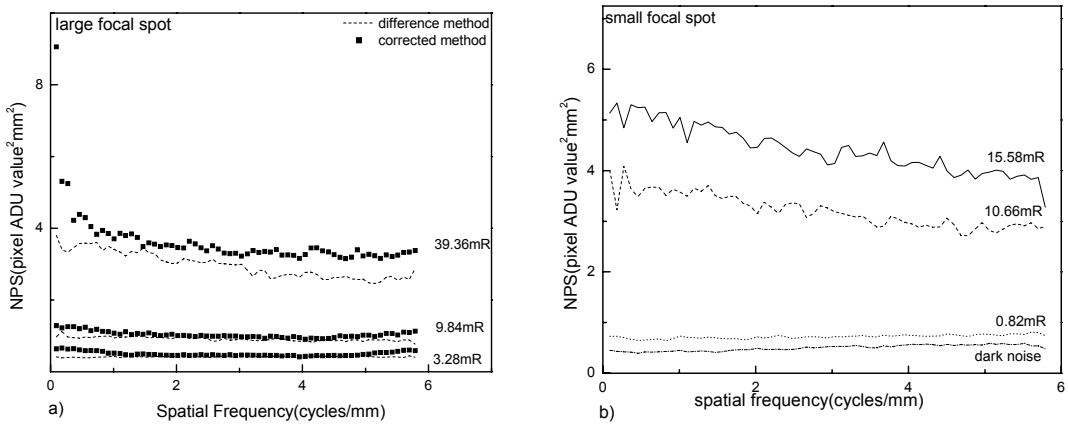

Figure 2.4. NPS measured at different exposures for: (a) the large and (b) the small focal spots

Shown in Figure 2.5(a) is the NPS calculated using the linear systems model, which also indicates a drop at high spatial frequencies. This drop is due to two factors: (1) K-fluorescence reabsorption; and (2) blur due to charge trapping in a 2 μm blocking layer at the interface between a-Se and the pixel electrodes. Shown in Figure 2.5(b) is the comparison between the measured and the modeled NPS of the prototype detector, where the model NPS in Figure 2.5 (a) has been rescaled to the measured NPS at 39.36mR. It shows good agreement between the shape of the measured and the modeled NPS.

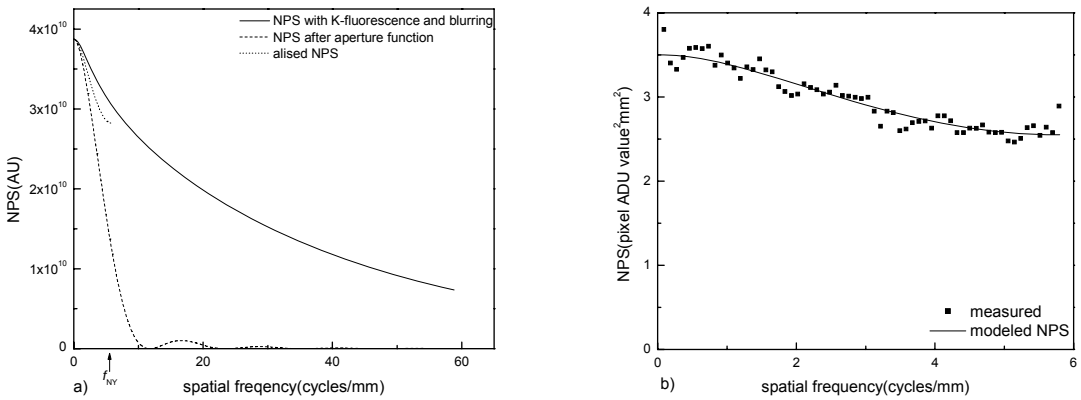

Figure 2.5 (a) Modeled NPS of the prototype detector, where the aliased NPS is plotted up to f_{NY} =5.88 cycles/mm; (b) comparison between measured and modeled NPS at 39.36mR.

In order to determine the importance of electronic noise relative to the x-ray intensity, we plotted the NPS (0) as a function of radiation exposure used in our measurement. The results are shown in Figure 2.6(a) and (b) for the large and small focal spots, respectively. Both sets of measurement demonstrate a linear increase in NPS (0) as a function of exposure, which is to be expected from the Poisson statistics of x-ray quantum noise. The intersection between the linear fitting of the measured data and the y-axis is the estimate of the magnitude of the electronic noise power. Figure 2.6(a) shows that with the experimental setting for the large focal spot, the dark noise is equivalent to the x-ray noise at 3.2 mR of exposure. Whereas with the small focal spot (Figure 2.6b), the dark noise is less important where it is equivalent to the x-ray quantum noise at 2.0 mR of exposure. This is because of the higher E_{Se} which resulted in higher x-ray to charge conversion gain, and a higher preamplifier gain setting which resulted in lower electronic noise. The comparison between Figure 2.6(a) and (b) demonstrated that increasing E_{Se} and reducing the electronic noise can be effective methods to reduce the detector's susceptibility to electronic noise so that high image quality can be obtained at low dose. This is important for advanced applications of digital mammography detectors such as

tomosynthesis, where the exposure used to generate one image is reduced by an order of magnitude.

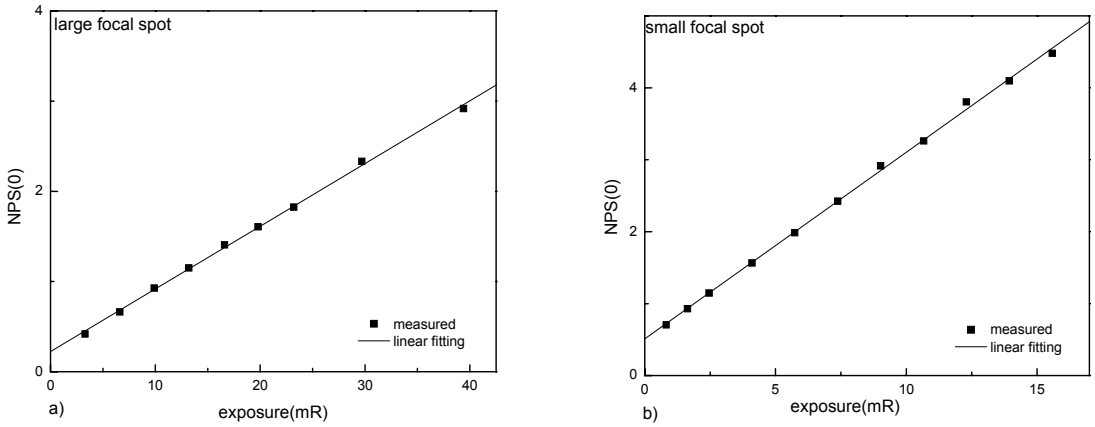

Figure 2.6, NPS(0) as a function of exposure generated using: (a) large focal spot; and (b) small focal spot.

2.6 DQE

From the measured presampling MTF and NPS, DQE was calculated using Eq 1.3[15]. The value for x-ray quanta q_0 was calculated from the modeled spectrum obtained using Boone's method[31-33]. In previous work, we have used direct integration of the x-ray spectrum to obtain q_0:[34, 35]

$$q_0 = \int_0^{kVp} \varphi(E)d(E) \tag{2.2}$$

which is consistent with the assumption of an ideal photon counting detector. For energy-dependent x-ray imaging detectors, it may be more appropriate to assume a perfect energy integration detector, in which case an energy weighted q_0 should be used:[31-33]

$$q_0 = \frac{[\int_0^{kVp} \varphi(E)EdE]^2}{\int_0^{kVp} \varphi(E)E^2dE} \tag{2.3}$$

It has been shown previously that the difference in the two quantities defined in Eq. (2.2) and (2.3) is only about 4 % for x-ray spectra typically used in mammography[36].

In order to be consistent with our previous work, the DQE will be calculated using q_0 obtained from Eq. (2.2), but we have also calculated q_0 using Eq. (2.3), and determined the effect of q_0 on DQE calculation. The detector incident x-ray fluence Φ_0 was determined to be 4.82x10^4 photons/mm^2/mR using Eq. (2.2) and 4.71 x10^4 using Eq. (2.3). The difference is ~ 2 % and insignificant.

Plotted in Figure 2.7 are the DQE values calculated using Eq. (1.3) for four different exposures: 0.82, 3.28, 15.58 and 39.36 mR. As exposure decreases to 0.82mR where electronic noise is dominant, DQE (0) drops to 40% of the value at highest exposures. This is consistent with the dark noise results shown in Figure 2.6.

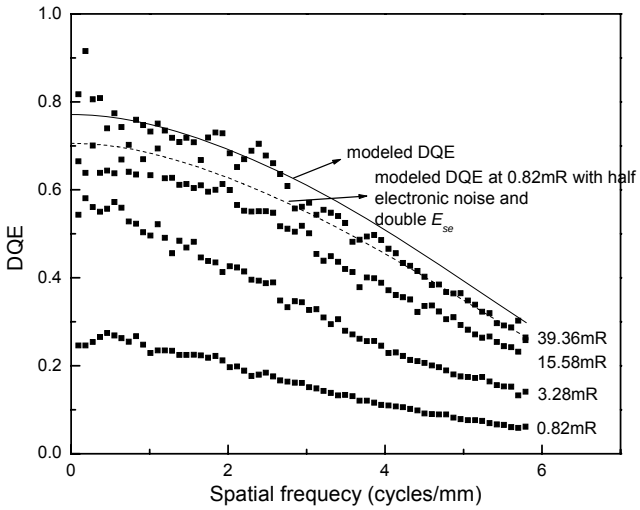

Figure 2.7 Experimental results for DQE at different exposures, solid line indicates modeled DQE at 39.36mR, dash line indicates modeled DQE at 0.82mR with half electronic noise and double electronic field, it shows DQE at low exposure can be increased with changing detector setting

Also plotted in Figure 2.7 (with solid line) is the modeled DQE using the linear system model. It shows good agreement between measured DQE at high exposures and the modeled DQE, except that the measured DQE drops slightly faster at high spatial frequencies due to the discrepancy between the measured and modeled MTF shown in Figure 2.2. The model predicts DQE(0) = 76%, this value includes x-ray attenuation of 1 mm of carbon fiber detector window(~11%) and a 2 μm blocking layer(~5%) at the

interface between a-Se and the top bias electrode which attenuates x-rays but does not contribute to signal due to zero electric field. In order to increase the DQE at low exposure, e.g. 0.82 mR, we need to further increase the gain or decrease the noise of the system. The former can be achieved by increasing the electric field E_{Se} across the a-Se layer. The tradeoff between increasing gain and increasing E_{Se}, or high voltage applied on the a-Se layer remains to be investigated. Shown in Figure 2.7 (dotted line) is the DQE prediction for 0.82mR if the E_{Se} is doubled and the electronic noise halved from the current detector setting. It shows that DQE(0) is increased to 70% from the current 30%. These improvements in detector performance are required in order to achieve good imaging performance for the low dose used in tomosynthesis.

2. 7 Conclusions

It was found that quantum noise becomes dominant at exposures >10 mR. At the lowest x-ray exposure (0.82 mR), the contribution of the electronic noise to the total NPS is more than 50%, resulting in a drop in DQE of 40% compared with DQE at high dose. The cascaded detector model predictions showed that if the electronic noise is suppressed to half the present level, DQE (0) improved to 60%, the level at high exposure. We concluded that decreasing electronic noise and increasing the x-ray to charge conversion gain in a-Se can be effective methods to improve the detector DQE at very low exposures as experienced in tomosynthesis.

Chapter 3

Temporal Performance of a-Se Detectors in Mammography and Breast Tomosynthesis

3.1 Background

Temporal imaging characteristics of x-ray imaging detectors can be separated into two categories: lag and ghosting (Figure 3.1). Lag is the residual signal generated by previous x-ray exposure into subsequent image frames. It is manifested as changes in dark images, i.e., readout of the detector without x-ray exposure. Ghosting is the change in x-ray sensitivity, or gain, of the detector as a result of previous exposure to radiation. It can only be seen with subsequent x-ray exposures.

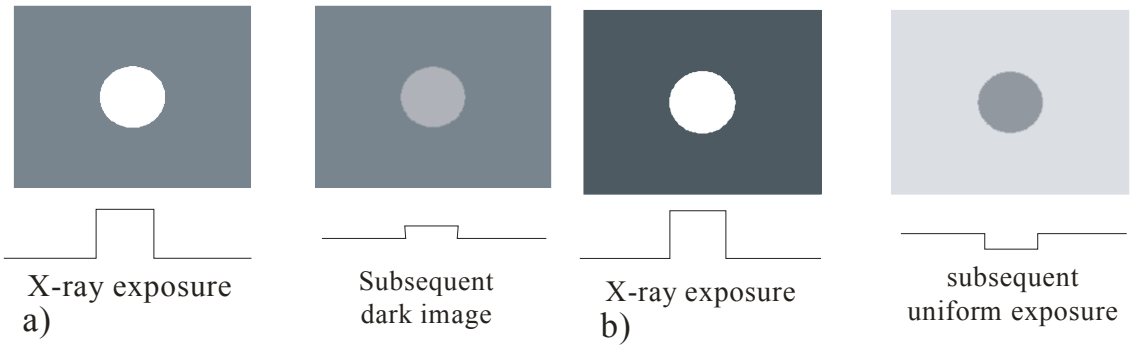

Figure 3.1, diagram for artifact caused by lag or ghosting. a) Lag is the residual signal generated by previous x-ray exposure; b) ghosting is the sensitivity change as a result of previous x-ray exposure

The temporal response caused by charge trapping and release gives rise to the imaging properties of lag and ghosting. Factors that affect the temporal performance include the design and operational parameters, e.g., E_{Se}, of the detector and the material properties of a-Se. A previous study on different mechanisms for lag and ghosting in a-Se flat-panel detectors showed that the dominant source of lag is the enhanced charge

injection from the bias electrodes as a result of previous exposure, and the dominant source of ghosting is the changed x-ray sensitivity as a result of bulk trapping[37].

In the a-Se layer there are a substantial number of deep traps for electrons and holes. These traps are energy states that may be occupied with x-ray generated charge. When x-rays are absorbed in a-Se, EHP are generated. The free charge carriers (electrons or holes) move toward the electrodes due to the applied electric field across a-Se and may fall into traps within the bulk of the material. The probability that charge may become trapped increases at lower values for applied electric field. Charge trapping occurs in three locations: 1) in the bulk of the a-Se layer; 2) at the interface between layers; 3) between pixel electrodes of the active matrix. Bulk trapping is the major source of trapping. Because the voluntary release of charge takes minutes for trapped holes and hours for trapped electrons, trapped electrons are the main source for temporal artifacts.

Trapped electrons in the bulk of the a-Se cause ghosting by the following mechanisms: (1) the distribution of trapped charge changes the electric field in the a-Se layer, which affects the x-ray-to-charge conversion gain. The electric field could either be enhanced or reduced; therefore the sensitivity change will be either positive or negative; (2) recombine with x-ray generated free holes, which reduces the x-ray sensitivity. (3) x-rays generate new trapped charge, which causes a sensitivity reduction as in (2). The combination of the three mechanisms is likely to cause a reduction in x-ray sensitivity. Trapped charge between pixel electrodes is another significant contributor to ghosting. Charge carries trapped via this mechanism cause a change in the local electric field near the electrodes, resulting in an increased effective fill factor, which increases the

sensitivity. Ghosting in a-Se flat-panel detectors is dominated by the long term effect of electrons captured in deep traps in the bulk.

Bulk trapping can contribute to lag through the following mechanisms: (1) Charge carriers trapped during one image frame can be released in subsequent image frames. (2) In a-Se layers with constant bias potential, i.e. with electrodes on both surfaces of the a-Se, charge trapped in the bulk increases the electric field at one of the electrode interfaces. This can cause increased charge injection from the bias electrodes which contributes to lag. Lag is a short-term effect and dependent on the time interval between consecutive x-ray exposures.

3.2 Introduction

In mammography, because of the wide range of exposure encountered by the detector (the raw exposure outside the breast is 1 R and the exposure behind the dense breast is several mR.), ghosting, which is manifested as the outline of a previously exposed breast, can be a potential problem. In breast tomosynthesis, several images are acquired within a regular patient scan time, i.e. <20s, and the image frame rate is much higher compared with that in mammography. Because lag presents as short-term artifact, it has more impact than ghosting for breast tomosynthesis. Preliminary studies of lag and ghosting on a-Se flat-panel digital mammography detectors have been performed in the context of both screening and advanced mammography[19, 38, 39]. Since the cumulative effect of ghosting could be important during the daily operation of the detector, it is necessary to study the temporal performance as a function of cumulative radiation exposure. Quantitative measurement of x-ray sensitivity was performed on electroded a-Se samples as a function of cumulative exposure at radiographic energies for electric field E_{Se} up to 5

V/μm.[40] It was found that ghosting was strongly dependent on cumulative exposure and E_{Se}. However no physical mechanism was provided for the field and exposure dependence, and the range of E_{Se} used in this study is not sufficient for practical use in x-ray imaging.

In this chapter, temporal imaging characteristics were studied both on a prototype full-field digital mammography detector[19] and small area electroded a-Se samples[41]. The measurement on the prototype full-field detector will show the overall temporal performance of the detector and the measurement on the samples will help understanding the inherent physics of lag and ghosting.

Because both the x-ray unit and our prototype FFDM detector could not be operated in tomosynthesis mode, the measurement on the prototype detector was performed with the detector operated in a typical screening mammography image acquisition sequence, where the time lapse between two subsequent exposures was ~60 seconds. The raw exposure delivered to the detector varied from several mR to several R.

Since lag and ghosting measurements from a flat-panel detector depends on its operational sequence, e.g. reset procedure between exposures, the results may not be suitable for understanding the physical mechanisms for lag and ghosting. In order to measure the temporal performance of the detector as a function of cumulative exposure and in the context of breast tomosynthesis, the investigation on temporal performance was performed using a-Se samples. Two small area electroded a-Se samples, one positively and the other negatively biased on the entrance side of x-rays, were used in the experiments. The study was performed by delivering a number of raw exposures as experienced in screening mammography to the samples at different E_{Se} while measuring

the current through the a-Se sample. Both lag and ghosting were measured as a function of E_{Se} and cumulative exposure. The values of E_{Se} used in our experiments ranged from 1 to 20 V/μm. Ghosting at different operational conditions was quantified as the percentage x-ray sensitivity (x-ray generated photocurrent measured from the sample) reduction compared to before irradiation. Lag was determined by measuring the residual current of a-Se at a given time (0.5s and 33ms) after the end of each x-ray exposure, which represents the application in tomosynthesis and fluoroscopy, respectively.

3.3 Temporal Performance of FFDM detector

The full field a-Se detector used for this study and the x-ray equipment are identical to the study described in Chapter 2. Although the readout time of the detector is one second, due to the limitation of the x-ray generator, we were not able to study the temporal performance of the detector at its maximum frame rate. During the measurement the prototype detector was operated in a typical screening mammography image acquisition sequence and the time lapse between two subsequent exposures was ~60 seconds[19]. Since at this rate the offset images of the detector can be updated frequently, offset subtraction can minimize the effects of lag.

3.3.1 Lag

The image acquisition sequence for the measurement of lag is shown in Figure 3.2, where offset corrected images were obtained with time interval of 42 seconds. With a single x-ray exposure ranging from 0.92 to 3.66 R (28 kVp), 20 dark images were acquired before and after the x-ray exposure. The average signal of a 200 x 200 pixel

ROI within the radiation field was calculated, so that the residual lag after offset correction can be examined as a function of time.

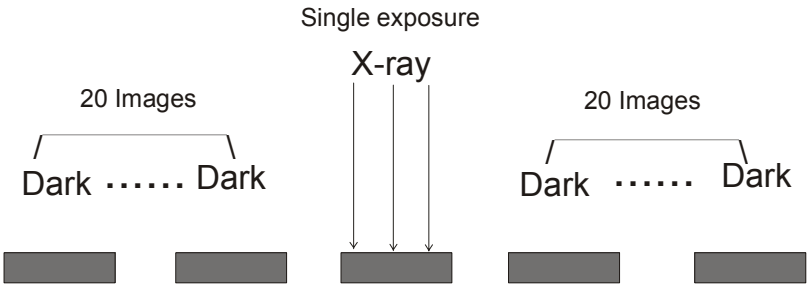

Figure 3.2, Image acquisition sequence for the study of lag.

Figure 3.3 shows the result of the lag measurement. The offset subtracted signal is plotted as a function of time for the 20 dark images acquired before and after the single x-ray exposure. The dark signal was normalized as the percentage of the signal obtained for the single x-ray frame.

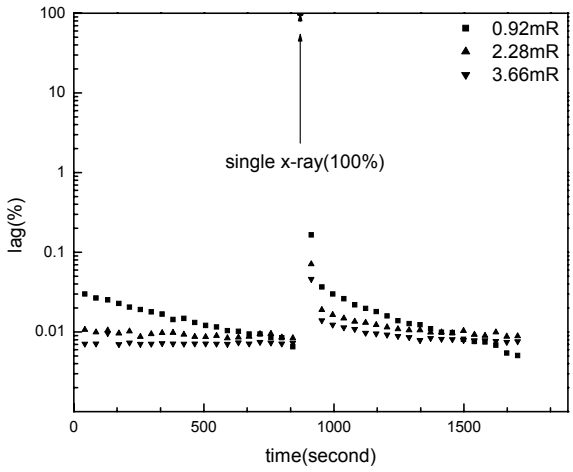

Figure 3.3, Percentage of lag as a function of time before and after a single x-ray exposure of different magnitude (0.92, 2.28 and 3.66 R).

As shown in Figure 3.3, the first frame lag for all three exposure levels used in the experiment was <0.2 %. As expected, the magnitude of lag increases with exposure level. This lag measurement at low frame rate is insignificant compared to published first frame lag measurement for real-time direct flat-panel detectors, which is ~ 5 %. It demonstrates

that frequent update of offset images can essentially eliminate lag in screening mammography applications. Although the frames rate needs to be much higher in tomosynthesis, it is still feasible to acquire one offset frame between two subsequent exposures.

3.3.2 Ghosting

The image acquisition sequence used for the measurement of ghosting is shown in Figure 3.4, where two different x-ray exposure levels were used for each sequence: one is referred to as the ghosting dose, and the other as the regular dose. The reason for using two different doses was to mimic the imaging conditions where ghosting is most likely to be generated. In mammography, the largest change in exposure to the detector occurs at the outline of the breast, where the average exposure within the breast near the skin line is ~40 mR, and the exposure outside the breast is >1 R. This large difference in exposure could result in different x-ray sensitivity in different regions of the detector, which leads to ghosting. Ghosting will most likely manifest as the outline of a previously imaged breast. In our experiment, we set the regular dose to 37 mR, which is close to the exposure level near the skin line, and the ghosting dose ranging between 1.83 and 3.20 R, which is equivalent to the raw exposure to the detector (outside the breast). The x-ray spectrum used in the measurement was 28 kVp without added Lucite in the beam. As shown in Figure 3.4, the x-ray exposure level was first set to the regular dose with 20 images acquired. Then a single x-ray exposure of the ghosting dose was given, followed by the acquisition of another 20 images with the regular dose. The same image sequence was repeated for each different ghosting dose. The time interval between two subsequent

x-ray images was 54 seconds. The x-ray sensitivity of the detector at regular dose was calculated by averaging the offset subtracted signal from all the pixels in a 200 x 200 pixel ROI within the radiation field. The x-ray sensitivity before and after the ghosting dose was monitored and compared.

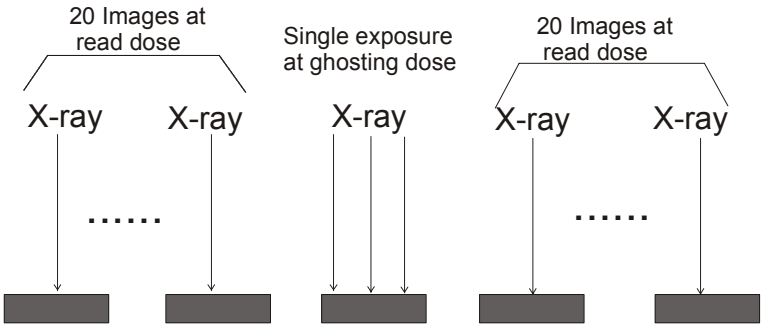

Figure 3.4. Image acquisition sequence used for the measurement of ghosting. Regular dose was set at 37 mR and ghosting dose ranged between 1.83 and 3.20 R.

Figure 3.5 shows the results of ghosting experiments for two different ghosting dose of 1.83 and 3.20 R. The offset subtracted signal at regular dose, which was used as a measure of the detector's x-ray sensitivity, was plotted as a function of time. The frame within which the ghosting dose was delivered was marked with an arrow. From the plot there is no obvious change in x-ray sensitivity after the ghosting dose, hence we took the average of the x-ray sensitivity for the 20 frames before and 20 frames after the ghosting dose. For the ghosting dose of 1.83 and 3.20 R, the average sensitivity dropped by 0.3% and 0.5%, respectively. This indicates that the amount of bulk trapping and recombination in a-Se after the dose of a single screening mammogram is negligible. Since charge trapped in the bulk of a-Se is located in deep traps, they will not be released for hours or even days after being trapped. Hence it is reasonable to extrapolate the ghosting measurement performed at screening mammography time intervals to fast frame rate required for tomosynthesis. Ghosting is not expected to be significant for tomosynthesis.

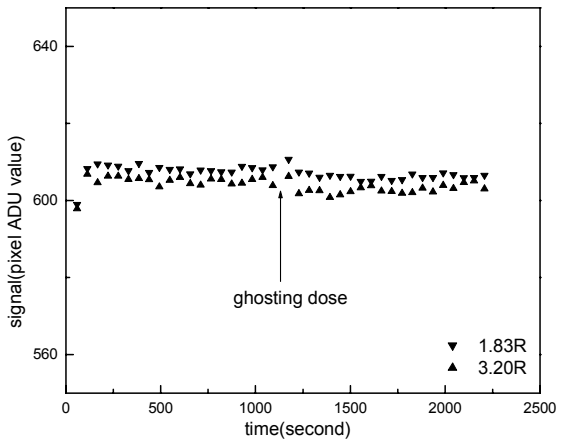

Figure 3. 5, X-ray sensitivity before and after the ghosting dose of 1.83 and 3.20R.

3.3.3 Conclusions

We studied the temporal imaging performance of a FFDM detector including both lag and ghosting for low frame rates encountered in screening mammography. Our results showed that lag can be practically eliminated by update of the offset image (dark image before x-ray exposure) between exposures. However the feasibility and effectiveness of this method at the fast frame rate anticipated for tomosynthesis needs further investigation. The results of our ghosting measurement showed that ghosting after the dose of a single screening mammogram is negligible. Since ghosting measurement does not depend strongly on frame rate, we expect ghosting to be negligible for tomosynthesis also.

3.4 Study of Temporal Performance in tomosynthesis mode on a-Se samples

In this study we performed quantitative measurements of lag and ghosting of a-Se mammography detectors as a function of cumulative exposure at E_{Se} up to 20 V/μm. In

order to focus our study on the effect of a-Se only, electroded a-Se samples as opposed to flat-panel detectors were used. These samples were identical to the a-Se used in digital mammography flat-panel detectors[38, 42]. Two types of a-Se samples were used, one positively and the other negatively biased on the entrance side of x-rays, both of which have been used in a-Se flat-panel detectors. We will present the investigation of the temporal performance of these two samples as a function of cumulative exposure and E_{Se} and then discuss the physical mechanisms.

3.4.1 Experimental Apparatus

The a-Se samples were deposited using an identical procedure as that used in a-Se FFDM detectors. The negatively biased sample has a layer thickness (d_{Se}) of 240 μm and an active area (defined by the bias electrodes) of 87 x 87 mm^2. The positively biased sample is 200 μm thick and 46 x 46 mm^2 in active area. Each sample has blocking layers for both bias electrodes to minimize charge injection, which is the dominant source of dark current[42]. The measured dark current at the same E_{Se} for the negatively biased sample is approximately two orders of magnitude higher than that for the positively biased sample. At 10 V/μm, the dark current is ~ 1.7 x 10^{-10} A/cm^2 and ~1.6 x 10^{-12} A/cm^2 for the negatively and the positively biased sample, respectively. Shown in Figure 3.6 is the apparatus used in our experiments. A high potential was applied to the top electrode (x-ray entrance side) of the a-Se layer so that an E_{Se} could be established during x-ray exposures. The bottom electrode was connected to the input of a low noise current amplifier (SR570, Stanford Research System), which has programmable bandwidth and gain. The output voltage of the amplifier was digitized by a 16-bit analog-to-digital

converter (PCI-6052E, National Instrument). A Bennett Contour mammography system (Bennett X-ray Technologies, Copiague, NY) was used for x-ray production. The x-ray tube has a Mo target and added filter of either Mo or Rh. The thickness values for the Mo and Rh filters are 20 and 15 μm, respectively. These values are smaller than those commonly used with Mo target, this is because the collimator mirror in our x-ray unit does not retract during x-ray exposure and results in an additional attenuation. During all the experiments, the tube potential was set at 28 kVp with Mo filtration, which produced a spectrum with a HVL (half value layer) of 0.319 mm (Al) and a mean energy of 17 keV. The x-ray spectrum used in our experiments was calculated using the parameterized model Molybdenum Anode Spectral Model using Interpolating Polynomials (MASMIP)[34]. The mean energy was calculated using:

$$\overline{E} = \frac{\int_0^{\max} E\Phi(E)dE}{\int_0^{\max} \Phi(E)dE} \tag{3.1}$$

where $\Phi(E)$ is the calculated x-ray spectrum. We used the unattenuated x-ray spectrum in our investigation of lag and ghosting. This is because the regions of the detector that will generate the most lag and ghosting is where "raw" radiation is received, i.e. without attenuation of the breast. The a-Se sample was centered along the chest-wall side. The x-ray exposure was measured with an ion chamber (Model 35050A, Innovision) placed at 15 cm above the detector plane to minimize the effect of back scatter from the detector. The detector entrance exposure was then calculated using the inverse square law.

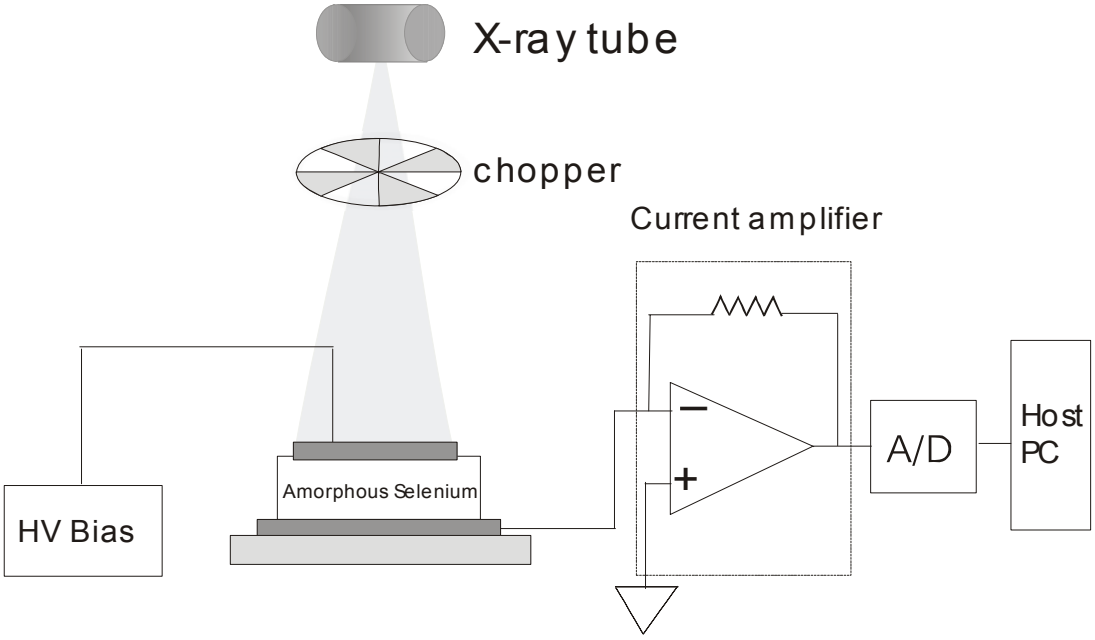

Figure 3.6, Schematic diagram of the experimental setup for lag and ghosting measurements. A high potential (HV bias) was applied to the top electrode (x-ray entrance side) of the a-Se layer. The bottom electrode was connected to the input of a low noise current amplifier. The output voltage of the amplifier was digitized by a 16-bit analog-to-digital converter (A/D) and the data was stored in a host PC and analyzed with Matlab.

3.4.2 Ghosting Measurements

The sample was rested in dark for 24 hours before each ghosting experiment. After the application of high voltage, the dark current was allowed 20 minutes to stabilize before the first x-ray exposure[43]. Due to the limitation of our x-ray generator, the minimum time interval between subsequent exposures was ~70 seconds, which is an acceptable value for screening mammography. Because ghosting is a long-term effect, which will last for hours, it will show similar dependence on cumulative exposure in screening mammography and in tomosynthesis with a high frame rate. Each sample was exposed to 60 x-ray exposures, each of which was ~ 1 R (8.76 mGy). The applied electric field E_{Se} ranged from 1 to 20 V/μm, which includes the E_{Se} of 10 V/μm most commonly

used in commercial flat-panel detectors. The current through each sample was measured before, during and after each x-ray exposure.

In order to determine the x-ray sensitivity of a-Se, dark current (which is primarily due to charge injection from the bias electrodes) needs to be determined and subtracted from the photocurrent measurements. It has been found previously that charge injection increases during x-ray exposure due to a weakened blocking layer as a result of x-ray generated charge in the bulk of a-Se[44]. In order to determine the enhanced charge injection, it is important to interrupt the x-ray exposure for a short period of time and perform the dark current measurements. Two methods have been used in the past: (1) to deliver the exposure in a series of short pulses and measure the dark current between x-ray pulses[40, 45]; and (2) to use a rotating chopper to modulate the x-ray beam and measure the dark current when the x-rays are blocked by the chopper[37, 46]. Due to the limitation of our x-ray generator, we chose the second approach. The rotating chopper (made with 2.5 mm thick brass) was operated at a frequency of 30 Hz. An example of the output waveform is shown in Figure 3.7. With a total exposure time of 1.25 second, we had more than 30 measurements of the x-ray photocurrent I and the enhanced dark current B_X, which were measured as the maximum and the minimum current of each cycle, respectively. As shown in Figure 3.7, the difference between the averaged I and B_X was used as the measurement of x-ray sensitivity S. The first and last four data points were excluded from the average because the exposure rate may fluctuate at the beginning and end of the x-ray exposure.

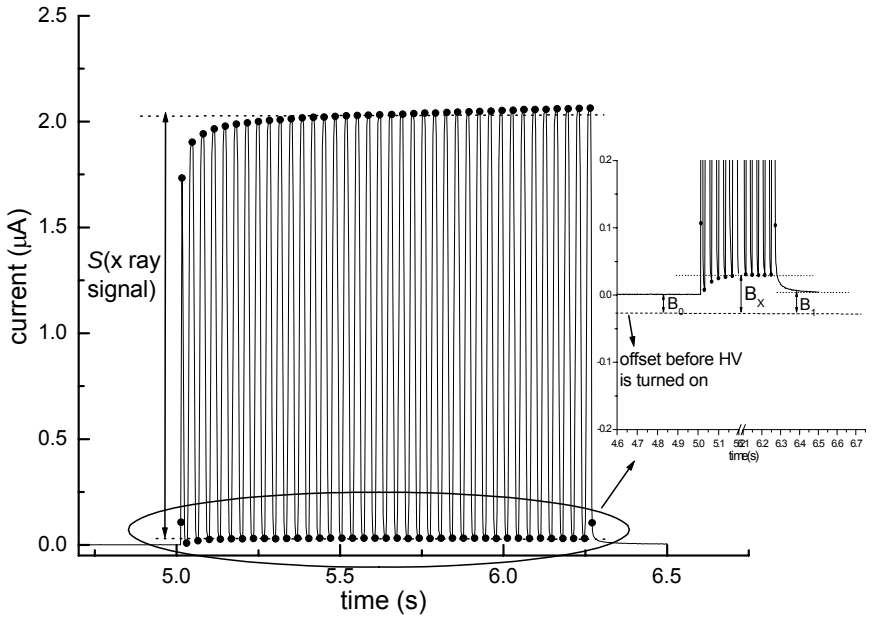

Figure 3.7, A typical x-ray photocurrent measurement with an x-ray pulse of 1.25 seconds. The chopper frequency was set at 30 Hz. The insert is the magnified view of the circled region showing the measurement of dark current. The symbols used in the graph and text are: *S*: x-ray signal; B_0: dark current measured before x-ray exposure; B_1: dark current measured at 0.5 s after x ray exposure; B_X: mean dark current (charge injection) measured during x-ray exposure through the use of a chopper.

Ghosting was quantified as the percentage change in x-ray sensitivity from the initial value:

$$g_n = \frac{S_n}{S_1} \tag{3.2}$$

where S_1 and S_n are the x-ray sensitivity measured at the first and *n*th x-ray exposure, respectively. Larger ghosting indicates a decrease in the x-ray sensitivity.

Although the dominant mechanism for ghosting is trapped electrons, holes can also get trapped in a-Se and play a role in the ghosting measurements depending on the energy depth of traps and time interval between subsequent exposures. The time constant τ for a charge carrier to be released from a trap is given by:[47]

$$\tau = \nu^{-1} e^{E_T / kT} \tag{3.3}$$

where ν is the phonon frequency, E_T is the energy depth of the trap, k is the Boltzman's constant and T is the absolute temperature. The estimated E_T for deep hole and electron traps is ~ 0.9 and ~ 1.0 eV, respectively[48], which result in an estimated τ on the order of minutes for holes and hours for electrons.

In order to determine whether trapped holes played a role in our ghosting measurements, we repeated the ghosting measurements at two different E_{Se} (6 and 10 V/μm) with increased time interval of 5 minutes between subsequent exposures, and compared the results with those obtained with 70 seconds time interval.

3.4.3 Ghosting: Results

Shown in Figure 3.8 are the results of ghosting measurements with 70 seconds time interval. The percentage x-ray sensitivity is plotted as a function of the number of exposures at different E_{Se}. Figure 3.8 (a) shows the result for the negatively biased sample. The most dominant effect of x-ray exposure on ghosting is a decrease in x-ray sensitivity, which is consistent with previous findings with a single, large x-ray exposure[49, 50]. This has been attributed to trapped charge in the bulk of a-Se, which recombines with the x-ray generated free carriers in subsequent exposures. As shown in Figure 3.8(a), the rate of x-ray sensitivity change decreases with the number of exposures at each E_{Se}. This is because the probability of charge trapping is proportional to the concentration of the empty electron traps, which decreases as a function of exposure[50]. In addition, the trapped electrons recombine with x-ray generated free holes with a rate proportional to the concentration of trapped electrons. Consequently, a dynamic equilibrium will be established when the newly generated trapped electrons are equal to the recombined trapped electrons. As a result, the x-ray sensitivity will eventually

saturate with more x-ray exposures. Another obvious dependence of ghosting is that it decreases with increasing E_{Se}. At the lowest E_{Se} of 1 V/μm, the x-ray sensitivity drops by 78 % after 60 exposures, which is quite significant. At E_{Se} = 10 V/μm which is commonly used in clinical a-Se based flat-panel detectors, ghosting reduces less significantly, where the decrease in x-ray sensitivity is ~ 12 % after 60 exposures. This is because at higher E_{Se} the electrons are less likely to get trapped in the bulk, which result in lower trapped charge density for the same exposure. In addition, since the x-ray sensitivity of a-Se increases with E_{Se}, the percentage reduction in sensitivity due to recombination with trapped electrons is decreased. Although the dominant effect of x-ray exposure is a decrease in sensitivity, there is a noticeable increase in sensitivity for the first several exposures at $E_{Se} \geq 10$ V/μm. The highest sensitivity is 109 % and 105 % for E_{Se} = 20 and 10 V/μm, respectively. This may be attributed to other mechanisms for ghosting that have been identified previously in addition to the dominant mechanism of recombination. Two possible mechanisms are: 1) an increased E_{Se} as a result of bulk trapping; 2) enhanced charge injection which is not properly subtracted with the approach used in the present study. Since the charge injection increases as a function of E_{Se}, its effect on sensitivity will be more severe at higher E_{Se} values. The explanation for the first mechanism will be provided later in this section together with the results from other samples and time intervals. It is plausible that these two mechanisms at high E_{Se} dominated the ghosting for the first several exposures when the trapped charge density in the bulk is still low.

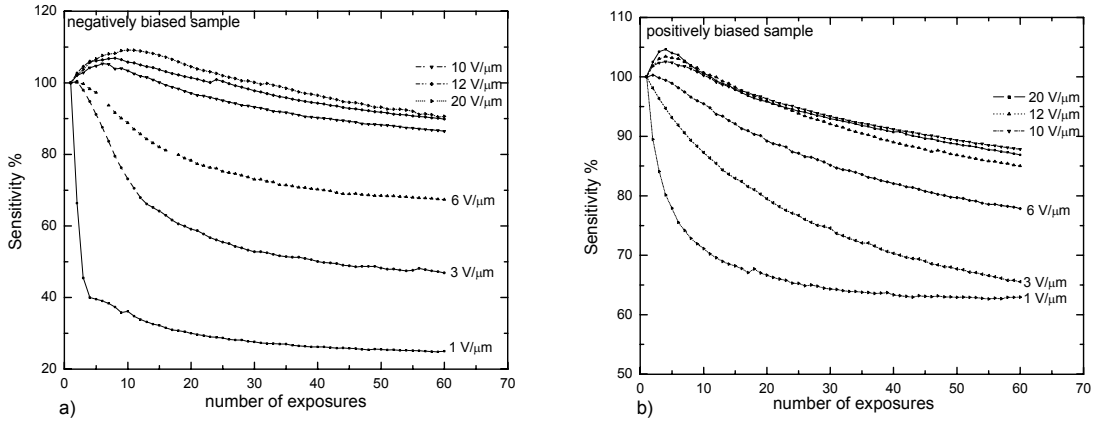

Figure 3.8, The results of the ghosting measurements with 70 seconds time interval for: a) the negatively biased sample; and b) the positively biased sample.

Ghosting measurement of the positively biased sample is shown in Figure 3.8 (b). Although ghosting has the same cumulative exposure and E_{Se} dependence as that in the negatively biased sample, the magnitude of ghosting is lower, especially at lower E_{Se}. This is because the majority of x-rays at mammographic energies are absorbed near the entrance side of the a-Se samples. In the negatively biased sample, as shown in Figure 3.9(a), x-ray generated electrons have to travel essentially the entire thickness of the layer before reaching the readout (bottom) electrode. Whereas in the positively biased sample, as shown in Figure 3.9 (b), the electrons only have to travel to the top bias electrode, which is a much shorter distance compared to in the negatively biased sample. Hence the electrons are much less likely to get trapped. As a result, the density of trapped electrons is less in the positively biased sample, hence lower ghosting. Although the positively biased sample also shows a small increase in x-ray sensitivity for the first several exposures at high E_{Se}, as shown in Figure 3.9(b), the amount of increase is smaller than that in the negatively biased sample. The highest sensitivity is 105 % and 103 % for E_{Se} of 20 V/μm and 10 V/μm, respectively. This is consistent with the lower trapped electron

density and lower dark current for the positively biased sample, which will reduce the effect of the two possible mechanisms indicated above.

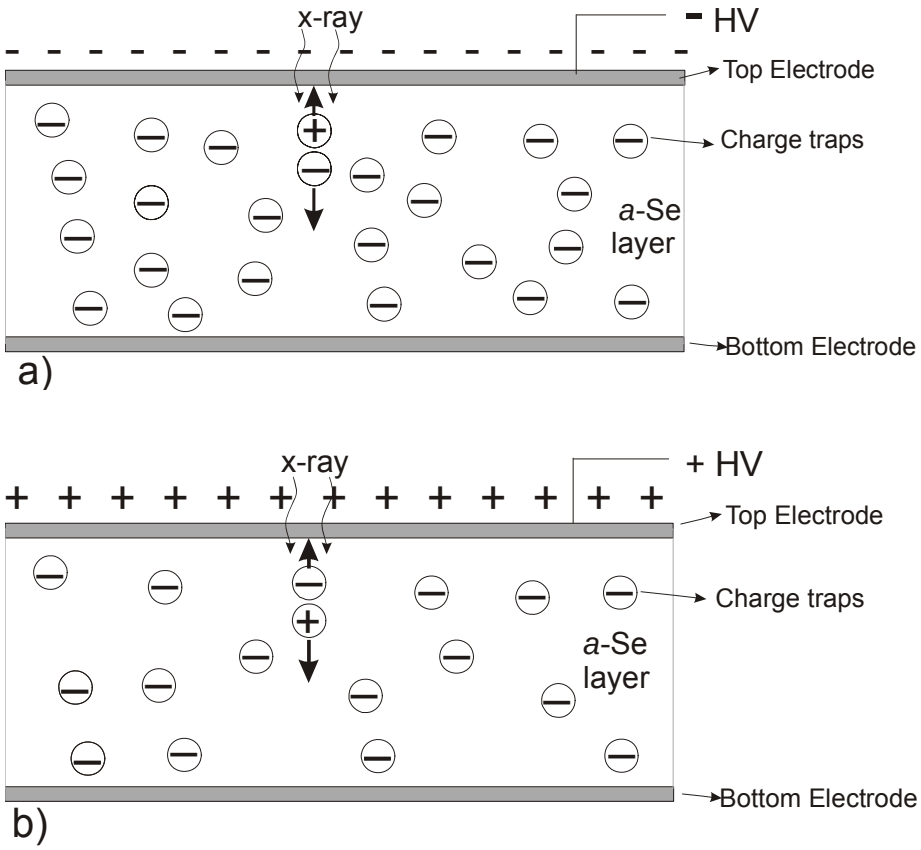

Figure 3.9, Diagrams showing the trapped electron distribution in the a-Se layer for: a) the negatively biased sample; and b) the positively biased sample.

Shown in Figure 3.10(a) are the ghosting measurements with 5 minutes time interval for the negatively biased sample. For the purpose of comparison, the ghosting measurements with 70 seconds time interval at the same E_{Se} (6 and 10 V/μm) are also plotted. Figure 3.10(a) shows that with 5 minutes time interval, the x-ray sensitivity decrease at the end of the experiments is 7 % and 10 % for E_{Se} of 10 and 6 V/μm, respectively. This level of ghosting is much less than that with 70 seconds time interval, which suggests significant recovery of ghosting with the increased time interval. There are two possible mechanisms for recovery: (1) Release of trapped holes. The trapped holes may not have been released

completely with 70 seconds time interval, hence playing a role in ghosting; (2) Neutralization of trapped electrons by injected holes from the bias electrodes through dark current. The longer the time interval between subsequent exposures and the higher the dark current, the more recovery of ghosting there will be.

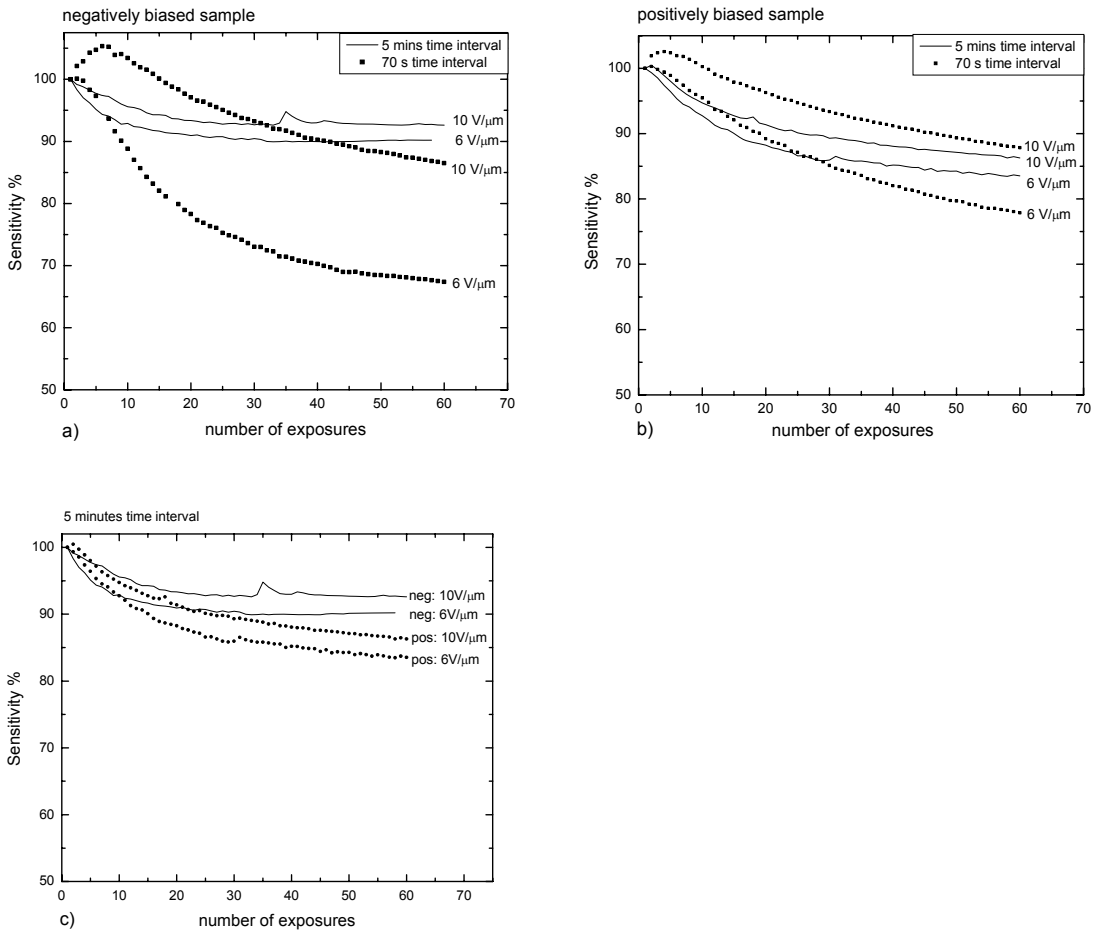

Figure 3.10. The result of ghosting measurement with 5 minutes time interval at applied E_{Se} of 6 and 10 V/μm for a) the negatively biased sample (neg); b) the positively biased sample (pos) and c) comparison between the two samples.

Another noticeable fact in Figure 3.10(a) is that although ghosting with 5 minutes time interval is lower than that with 70 seconds interval at the end of the experiments, it is higher at the beginning. This results in a cross-over between the x-ray sensitivity curves

for the two different time intervals. This may be explained qualitatively by the dynamics of the trapped charge forming in the bulk of a-Se.

Figure 3.11 shows the conceptual trapped charge distribution and the resulting E_{Se} distribution for the two different samples at different time intervals between subsequent exposures. Shown in Figure 3.11(a) is the case for the negatively biased sample. E_{Se} is constant across the layer before any exposures. With 70 seconds time interval, there are unreleased trapped holes in the bulk of a-Se in addition to the trapped electrons. This causes a higher E_{Se} near both bias electrodes, hence a possible increase in x-ray sensitivity for the first several exposures before the recombination mechanism becomes dominant. With longer (5 minute) time interval, there are no trapped holes and fewer trapped electrons (due to recombination with injected holes from the bias electrode), which result in a decreased E_{Se} at the entrance side. Hence the change in E_{Se} also causes a decrease in x-ray sensitivity, and no increase in x-ray sensitivity is observed at the beginning of the experiments (Figure 3.11a). With more x-ray exposures and build-up of trapped electrons, recombination becomes the dominant mechanism which causes a decrease in x-ray sensitivity in both cases.

Shown in Figure 3.10(b) are the ghosting measurements with 5 minutes time interval for the positively biased sample. Although the total amount of ghosting at the end of the experiments is also reduced as a result of the increased time interval at E_{Se} of 6 V/μm, the difference between the two time intervals is not as large as seen in the negatively biased sample. The two curves for E_{Se} of 10 V/μm do not cross over in the exposure range used in our experiments. However, they are anticipated to meet at exposures higher than 60 R based on their shapes. Shown in Figure 3.11(b) is the conceptual trapped charge and E_{Se}

distribution for the positively biased sample at the beginning of the experiments. With shorter time interval (70 seconds) between exposures, the trapped electron density is higher and there are unreleased trapped holes in the bulk.

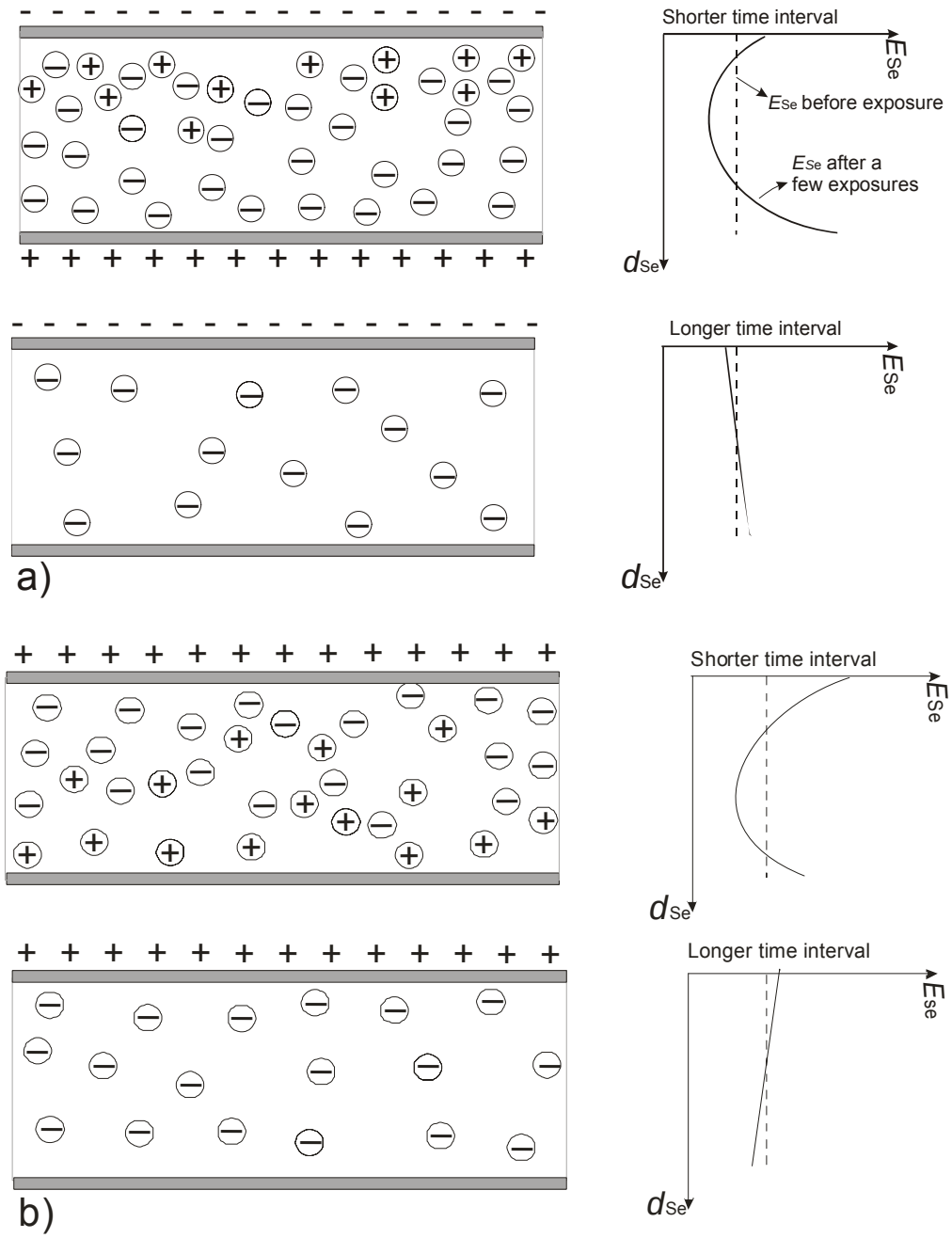

Figure 3.11. Diagrams showing the distribution of trapped charge (left) and E_{Se} (right) for a) the negatively biased sample; and b) the positively biased sample in the ghosting measurement with different time intervals. We assume a uniform distribution of trapped electron in the condition of longer time interval for both samples. Dash line: uniform E_{Se} before any exposure; Solid line: E_{Se} distribution after a few exposures at different experimental conditions.

This results in a higher E_{Se} near both bias electrodes compared to the case for 5 minutes time interval, where E_{Se} decreases monotonically as a function of depth into the layer due to the trapped electrons in the bulk. We believe the enhanced E_{Se} near the top surface is partially responsible (in addition to charge injection from the bias electrodes) for the small increase in x-ray sensitivity for the first several exposures (Figure 3.11b), although the magnitude of increase with 5 minute time interval (< 1 %) is much less than with the 70 second time interval due to the difference in E_{Se} distribution.

In order to demonstrate the impact of dark current on the recovery of ghosting, the measurements with 5 minutes time interval for the two samples are replotted in Figure 3.10(c) for comparison. It shows that the negatively biased sample has less sensitivity reduction than the positively biased sample at the same E_{Se}. This is in contradiction to what was observed with the 70 seconds time interval. This is because the dark current of the positively biased sample is two orders of magnitude lower than that of the negatively biased sample. Hence less trapped charge is neutralized by the injected carriers through dark current. This result suggests that a reset procedure by injection of holes between subsequent x-ray exposures, either through optical exposure on the positive bias electrode or some form of enhanced charge injection, can speed up the recovery of ghosting. This reset procedure by neutralizing trapped charge is different from that used in indirect flat-panel detectors, where electrons generated by reset light are used to fill the traps before the next x-ray exposure[51, 52]. It is expected that with proper reset procedures, the cumulative ghosting can be reduced to the same level as for a single exposure, which has been shown to be < 0.5 % and negligible in prototype a-Se FFDM detectors (Sec. 3.2)[19, 38].

3.4.4 Lag Measurements

The first frame lag was quantified as the percentage residual signal at 0.5 s after the x-ray exposure, which corresponds to a frame rate of 2 frames/second anticipated for tomosynthesis**.** Because lag is strongly dependent on frame rate[38], it is the main component of the temporal performance in tomosynthesis. Ghosting, on the other hand, is the dominant effect for temporal performance in screening mammography.

As shown in Figure 3.2, the dark current was measured both before and after each x-ray exposure. Since in practice the dark current B_0 before an x-ray exposure can easily be sampled and subtracted from each frame, we defined the first frame lag as:

$$l = \frac{B_1 - B_0}{S} \tag{3.4}$$

where B_1 is the dark current measured 0.5 second after an x-ray exposure. For comparison, we also quantified the lag associated with the enhanced charge injection during x-ray exposure, B_X:

$$l_X = \frac{B_X - B_0}{S} \tag{3.5}$$

The value of l_X should be comparable to lag measured at real-time frame rate of 30 frames/second.

3.4.5 Lag: Results

Shown in Figure 3.12 are the results of first frame lag l for the two samples. For E_{Se} > 1 V/μm, lag increases with the number of exposures for both samples. This is because as the density of trapped electrons in the bulk increases with exposure, the electric field at the positive bias electrode gets further enhanced and causes an increase in charge

injection, which is the main mechanism for lag. As shown in Figure 3.12(a), for the negatively biased sample, lag increases significantly from ~ 0 to 12 % with the number of exposures at E_{Se} = 20 V/μm. On the contrary, for the positively biased sample as shown in Figure 3.12(b), lag increases only slightly from ~ 0.15 % to 0.2 % at the same E_{Se}. This is because the amount of trapped charge is lower in the positively biased sample at the same E_{Se}, and the blocking layers in the positively biased sample were better engineered, which was evident from its much lower initial dark current than the negatively biased sample. For E_{Se} = 1 V/μm, lag is essentially constant with the number of exposures for both samples. This is because at such a low E_{Se}, the function of the blocking layer is intact in spite of the existence of trapped charges. Compared with the negatively biased sample, the first frame lag of the positively biased sample is much lower at all E_{Se} used in

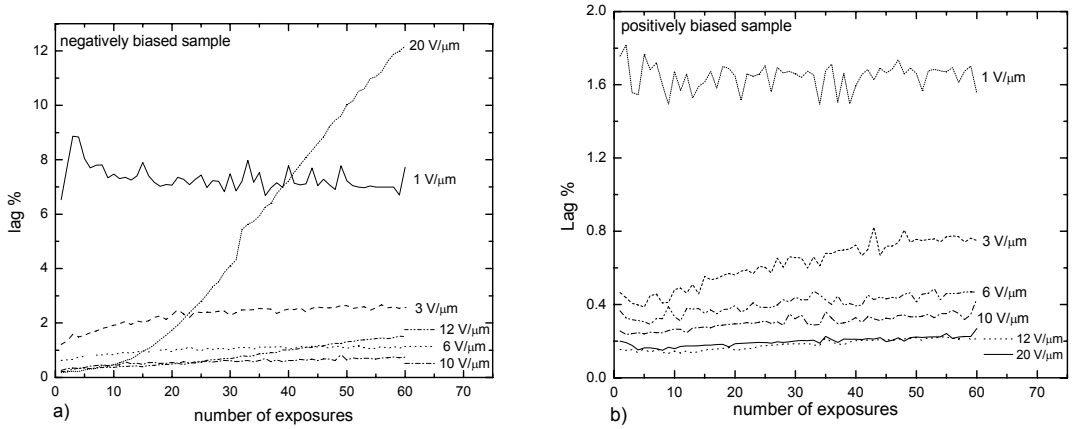

Figure 3.12. The result of the first frame lag (*l*) measurement with 70 seconds time interval for a) the negatively biased sample; and b) the positively biased sample.

our experiments. This is consistent with the fact that the dark current of the negatively biased sample is two orders of magnitude higher than that in the positively biased sample, which suggests that the blocking layers in the negatively biased sample are not as well engineered as the positively biased sample.

The measurements of l_X determined using Eq. 3.5, which is equivalent to the first frame lag at 30 frames/second, are shown in Figure 3.13(a) and (b) for the negatively and positively biased samples, respectively. At E_{Se} > 1 V/μm, the exposure and E_{Se} dependence of l_X is similar to that of l shown in Figure 3.13 for both samples. The magnitude of l_X is about four times that of l for the same sample and E_{Se}. This is mainly because B_1 is much lower than B_X, which drops to B_1 after 0.5 seconds. At the extremely low field of E_{Se} = 1V /μm, l_X follows a different exposure dependence, i.e. decreasing as a function of the number of exposures. The mechanism for this behavior is not clear and needs further investigation. For the most commonly used E_{Se} of 10 V/μm for commercial direct flat-panel detectors, the value of l_X is 1 % for the positively biased sample and 4 % for the negatively biased sample. This is compatible to the measured result (4 %) for a real-time prototype a-Se flat-panel detector[53].

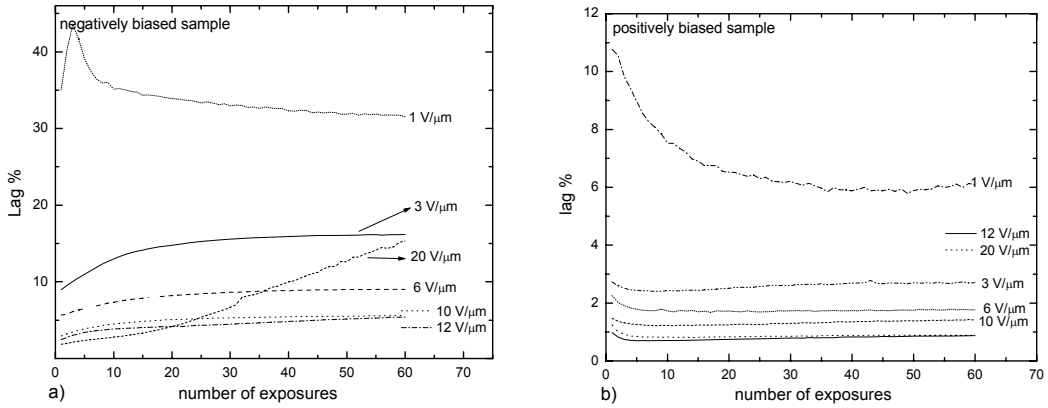

Figure 3.13. The result of l_X measurement with 70 seconds time interval for a) the negatively biased sample; and b) the positively biased sample.

From our investigation of lag and ghosting in two different a-Se samples, we can conclude that biasing the x-ray entrance side of the sample positively can lead to lower ghosting. Samples with higher dark current have higher lag, however dark current caused

by charge injection can speed up the recovery of ghosting by neutralizing the trapped electrons with injected charge carriers. The x-ray spectrum of 28 kVp Mo/Mo chosen in our experiment was based on the current clinical practice of screening mammography. Recent studies have shown that digital mammography may benefit from higher energy x-ray beams[54]. It is expected that higher energy x-ray beams delivered with the same glandular dose will increase the x-ray signal per unit exposure, and lead to a faster approach to equilibrium. However because the electron trap density in a-Se is the same, the change in ghosting as a function of cumulative exposure and E_{Se} is expected to be similar to that measured at 28 kVp Mo/Mo.

3.4.6 Conclusions

We have quantitatively investigated the temporal performance, i.e., ghosting and lag, of two small area a-Se detectors, one positively and the other negatively biased at the x-ray entrance side, as a function of cumulative radiation exposure and E_{Se}. The applied electric field E_{Se} ranged from 1 to 20 V/μm. It was found that lag changed slowly with radiation exposure at E_{Se} < 10 V/μm for both samples. At commonly used E_{Se} = 10 V/μm in a-Se flat-panel detectors, lag is negligible (< 1 %) for both samples. Ghosting was found to increase as a function of exposure and decrease with increasing E_{Se}. With shorter time interval (70 seconds) between exposures, ghosting in the positively biased sample is less than in the negatively biased sample due to the lower probability of electron trapping. With longer time interval (5 minutes), less ghosting is observed in the negatively biased sample due to its higher dark current (charge injection), which causes

injected holes from the bias electrode to neutralize the trapped electrons. We found that at E_{Se} = 10 V/μm, the dark current in the negatively biased sample reduced the cumulative ghosting from 12 % to 7 %. It is expected that with proper reset procedures in a-Se detectors where a sufficient number of holes are injected either through optical exposure or charge injection from the bias electrodes, the cumulative ghosting can be reduced to the same level as a single exposure, which has been shown to be negligible in an a-Se FFDM detector.

Chapter 4

Detector Imaging Performance Evaluation in a Prototype Breast Tomosynthesis System

Breast tomosynthesis is implemented by modification of existing screening mammography gantry and digital detectors. In the last two chapters, the a-Se detector designed for mammography has been studied in the context of both screening mammography and tomosynthesis. Due to the lack of an x-ray unit dedicated for breast tomosynthesis, it was difficult to investigate the imaging performance completely in the context of tomosynthesis. The purpose of this chapter is to investigate the detector performance, both temporal and spatial, in different operational modes designed for tomosynthesis acquisition, e.g. binning or full resolution readout, the range of view angles and the number of views.

4.1 Introduction

Since breast tomosynthesis uses a limited angular range, which is insufficient for artifact free reconstruction of the 3-D information, the majority of existing research efforts were devoted to the development and comparison of different reconstruction algorithms[14, 55, 56]. Very few investigations have been focused on the effect of acquisition geometry and detector performance. Ren *et al* studied the resolution characteristics of a Hologic prototype breast tomosynthesis system equipped with amorphous selenium (a-Se) digital detector with a pixel size of 70 μm[10]. Bissonnette *et al* studied the detector performance for the Siemens prototype breast tomosynthesis

system and presented the preliminary clinical breast imaging results[13]. Both systems employed continuous motion of x-ray tubes during image acquisition to minimize system instability and scan time, and FSB due to tube motion was considered as an important factor for spatial resolution[10]. Previously we built a computer simulation platform for breast tomosynthesis to investigate the effects of detector performance and acquisition geometry on image quality[57]. The in-plane MTF was calculated from reconstruction of simulated projection images of a W wire, and the results were compared for different acquisition geometry and reconstruction algorithms. It was found that pixel binning is the dominant source of image blur compared to FSB (due to tube motion) and reconstruction filters.

In the present study, we experimentally characterized the detector performance using a prototype breast tomosynthesis system. The detector performance was evaluated in the context of tomosynthesis acquisition, which differs from screening mammography in the following aspects: 1. the x-ray exposure per image was 1/*N* of that used in screening mammography; 2. the tube travels continuously during x-ray exposure, which causes additional FSB; 3. the images are acquired at much higher frame rate (up to 2 frames per second) and pixel binning is an option to trade resolution for frame rate; 4. the x-rays could enter from an oblique angle to the detector surface. Physical properties of the detector were characterized using MTF, NPS and DQE at different detector and system operational conditions. The temporal performance was categorized as lag and ghosting, and was measured as a function of exposure.

4.2 System operation

The prototype breast tomosynthesis system (Siemens Mammomat Novation^{Tomo}) [1] was modified from a mammography screening unit (Siemens Mammomat Novation^{DR}). As shown in Figure 4.1, the breast is compressed above a stationary a-Se FFDM detector. The COR of the x-ray tube is 4.5 cm above the detector carbon fiber surface, which is ~1.5 cm above the surface of the a-Se layer. The SID is 65 cm, the same as that in screening mammography. The a-Se detector has a dimension of 24 cm x 30 cm and a pixel pitch of 85 μm, resulting in an image size of 2816 x 3584. The detector can be read out with full resolution or 2x1 binning (with binning in the tube travel direction), which shortens the image readout time by 50%. The readout time for each frame was 0.6 and 0.3 second, respectively, for full resolution and 2 x 1 pixel binning modes. The detector was operated in a repeated "integrate and read" sequence, with a signal integration window of 0.2 second between subsequent detector readout. The detector binning was accomplished by operating two adjacent gate lines at the same time. The x-ray tube travels continuously in an arc within a nominal angular range of ± 24^o, and x-ray pulses are generated within the integration window of the detector for each frame. The true angular position of the x-ray tube for each view was measured with a galvanometer (physically placed in the tube column) at the beginning of each x-ray exposure, and the measurements were used later to set up the accurate geometry for image reconstruction. The number of views in each acquisition can be varied from 11 to 49 and FBP algorithm was used to reconstruct the image slices parallel to the detector surface. The x-ray tube had nominal focal spot sizes of 150 and 300 μm, and target material choices of Mo and W. The target/filter combination of W/Rh with nominal Rh filter thickness of 50 μm was

[1] Caution: Investigations Device. Limited by US Federal law to investigational use. The information about this product is preliminary. The product is under development and is not commercially available in the US; and its future availability cannot be ensured.

chosen for all our measurement, because compared to Mo target it delivers harder x-ray spectrum at higher tube current, which allows shorter x-ray exposure time and higher dose efficiency for tomosynthesis. Our previous theoretical calculation showed that the optimal kVp for an average breast thickness of 4 cm is ~28 kVp with W/Rh combination[11]. Hence this spectrum was used for all our measurements of NPS and DQE. During the experiment, a 3.95 cm Lucite block was inserted to the tube output to mimic the attenuation of an average breast. The x-ray exposure, given in mR/mAs, was measured using a Keithley dosimeter (model 35050 A) and an ion chamber (model 35050 B).

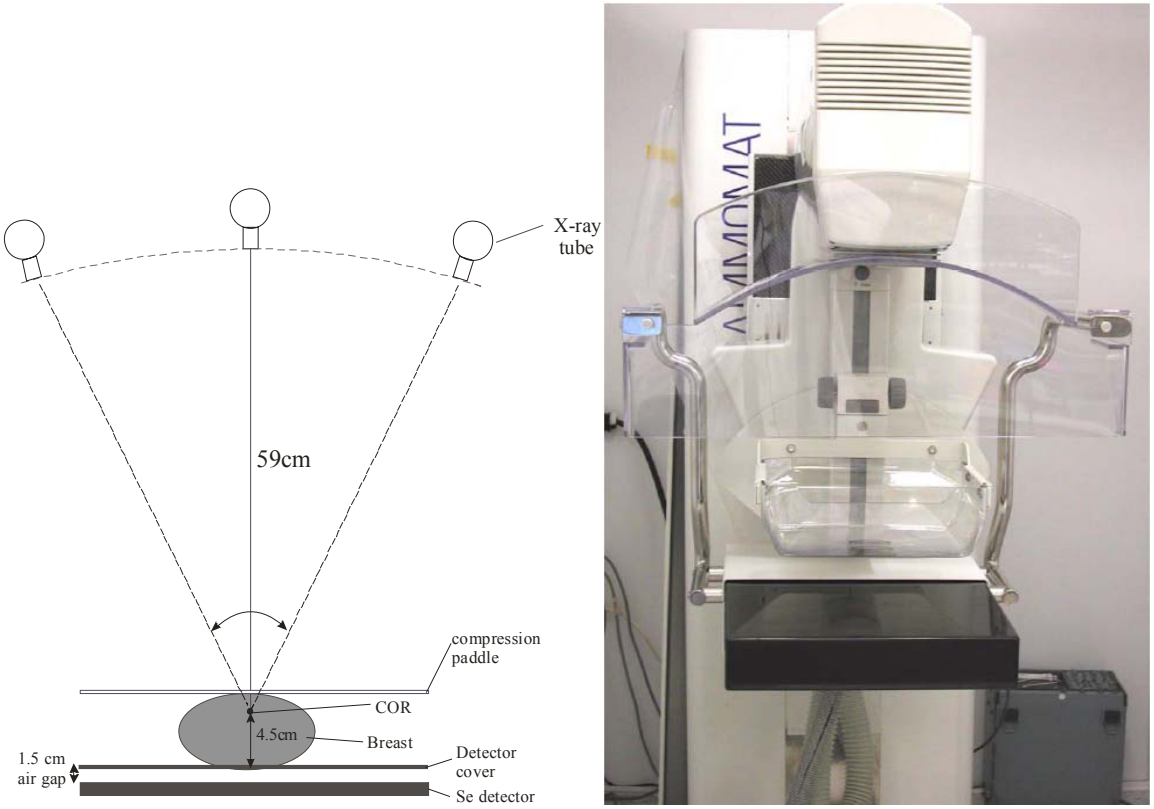

Figure 4.1. a) Geometry of the prototype breast tomosynthesis system, b) A photograph of the prototype tomosynthesis system used in our investigation.

Table 4.1 shows examples of the image acquisition modes available on the prototype system. They differ in detector resolution (binning or full resolution), number of views,

gantry travel speed, and whether an offset image is acquired between two subsequent x-ray images. The abbreviated name we have chosen for each acquisition mode has the following meanings: 'x' refers to x-ray frames only; 'xb' refers to offset frame acquired between subsequent x-rays; the number refers to the number of views for each scan, and 'bin' means the detector was operated in binning mode. The modes with 'Zero' in the front mean that the gantry rotation was disabled during the acquisition of the image sequence. These modes were usually used during physics investigation of the detector performance.

Table 4.1, Available acquisition modes for tomosynthesis scanning

Imaging geometry		Detector operational mode		Scan time	
Mode name and angular range	No. of views	Dark frame between x-rays	Pixel binning	Gantry speed (cm/s)	Scan time (s)
x49:±20°	49	No	No	1.2	40.7
x25:±20°	25	No	No	2.4	20.8
xb25:±20°	25	Yes	No	1.2	41.6
x25bin:±21°	25	No	Yes	3.9	12.7
xb25bin:±22°	25	Yes	Yes	1.9	25.4
x19:±21°	19	No	No	3.1	15.8
xb15:±20°	15	Yes	No	2.0	24.9
Zero xb25: 0°	25	Yes	No	0	46.5
Zero x 25bin: 0°	25	No	Yes	0	12.7
Zero xb25bin:0°	25	Yes	Yes	0	25.4

4.3 MTF

In breast tomosynthesis, three factors affect the spatial resolution of the projection images: 1. inherent detector resolution; 2. FSB due to the motion of the x-ray tube; and 3. the oblique entry of x-rays. The inherent resolution of a-Se detectors is determined mainly by the pixel pitch. In screening mammography, the size of the focal spot (nominally 100 and 300 μm) rarely causes degradation of spatial resolution because there

is very little magnification. In most tomosynthesis systems, however, the x-ray tube travels continuously during x-ray exposure (for stability of the gantry), and causes significant increase in the effective focal spot. The effective focal spot size is proportional to the product of the gantry travel speed and the x-ray exposure time for each view, which varies with dose and imaging geometry. Since detector binning is in the tube travel direction, its effect on spatial resolution should be compared with that due to focal spot motion (FSM).

The measurement of the presampling MTF was same as that described in Chapter 2. The slit phantom was placed on top of the detector cover, which is 1.5 cm above the a-Se layer. The slit was placed close to chest wall and aligned to the center of the detector. The x-ray exposure (to the detector) used for acquiring each slit image was 104 mR. To include the effect of FSB, the images were acquired with tube motion in two modes: 'x25bin' and 'x19', where the gantry speed (shown in Table 4.1) is the largest for pixel binning and full resolution modes, respectively. The exposure time per view was ~164 ms, resulting in a FSM of 6.4 mm and 5.2 mm, respectively for 'x25bin' and 'x19'. Since the radiation at oblique angles was cut off by the narrow slit, only the central view of the tomosynthesis acquisition was used to determine the detector MTF with FSM. It is important to note that the maximum exposure time of 164 ms per view was used for the acquisition of slit images to minimize the effect of noise on the determination of oversampled LSF. In tomosynthesis scans of an average breast thickness, the exposure time is typically 1/5 of what was used. Hence the effect of FSM in our measurements was the worst case scenario. With a given tomosynthesis geometry, which determines the

magnification, the effect of FSM on presampling MTF can be easily calculated. The calculated results were compared to the measured presampling MTF with the FSM.

Another factor affecting the MTF in tomosynthesis is the oblique entry of x-rays, which has been studied previously for a-Se flat-panel detectors[58-61]. In our prototype system, the detector remains stationary while the x-ray tube rotates around the COR. A maximum tube angle of 20° corresponds to an oblique entry angle of 18^o and 30^o, respectively, for the center and far edge of the detector. Using the method described in Ref,[61] the MTF due to oblique entry of x-rays was calculated. The MTF due to oblique angle was also measured by the slanted-edge technique[62-64]. A 250 μm thick W edge was placed in the center of the detector close to the chest wall side. The images were acquired at two tube column angles (with respect to the surface of the detector) of 0^o and 23^o, which correspond to detector x-ray entry angles of 0^o and 21^o, respectively, according to the system geometry shown in Figure 4.1(a). The edge images were used to calculate the edge spread function (ESF), the derivative of which formed the LSF. The MTF was obtained by Fourier transform of the LSF. The additional blur due to oblique entry of x-rays was obtained by dividing the MTF at angle θ by that at angle 0^o:

$$MTF_{Obl}(f,\theta) = \frac{MTF(f,\theta)}{MTF(f,0^o)} \tag{2.1}$$

Figure 4.2(a) shows the presampling MTF with and without pixel binning. The MTF shown is in the data-line (binning) direction, and the effect of binning on the first zero of the presampling MTF is clearly indicated. Also shown in Figure 4.2(a) is the measured presampling MTF with gantry motion. The measured presampling MTF with FSM agrees well with calculation. The effect of FSM, however, increases with the distance of the object from the detector surface due to magnification. Figure 4.2(b) shows the calculated

presampling MTF due to FSM for an object plane that is ~ 4 cm from the detector surface. The detector presampling MTF without FSM in the full resolution and binning modes are shown in the same graph for comparison. The total exposure, which is 28 kVp and 144 mAs with W/Rh target/filter combination, corresponds to the glandular dose of 1.7 mGy for a 4 cm breast with average composition. Three imaging modes with total scan time of 20 seconds or less were chosen. The FSM is 1.15 mm, 1.26 mm and 0.65 mm, respectively, for the imaging modes of 'x25bin', 'x19' and 'x25'. It shows that the blur due to FSM is dominant for mode 'x19' and comparable to the detector inherent MTF for mode 'x25'. We can predict that for full resolution mode with fewer number of views (<19), which results in faster gantry travel, FSB will be the dominant factor for presampling MTF. In binning mode ('x25bin'), the aperture function is the dominant source of blur. The blur due to oblique x-ray entry alone is shown in Figure 4.2(c). The measured result at 21^o agrees well with that from theoretical calculation. Also plotted in the same graph are the calculated results for the range of oblique angles (18^o-30^o) expected for our tomosynthesis geometry. In the worst case of 30^o, which corresponds to the far side of the detector with the x-ray tube column at the maximum angle, the blur due to oblique x-ray entry causes MTF to decrease by 28% at f_{NY} (5.88cycles/mm). This calculated MTF is added to the graph in Figure 4.2(b) for comparison with other factors. It shows that FSB or pixel binning are the dominant effects of blur in tomosynthesis image acquisition.

The practical advantage of pixel binning is to shorten scan time. When binning is performed in the scan direction, its effect on image blur should be compared with FSB.

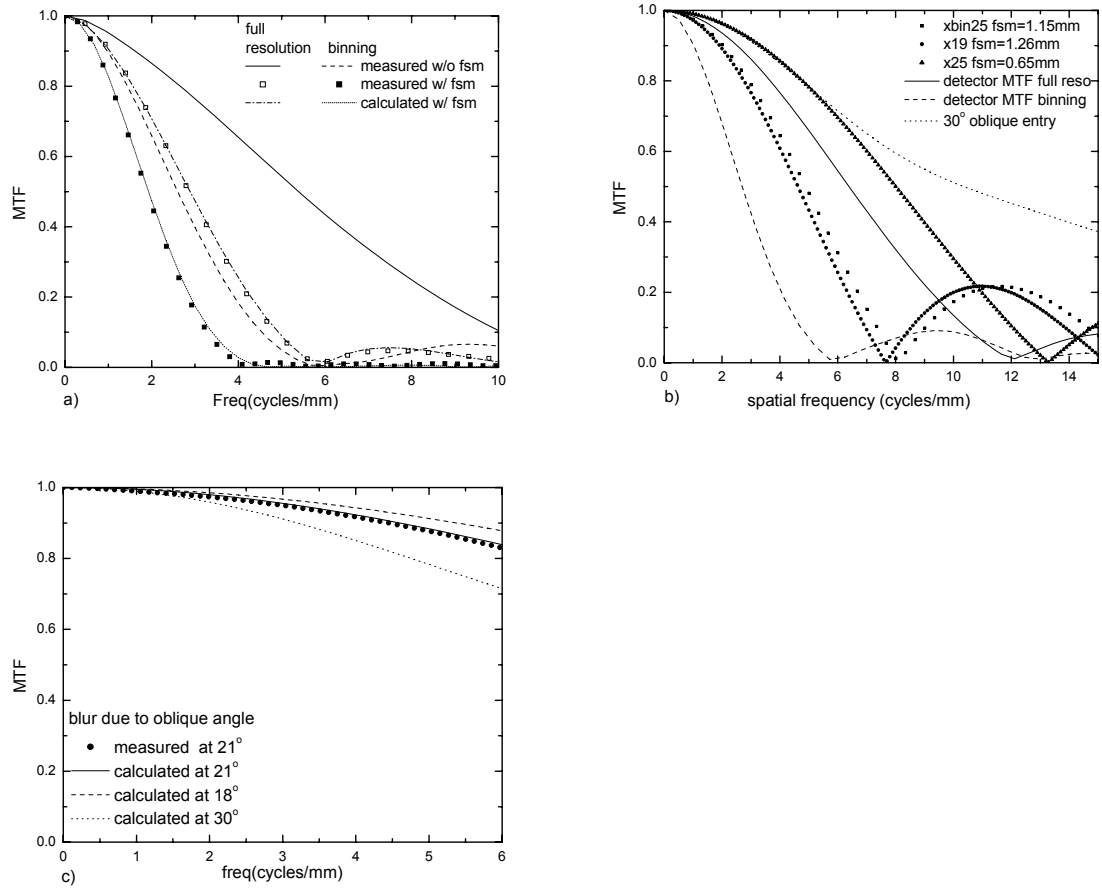

Figure 4.2. a) presampling MTF measured from the system; b) a comparison of MTF due to detector inherent resolution, FSB and oblique entry angle; c) Calculated and measured MTF due to oblique x-ray entry alone.

Even with full resolution readout, the MTF in the scan direction is degraded by FSB due to continuous tube motion. Therefore the relative degradation of MTF due to pixel binning is not as severe as in screening mammography with stationary gantry, or in a step-and-shoot tomosynthesis system. Whether binning mode should be used in tomosynthesis depends ultimately on its impact on the detectability of objects, most notably microcalcifications. This topic is beyond the scope of the present investigation, which focuses on the detector performance in different image acquisition modes.

4.4 X-ray sensitivity and NPS

NPS was measured for x-ray exposures ranging from 0.4 to 5.7 mR in both binning and full resolution modes. Two imaging modes without gantry motion were used: 'Zero x25bin' and 'Zeroxb25'. To minimize the effect of lag on NPS measurements, only the first image from each tomosynthesis acquisition was used for the calculation. Offset and gain correction was applied to each image, and a uniform area with 512 x 512 pixels at the center of the chest wall side of the detector was chosen as ROI. The x-ray response of the detector at each exposure was calculated by averaging the pixel values in the ROI. Each ROI image was then divided into 16 sub-images, each with 128 x 128 pixels. Two tomosynthesis sequences were acquired at each exposure, hence 32 realizations of NPS were generated. The 2-D and 1-D NPS was then calculated the same way described in Chapter 2.

Figure 4.3 shows the pixel response, in analog-to-digital units (ADU), measured as a

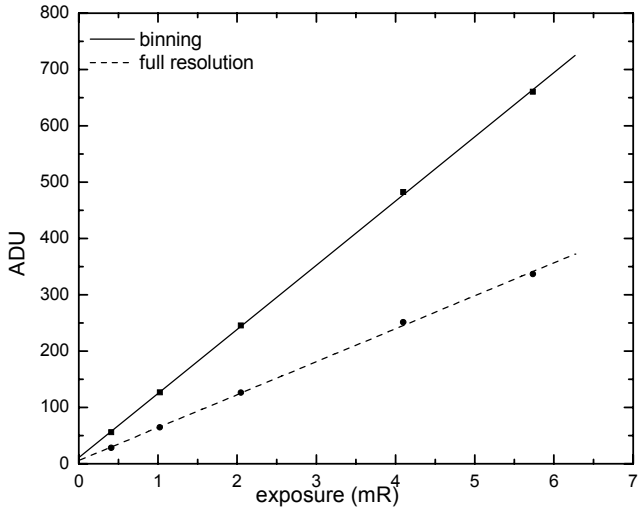

Figure 4.3. Pixel response of the detector in full resolution and binning modes as a function of x-ray exposure. Measured data are shown with symbols and linear fitting shown with straight lines. ADU/mR = 58.5 for full resolution and 114 for binning mode.

function of x-ray exposure in both full-resolution and pixel binning modes. The pixel x-ray sensitivity was determined from the linear fitting of the measurements, and results were 58.5 ADU/mR and 114 ADU/mR, respectively, for full resolution and binning modes. The sensitivity in binning mode is approximately twice that with full resolution, which is to be expected from the doubling of effective pixel size in binning direction.

Figure 4.4 (a) shows the dark NPS of the detector measured without x-ray exposure. The NPS(0) for binning mode is approximately 3.5 times that for full resolution mode. However since the f_{NY} in the data-line direction (binning direction) is reduced to one half due to binning, the integrated NPS, which is equal to the pixel variance σ^2_p, in binning mode is ~1.7 times that in full resolution mode. Since charge amplifier noise is independent of pixel binning, the fact that σ^2_p almost doubled with binning means that other sources of electronic noise, e.g. pixel reset noise and gate line correlated noise,[65] that scale with pixel binning make significant contributions.

Figure 4.4(b) shows the measured NPS in the dataline (binning) direction at different detector exposures in both full resolution and binning modes. The NPS is essentially white throughout the frequency range. This is consistent with our previous theoretical investigation[19]. The NPS (0) in binning mode at high exposures, e.g. 6 mR where the effect of electronic noise is negligible, is approximately four times that for full resolution mode, which means that the integrated NPS (pixel variance σ^2_p) doubles with pixel binning. This is consistent with the scaling of x-ray quantum noise with pixel size. At the low exposure of 0.4 mR, the contribution of electronic noise to the total NPS is <10 % for both modes. This indicated that the system is essentially x-ray quantum noise limited for tomosynthesis imaging.

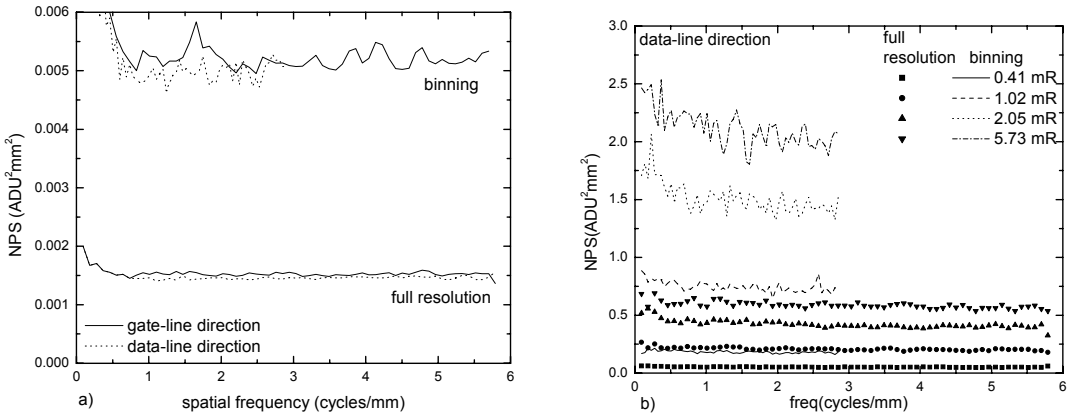

Figure 4.4. (a) Measured electronic noise NPS (in orthogonal directions of the detector) in both full resolution and pixel binning modes; (b) NPS at different detector exposures for both modes. For clarity, only NPS in the data-line (binning) direction is shown. The Nyquist frequency f_{NY} of NPS is 5.88 and 2.94 cycles/mm, respectively, for full-resolution and binning modes.

4.5 DQE

The calculation of DQE was described in Sec. 1.7 and 2.6. The x-ray spectrum used in our NPS measurements (28 kVp W/Rh with 3.95 cm Lucite) was modeled using Boone's parameterization method[34, 35], from which the value for q_0 was calculated as 5.83×10^4 photons/mm^2/mR.

The DQE is plotted as a function of spatial frequency and exposure for both modes in Figure 4.5. There is a noticeable decrease in DQE for spatial frequencies of $f < 0.5$ cycles/mm, which is due to a corresponding increase in NPS in the same frequency range. This phenomenon was investigated previously and attributed to the image correction algorithms, which introduced additional noise at low spatial frequencies[19]. The DQE (f) essentially follows the shape of MTF^2(f) because there is very little spatial correlation in the measured NPS. Hence the DQE (f) in binning mode drops more rapidly as spatial frequency increases. At the lowest exposure of 0.41 mR used in the measurements, the DQE (0) drops from the maximum value of ~0.58 to 0.5 due to the degradation effect of

electronic noise. There is no significant difference in DQE (0) between the two modes because the degradation effect of electronic noise is comparable, as shown in Figure 4.4(a).

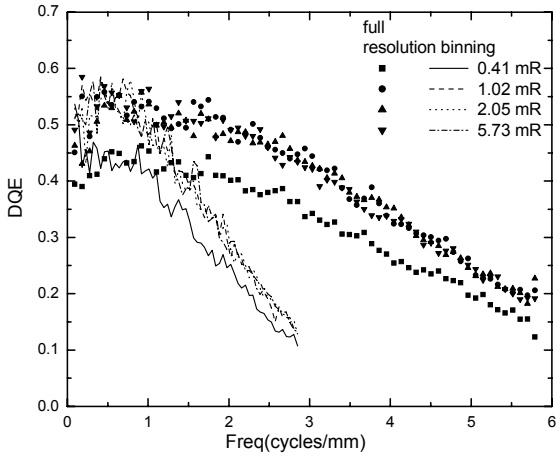

Figure 4.5. Measured detector DQE at different exposures in full-resolution and binning modes. Individual symbols are used for the results in full resolution mode, and lines used for the binning mode.

4.6 Temporal performance: Lag

Due to the rapid image acquisition required for tomosynthesis, temporal performance of the detector plays an important role. Lag and ghosting of the a-Se flat-panel detector was investigated as a function of x-ray exposures and detector operational modes used in tomosynthesis.

Lag was measured with the detector operated in either full resolution or binning mode, with corresponding time interval between subsequent images of 0.8 and 0.5 second, respectively. The measurement was performed without gantry motion. The x-ray exposures chosen for the lag measurement is relevant to tomosynthesis acquisition. We assumed that the total dose for a tomosynthesis scan is equivalent to a single view screening mammogram, which is ~1.6 mGy for a 4 cm breast with average density according to a national survey of digital mammography[66]. With the spectrum used in

our experiment (28 kVp W/Rh), this corresponds to a mean detector exposure behind the breast of ~ 30 mR, i.e. ~1.2 mR per view with 25 views. Under the same exposure condition, the detector exposure for areas outside the breast is ~ 455 mR in screening and ~18.2 mR per view in tomosynthesis. The image acquisition sequence for the measurement of lag is shown in Figure 4.6, where an offset image was acquired before a single x-ray exposure, which ranged from 0.5 to 15 mR. After the x-ray frame, N_d = 25 dark images were acquired. The x-ray and trailing dark images were corrected by subtracting the offset frame acquired before the x-ray exposure. The full x-ray signal and residual signal were computed using a 400 x 400 pixel ROI within the radiation field. Lag was quantified as the ratio between the residual signal in each dark frame and the full x-ray signal, and was examined as a function of time at different exposure levels.

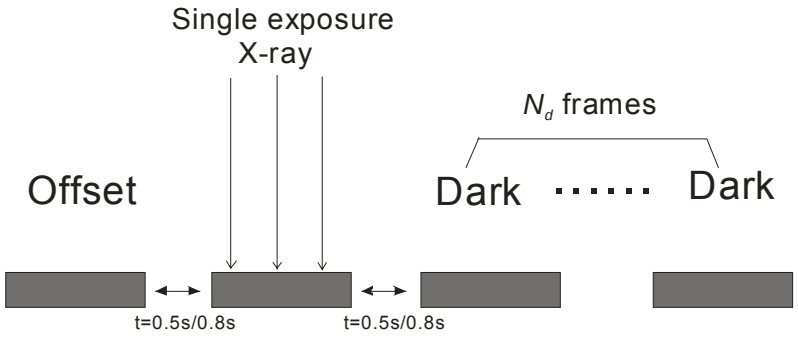

Figure 4.6. Diagram showing the image sequence used in lag measurement: An offset image was acquired before x-ray exposure, and N_d image frames were acquired after a single x-ray exposure. The x-ray exposure varied from 0.5~15mR. The time interval between subsequent image views is 0.5s and 0.8s, respectively for binning and full-resolution modes.

The results of lag measurements plotted as a function of frame number are shown in Figure 4.7(a) and (b), respectively, for the full resolution and binning modes. Figure 4.7(a) shows that with full resolution readout (frame interval of 0.8 second), the first frame lag of ~4-5 % is relatively independent of x-ray exposure. After the second frame, the relative percentage of lag starts to show an inverse dependence on exposure. This is

because two mechanisms contribute to lag in a-Se: (1) detrapping of charge from shallow traps; which is proportional to x-ray signal; and (2) the increase in charge injection from the positive bias electrode due to an increase in electric field at this interface as a result of electrons captured in deep traps in the bulk. The first mechanism is dominant for the first frame lag, hence the residual signal exhibits a constant fraction of the x-ray signal. The second mechanism is dominant for the remainder of the lag measurements. Since the increase in charge injection depends on the nature of metal contact (barrier height) and blocking layers, it is not expected to be directly proportional to exposure, but rather reaching a steady state with time that is independent of exposure. Hence its relative effect on lag is less at higher exposures.

Shown in Figure 4.7(b) are the measurements of lag with 2x1 pixel binning. Due to the shorter time interval (0.5 second) between frames, the first frame lag of 8-9 % is almost twice that with full resolution readout. After the second frame, the lag is < 3 %, and is essentially at the same level as that with full resolution readout. This is consistent with the second lag mechanism being dominant. From Figure 4.7 we can conclude that in the 'xb' modes listed in Table 4.1, where a dark frame is acquired between subsequent exposures and used for offset correction, would not be beneficial to image quality because: (1) the dark frame would overestimate the contribution of lag and result in an over-correction; (2) the correction will double the electronic noise power in the final image, and increase the degradation effect of electronic noise at the low exposures used in tomosynthesis. It has been shown in CBCT that temporal image persistence on the order of ~ 5 % will not result in significant image artifact[67, 68]. Since the reconstructed images in tomosynthesis suffer from inaccuracy due to incomplete sampling[69], the

effect of temporal artifact is expected to be less critical compared to CBCT. Possible strategies for minimizing the effect of lag would be to discard the dark frame acquired between x-ray frames, and use the 'xb' modes just to increase the time interval between two subsequent x-ray frames. However this is at the cost of increased scan time and its associated risks of patient motion. Since the quality of reconstructed images is susceptible to artifact introduced by patient motion, to decrease the scan time becomes more important. Therefore for patient imaging the modes without additional dark frame acquisition are more desirable.

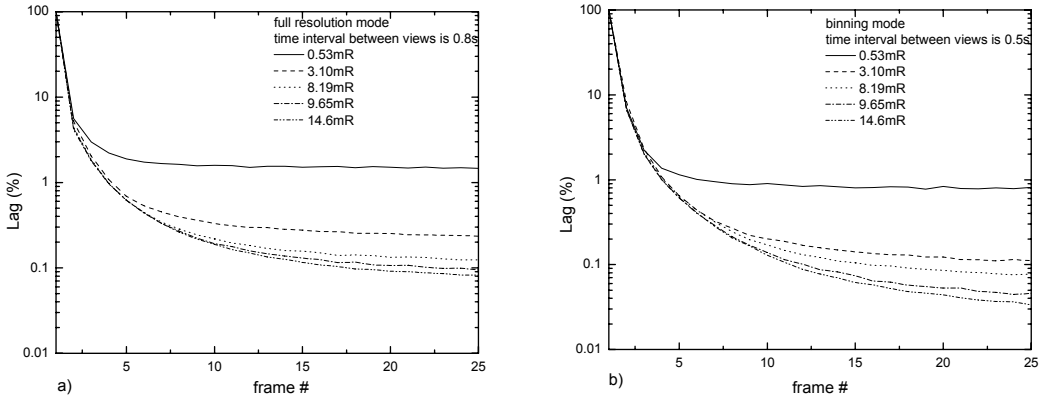

Figure 4.7. Lag as a function of frame number measured at different detector exposures for: (a) full resolution; and (b) binning mode.

4.7 Temporal performance: Ghosting

In tomosynthesis, ghosting will most likely cause an artifact near the edge of the breast, where the detector could receive raw exposure in one view and behind the breast in the next. The image acquisition sequence used in our ghosting measurement is shown in Figure 4.8. All images were acquired with full detector resolution and no gantry motion. The reference x-ray sensitivity (without ghosting) was first established using exposures comparable to that received by the detector behind the breast per view (0.4-5 mR). The

ghosting dose ranged from 10 mR to 1 R, and was 17-170 times the reference exposure. Due to the limited x-ray integration time in tomosynthesis (0.2 second), the maximum detector exposure that can be delivered per view was 0.1 R. Therefore several (N_x) consecutive exposures were made to achieve the total ghosting exposure. Since ghosting is a long term effect, the "ghosted" x-ray sensitivity at the same reference exposure was measured several frames ($N_d > 10$) after the ghosting dose was delivered so that the effect of lag was minimized. All the x-ray images were corrected for offset and gain non-uniformity. Ghosting was quantified as the ratio between the "ghosted" sensitivity and the reference sensitivity, and was examined as a function of ghosting exposure.

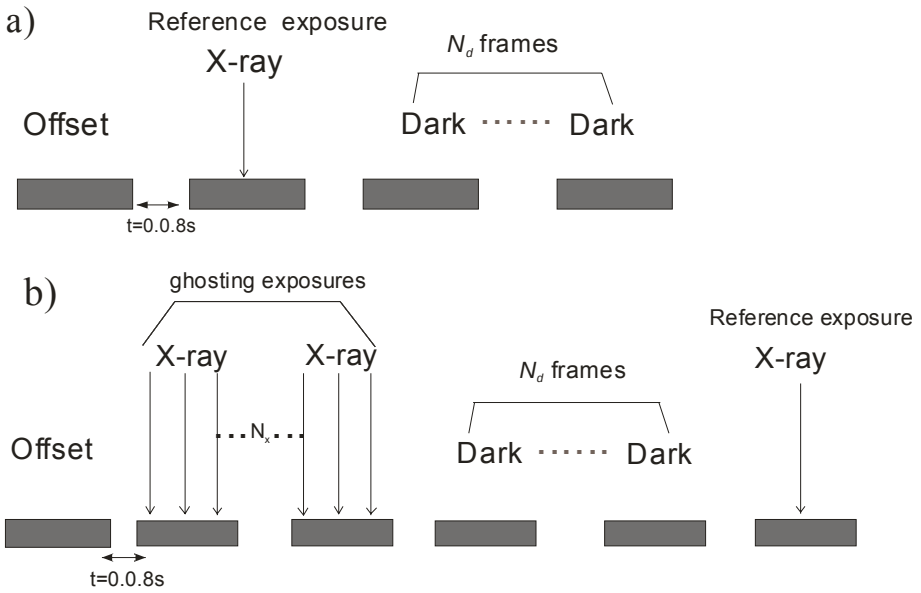

Figure 4.8. Diagram for ghosting measurement, x-ray sensitivity was measured at a reference exposure before (a) and after (b) ghosting exposures. The exposure for ghosting ranged from 10-1000 mR. Ghosting is quantified as ratio of sensitivity at reference exposure before and after ghosting exposure.

Figure 4.9 shows the results of ghosting measurements, where the normalized x-ray sensitivity is plotted as a function of ghosting dose. It shows that ghosting causes a slight increase in x-ray sensitivity for the dose range used in our investigation. The sensitivity increases by 4% after a single exposure of 10.0 mR. This means that the first mechanism for ghosting (Sec. 3.1), i.e. change in x-ray to charge conversion gain as a result of

trapped electrons in the bulk, was dominant. This observation was consistent with our previous investigation using electroded a-Se samples (without TFT readout)[41]. The electrons captured in deep traps causes an increase in the electric field at the x-ray entrance side (positively biased) of the a-Se layer, where the majority of the x-rays are absorbed due to the relatively low x-ray energy used in mammography. Therefore the first ghosting mechanism leads to an increase in x-ray sensitivity. Part of the increase in sensitivity can also be due to charge trapping between pixel electrodes[37]. which causes an increase in effective fill-factor.

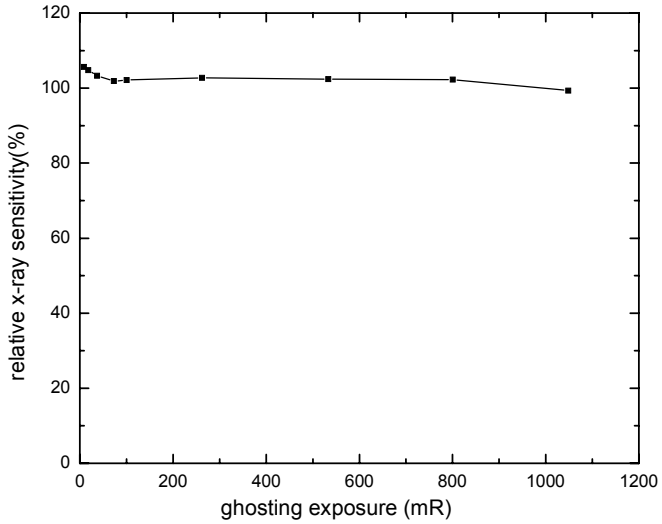

Figure 4.9. Ghosting measurement, quantified as sensitivity at reference exposure as a function of ghosting exposure

Also shown in Figure 4.9 is that as the ghosting dose increases, the relative x-ray sensitivity decreases. The relative sensitivity decreases to 99 % after a ghosting exposure of 1R. This indicates that the second mechanism, i.e. the recombination of trapped electrons with free holes, becomes more significant with increase in dose, and eventually dominates ghosting. It should be noted that trapped charge due to irradiation cannot be

cleared between tomosynthesis views, hence the maximum ghosting dose that is relevant to tomosynthesis is the total raw exposure to detector during the entire scan. Between subsequent tomosynthesis scans, the trapped charge can be cleared in the same fashion as that used in screening mammography. Previous ghosting measurements of a-Se detectors in screening mammography showed that with ghosting clearance procedures between subsequent exposures, the change in x-ray sensitivity is ~0.2 % with ghosting dose of > 3 R[19].

4.8 Conclusions

The imaging performance of an a-Se flat-panel detector in a prototype breast tomosynthesis system was fully characterized. The spatial frequency dependent metrics depend on both the inherent properties of the a-Se detector and the imaging geometry. It was found that for view numbers of 25 or above, the dominant source of blur is pixel aperture function. For fewer views with faster gantry travel, the blur due to focal spot motion becomes dominant. The detector performance is essentially x-ray quantum noise limited down to an exposure level of 0.4 mR. The temporal performance of the detector was quantified for the frame rates and exposure range experienced in tomosynthesis, and is expected not to degrade the reconstructed image quality.

Chapter 5

A Three-dimensional Linear System Analysis Framework for the Optimization of Breast Tomosynthesis: Theory

Optimization of breast tomosynthesis geometry and reconstruction is crucial for the clinical translation of this exciting new imaging technique. In this chapter, we developed a 3-D cascaded linear system model for breast tomosynthesis to investigate the influence of detector performance, imaging geometry and image reconstruction algorithm on the reconstructed image quality. The characteristics of a prototype breast tomosynthesis system equipped with an a-Se flat-panel detector as described in Chapter 4 and FBP reconstruction were used as an example in the implementation of the linear system model.

5.1 Background

5.1.1 Flourier slice theorem

Fourier slice theorem, also know as Central Slice Theorem, states that the Fourier transform of the projection of an 2-D object f(x,y) at angle θ corresponds to a line (with a polar angle θ) in the 2-D Fourier space of the object F(u,v).[70] The projection at angle θ, p(t, θ) is the line integral at angle θ as shown in Figure 5.1 and is defined by:

$$p(t,\theta) = \int_{-\infty}^{+\infty}\int_{-\infty}^{+\infty} f(x,y)\delta(x\cos\theta + y\sin\theta - t)dxdy \qquad (5.1)$$

where (t,θ) is polar coordinates of (x,y) and p(t, θ) is known as the Radon Transform of f(x, y). The Fourier transform of p(t, θ) is given by:

$$S(w,\theta) = \int_{-\infty}^{+\infty} p(t,\theta) e^{-j2\pi wt} dt \tag{5.2}$$

where (w,θ) is polar coordinates of (u, v). $S(w, \theta)$ can be elaborated as:

$$\begin{aligned} S(w,\theta) &= \int_{-\infty}^{+\infty} [\int_{-\infty}^{+\infty}\int_{-\infty}^{+\infty} f(x,y)\delta(x\cos\theta + y\sin\theta - t)dxdy] e^{-j2\pi wt} dt \\ &= \int_{-\infty}^{+\infty}\int_{-\infty}^{+\infty} f(x,y) e^{-j2\pi w(x\cos\theta + y\sin\theta)} dxdy \\ &= \int_{-\infty}^{+\infty}\int_{-\infty}^{+\infty} f(x,y) e^{-j2\pi(xu+yv)} dxdy \\ &= F(u,v) \end{aligned} \tag{5.3}$$

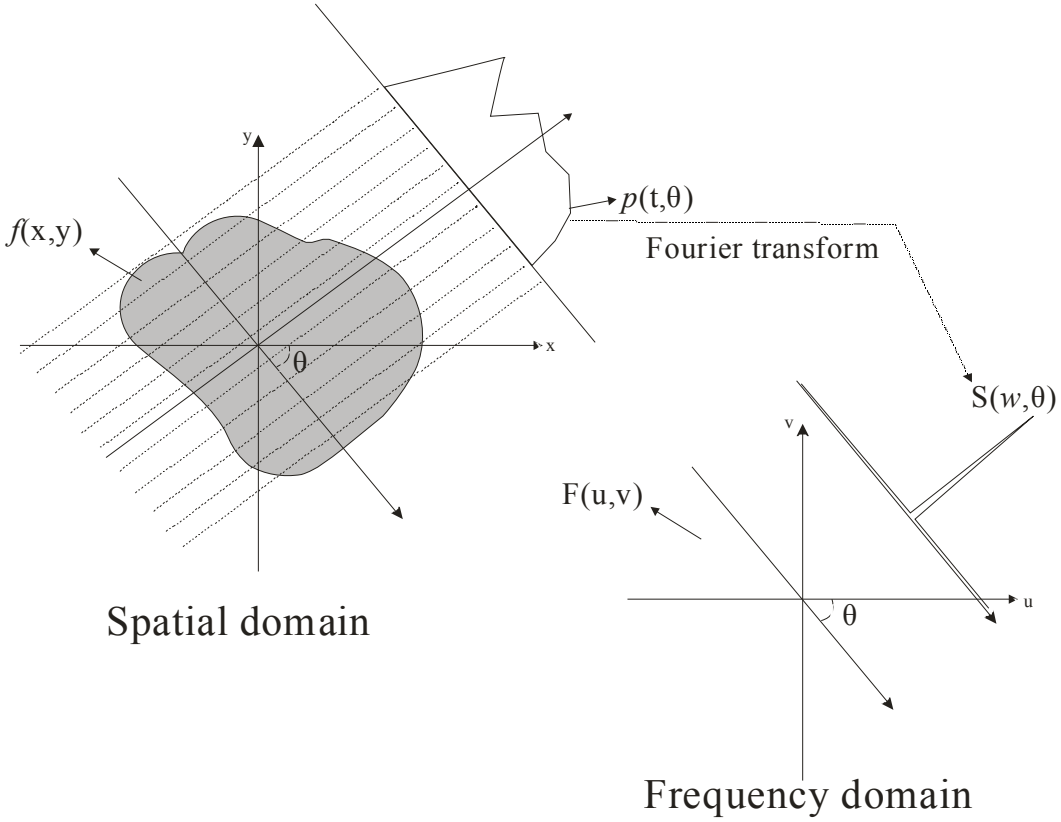

Figure 5.1, Diagram showing Fourier slice theorem

This states that for an object f(x,y), the 1-D Fourier transform $S(w, \theta)$ of a projection at angle θ is equivalent to the 2-D Fourier transform $F(u,v)$ of the object at a radial line with angle θ. In another word, the 2-D Fourier transform of an object function f(x,y) is

composed of 1-D Fourier transforms of each projection at oblique angles distributed in the space.

5.1.2 FBP reconstruction

The object function f (x, y) can be recovered by using the inverse Fourier transform of F(u,v). Mathematically f (x, y) is written as:

$$f(x,y) = \int_{-\infty}^{+\infty}\int_{-\infty}^{+\infty} F(u,v)e^{j2\pi(ux+vy)}dudv \tag{5.4}$$

Or more precisely:

$$f(x,y) = \int_{0}^{\pi} d\theta \int_{-\infty}^{+\infty} F(w\cos\theta, w\sin\theta)e^{j2\pi wt}|w|dw \tag{5.5}$$

Where F(w cos θ+ w sin θ) is the Fourier transform of projection at angle θ. The inside integral is the inverse Fourier transform of projection filter $|w|$ in the frequency domain, therefore it is called 'filtered projection'. From the above equation, the object f(x,y) at location (x,y), is reconstructed through a summation of all filtered projections that have passed through that point, at all angles within the angular range π. The filter with expression $|w|$ is called Ramp (RA) filter. In practice, filters other than RA are applied in order to best display features of interest.

5.2 Introduction

Tomosynthesis systems are usually modified from existing screening mammography systems by adding tube gantry motion. The operation and performance of digital mammography detectors were modified to accommodate the increased acquisition speed

and lower dose (per view) used in tomosynthesis. As a result, tomosynthesis image quality is compromised by many factors such as angular range, number of views, detector performance and reconstruction filters. Several investigations have been performed to study tomosynthesis image quality. Wu *et al* used the objects in an ACR phantom to study the effects of angular range and view number.[71] Ren *et al* investigated the dependence of in-plane resolution on inherent detector performance and FSB.[10] We built a computer simulation platform for breast tomosynthesis to investigate the effects of system geometry, detector performance and reconstruction algorithms.[57] The image quality was evaluated using CNR and in-plane MTF of reconstructed, simulated objects. Chen *et al* measured and compared the image noise and resolution using in-plane image slices for several reconstruction algorithms.[72] However, most studies used objects with mixed frequency components, and the evaluation was based on in-plane images only, i.e., 1-D or 2-D frequency domain.[10, 55, 73] It is difficult to fully reveal the effects of imaging geometry because breast tomosynthesis uses a limited angular range, and the reconstructed images are highly anisotropic. Hence it is important to develop fully 3-D analysis methods.

Our goal is to build a 3-D linear system analysis framework for breast tomosynthesis. Cascaded linear models have been used extensively to study the performance of digital detectors in the context of projection imaging.[20, 74] The theoretical foundation of NPS analysis in 3-D has been established for CT,[75, 76] and more recently for CBCT.[77, 78] With linear reconstruction algorithms, e.g. FBP, linear system analysis can be applied to tomosynthesis, and facilitate the understanding of the effects of system geometry, detector performance and reconstruction filters on the image quality of reconstructed

tomosynthesis slices. Compared with CBCT, tomosynthesis is performed with limited angular range (<50°) and number of views (typically < 30). Due to incomplete data sampling, the images are reconstructed using anisotropic voxel size, with in-plane (parallel to detector surface) pixel size d_x and d_y comparable to that of the projection images, and in-depth dimension d_z of 1 mm. Figure 5.2 shows the relationship between the reconstructed image space and the frequency domain in tomosynthesis. In tomosynthesis only the shaded area with an angular range of θ ($\pm\frac{\theta}{2}$) is sampled in the frequency domain.

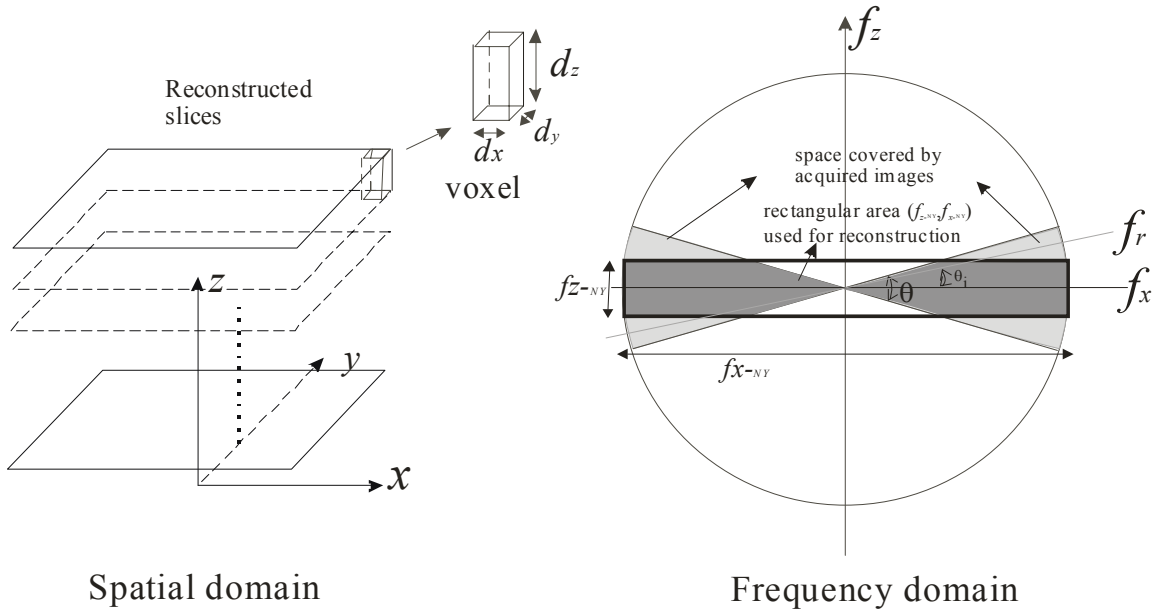

Figure 5.2 Diagrams showing the data sampling of the reconstructed images for tomosynthesis in the spatial domain (left) and spatial frequency domain (right). The area shaded in light grey with an angular range of θ ($\pm\frac{\theta}{2}$) shows the sampled frequency range as determined by the Fourier slice theorem. The area shaded in darker grey indicates the frequency range below the Nyquist frequencies in both the x (tube travel) and z (slice thickness) directions. As described later in the chapter, frequency limiting filters, such as the slice thickness filter, can be applied in the FBP process to minimize aliasing in the reconstruction process.

5.3 Component of 3-D linear model

Our model is based on a linear system approximation for breast tomosynthesis, i.e. stationary and shift-invariant. The linear system assumption for a-Se detector in the projection image domain has been described in detail previously.[20] In the context of tomosynthesis reconstruction, a parallel beam approximation and a FBP algorithm were used, similar to that used in linear system analysis of cone-beam CT. Since in tomosynthesis system the breast is compressed directly onto the surface of the detector, the magnification due to cone-beam projection is minimal, however the blur due to focal spot motion is significant.

Here we consider an example breast tomosynthesis geometry described in Chapter 4[79]. It is equipped with an a-Se detector with 85 μm pixel size. The x-ray tube travels continuously in an arc to acquire N projection images within an angular range θ. The nominal value for θ is 40^o ($\pm 20^o$), with maximum $N = 49$. To keep scan time within 20 seconds, $N \leq 25$ was usually used. A harder mammography energy spectrum with target/filter combination of W/ Rh with nominal Rh thickness of 50 μm was preferred over Mo spectrum to maximize the SNR ratio in tomosynthesis.[11] Since the detector performance and FSB depends on operational modes and dose in breast tomosynthesis acquisition, the parameters used in our model is based on the parameters listed in Table 5.1. A total exposure of 144 mAs at 28 kVp was assumed, which corresponds to an average glandular dose of 1.7 mGy for a 4 cm average breast. The average detector entrance exposure after attenuation by the breast is 1.18 mR per view with 25 views.

FBP reconstructions were used to reconstruct 1 mm thick image slices parallel to the stationary detector. The pixel size for each reconstructed in-plane image could be as

small as the detector pixel size, i.e. 85 μm. Therefore the reconstructed voxel is highly anisotropic, with dimension of 0.085 x 0.085 x 1 mm^3. As shown in Figure 5.2, the axes of the imaging system are defined as follows: The x-y- plane defines the reconstructed planes parallel to the detector, with the x-axis representing the tube travel direction. The z- axis is perpendicular to the detector plane. For the remainder of this chapter, the x-y-plane is referred to as the 'in-plane', and the x-z plane, which corresponds to the cross-sectional plane in CT, is referred to as the 'in-depth' plane. The frequency domain variables shown in Figure 5.2 are defined as follows: f_x and f_z are the Cartesian coordinates for the spatial frequencies in the x- and z- directions; f_r and θ_i are the polar coordinates, where f_r is the radial frequency and θ_i is the angle. According to Fourier Slice Theorem,[70] the projection image taken at angle θ_i fills the frequency space along the same angle, and the frequency response of the projection image corresponds to the radial frequency f_r along θ_i. The polar coordinates are related to the Cartesian coordinates of the reconstructed image through:

$$f_z = f_r \sin(\theta_i), f_x = f_r \cos(\theta_i), f_r = \sqrt{f_x^2 + f_z^2} \quad (5.6)$$

Table 5.1 Imaging parameters

Detector parameters	Pixel size (a): 85 um $f_{r\text{-}NY}$: 5.88 cycles/mm
x-ray spectrum	Target/filter: W/Rh 28 kVp
Imaging protocol	Angular range: $40^o(\pm 20^o)$ View number: 25 Scanning time: 20.8 s Total mAs: 144 mAs
Reconstruction	Algorithm: FBP voxel size(d_x, d_y, d_z): 0.085 x 0.085 x1 mm^3

5.3.1 Detector cascaded linear system model

The detector parameters for the a-Se FFDM detector described previously were used as an example in our model development.[19] The detector has a pixel size of 85 μm and a-Se layer thickness of 200 μm. Previously we have developed and validated a cascaded linear model for the detector.[20, 21, 23] The model can be used to predict the detector performance, in the form of MTF, NPS, and DQE as a function of detector parameters and x-ray exposures. The output of this model, which will be used as the input for further stages in tomosynthesis, consists of the signal spectrum Φ_p and noise spectrum S_p. They are related to the detector presampling MTF, and DQE through:

$$\Phi_p(f_r, f_y) = k\mathrm{MTF}_p(f_r, f_y)$$
$$\mathrm{DQE}(f_r, f_y) = \frac{\Phi_p{}^2(f_r, f_y)}{S_p(f_r, f_y) \times q_0} = \frac{[k\mathrm{MTF}_p(f_r, f_y)]^2}{S_p(f_r, f_y) \times q_0} \tag{5.7}$$

where q_0 is the number of incident x-ray quanta per projection view and k is the pixel response of the detector for a given exposure.

It was found previously that image correction could introduce additional noise to the images and result in a DQE that is lower than predicted by the model.[19] To represent the measured performance of a-Se flat-panel detector as that shown in Figure 5.3,[79] the detector parameters used in the model had to be modified. The following detector parameters in the model were varied until the measured and calculated MTF and DQE at different exposure levels matched: 1) the x-ray to charge conversion of a-Se, i.e., the energy W required to generate EHP; 2) the thickness of the top blocking layer for a-Se, which absorbs x-rays but does not contribute to signal due to the limited range of free carriers; 3) the electron noise n_e, usually given in number of electrons per pixel. The modeled results are shown in Figure 5.3, and they match reasonably well with the

measured MTF and DQE. The corresponding detector parameters are W = 50 eV, thickness of 22 μm for the top blocking layer, and electronic noise n_e = 2000 electrons/pixel. It is important to note that the modeled top blocking layer thickness is significantly larger than the real value used in the detector. It is artificially enlarged to account for the additional drop in DQE due to image correction and other factors that are not accounted for in the detector model.

Figure 5.3(b) shows that at 1.18 mR, which corresponds to the detector exposure per view (with 25 views) for an average 4 cm breast, DQE(0) is ~0.5. There is no significant degradation by electronic noise from the maximum values measured at higher exposures.

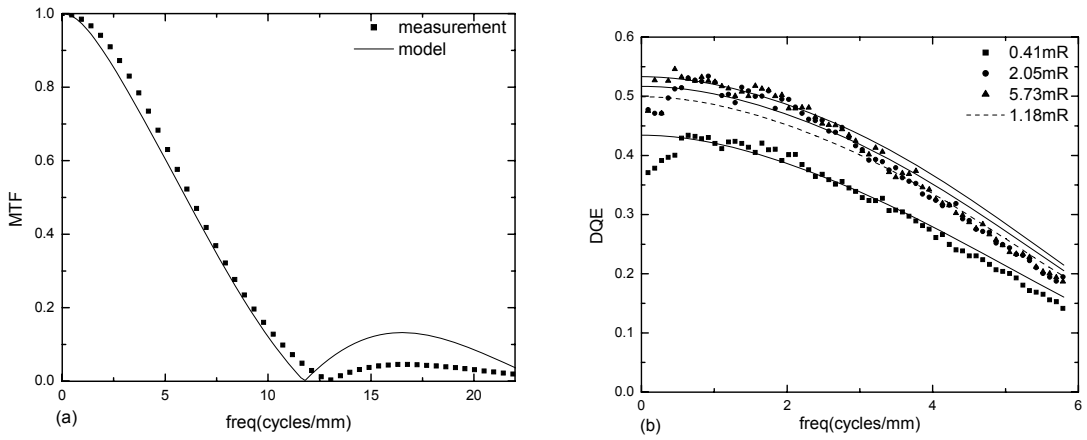

Figure 5.3 Experimental and model result for (a) MTF, (b) DQE for an a-Se digital detector with 85 μm pixel size.

5.3.2 3-D model development for tomosynthesis

Figure 5.4 shows the flow chart of the 3-D cascaded linear system model for tomosynthesis. The output spectra, Φ_p, and S_p, of the existing detector cascaded model are propagated through five more stages that are unique for tomosynthesis acquisition and reconstruction: 1) additional FSB due to focal spot motion, which is in the tube travel direction only; 2) logarithmic transformation on projection images; 3) reconstruction

filters applied to the resulting projection images; 4) conversion and mapping of the 2-D spectra along the projection angle within the limited angular range; and 5) 3-D sampling according to the anisotropic voxel size, which introduces noise aliasing above the Nyquist frequencies in each direction. The output spectra for each stage are denoted by the subscripts of the signal spectrum Φ and noise power spectrum *S*, as defined in Figure 5.4. Now we will describe separately the propagation of signal and noise spectra through each of the five stages.

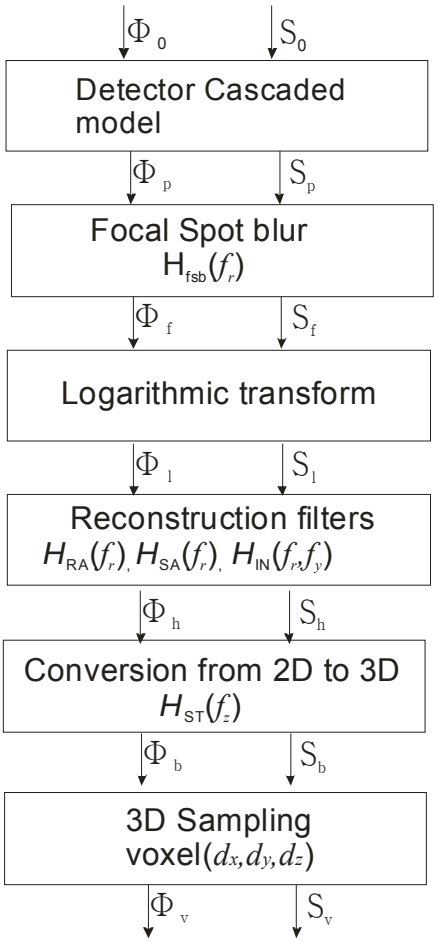

Figure 5.4 Flow chart for signal and noise propagation in the model

1. Focal spot blur

In the cascaded linear system model, the FSB is usually implemented as a stage after the x-ray absorption and before the x-ray to charge conversion gain. In projection mammography, due to the small focal spot and minimal magnification, FSB is usually negligible. To separate the effects of intrinsic detector parameters and extrinsic factors such as focal spot motion in tomosynthesis, in the present model the additional FSB caused by tube motion was implemented after the intrinsic detector model. Because FSB introduces a multiplicative factor to the MTF and does not affect the NPS, [20] the results should be equivalent to the original linear system approach. Since this additional FSB is only in the tube travel direction, i.e. along θ_i direction of each projection image. The output signal and noise power spectra after FSB, which has a blur function of $H_{\text{fsb}}(f)$, is given by:

$$\begin{aligned} \Phi_f(f_r, f_y) &= \Phi_p(f_r, f_y) H_{\text{fsb}}(f_r) \\ S_f(f_r, f_y) &= S_p(f_r, f_y) \end{aligned} \tag{5.8}$$

FSB due to continuous tube motion during tomosynthesis acquisition could be significant.[10, 13] [80] $H_{\text{fsb}}(f)$ is given by the product of two aperture functions: 1) the finite focal spot size a_0; and 2) focal spot travel distance a_1 during the x-ray exposure of each view. Since $a_1 >> a_0$, $H_{\text{fsb}}(f)$ is simplified to a single aperture function and applied to f_r along each θ_i direction:

$$H_{\text{fsb}}(f_r) = \text{sinc}(a_1 f_r) \tag{5.9}$$

Although the implementation of our breast tomosynthesis linear system model assumes isocentric tomographic geometry for filter application and backprojection, $H_{\text{fsb}}(f)$ for a stationary detector breast tomosynthesis system is more severe.[80] As a compromise, the FSB for the prototype breast tomosynthesis system with stationary detector in Chapter 4

is adopted for $H_{fsb}(f)$ in our model. Due to the variation in magnification as a function of distance from the detector, $H_{fsb}(f)$ is position dependent. For simplicity, $H_{fsb}(f)$ was calculated for tube angle $\theta = 0$ and $d = 4$ cm above the detector surface. The focal spot travel distance during each view in the tomosynthesis acquisition for x-ray parameters listed in Table 5.1 is 0.8 mm, resulting in $a_1 = 0.075$ mm if the detector is stationary during x-ray exposure.

Plotted in Figure 5.5 is the calculated $H_{fsb}(f)$ in comparison with the detector presampling MTF and the total MTF. It shows that the intrinsic detector MTF dominates the total MTF, and FSB causes an additional drop of 30% at the Nyquist frequency in the r- direction, $f_{r\text{-NY}}$ (5.88 cycles/mm). Consequently this will cause a decrease in 3-D MTF and DQE for the reconstructed images as will be shown in Sec. 5.5 and 5.6. The total MTF with FSB shown in Figure 5.5 was used in the 3-D model for projection MTF in all directions.

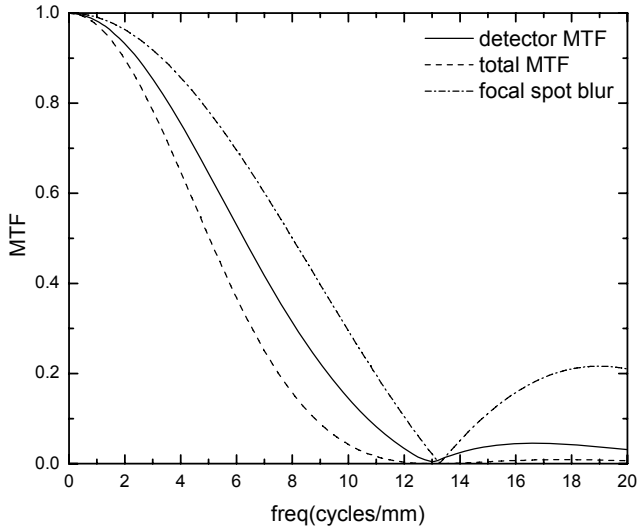

Figure 5.5 The effect of FSB on presampling MTF of projection images. Acquisition parameters are shown in Table 5.1. The FSB was calculated for a breast tomosynthesis system with a stationary detector.

2. Logarithmic transformation

A logarithmic transformation is performed on each projection image to yield the line integral of x-ray attenuation prior to FBP reconstruction. Although this transformation is not a linear process, it can be considered linear within a small range of exposure. This is applicable for low-contrast objects. As shown in Appendix A, the output signal and noise power spectra are propagated through a gain stage, and can be written as:

$$\Phi_l(f_r, f_y) = \frac{\Phi_f(f_r, f_y)}{k}$$
$$S_l(f_r, f_y) = \frac{S_f(f_r, f_y)}{k^2} \tag{5.10}$$

where k is the sensitivity of the detector at a given exposure. Neither MTF nor DQE change from the prior stage in this process.

3. Filters

During image reconstruction several filters are applied, which modify the signal and noise spectra of the projection images as deterministic blur. These filters include: 1) RA filter H_{RA}, applied in the scan (r-) direction of the projection image only; 2) Spectrum apodization (SA) filter H_{SA}, applied in the scan (r-) direction only; and 3) slice thickness (ST) filter H_{ST}, applied in the z-direction, and 4) interpolation (IN) filter H_{IN}, applied in both r- and y- directions. It is important to note that in a tomosynthesis geometry where the detector stays stationary while the tube moves in an arc, the filtered projection image at each angle θ_i does not correspond to the same f_r response, but differs by the inverse of $\cos(\theta_i)$. However this factor was ignored in our model to facilitate the comparison

between tomosynthesis and CT. As shown by Wu et. al., this factor is negligible with an angular range of ±20°.[71]

The RA filter is given by:[14]

$$H_{\mathrm{RA}}(f_r) = 2 \times \tan(\theta) \times \frac{|f_r|}{f_{r\text{-NY}}} \quad \text{for } |f_r| \le f_{r\text{-NY}} \tag{5.11}$$

where θ is the angular range of the tomosynthesis acquisition. For $|f_r| > f_{r\text{-NY}}$, the RA filter replicates at multiples of $2f_{r\text{-NY}}$. Shown in Figure 5.6 is the RA filter used in the present investigation. Since the amplitude of the filter is dependent on θ, the magnitude of NPS is scaled by $\tan^2(\theta)$.

The purpose of both the SA and ST filters is to limit the bandwidth of the projection data and reduce noise and aliasing. In our implementation, both the SA and ST filters use a Hanning window function given by $H(f) = 0.5[1 + \cos(\pi f / W_f)]$, where W_f defines the width of the Hanning window, i.e. the lowest spatial frequency at which the value of $H(f)$ decreases to zero. W_f is given in multiples of f_{NY} of the projection images, and the multiplicative factors for the SA and ST filters are denoted A and B, respectively. The SA filter is applied in the tube travel direction of the image, i.e. along the r-axis for each θ_i, and the 1-D Hanning window function is given as:

$$H_{\mathrm{SA}}(f_r) = \begin{cases} 0.5\,[1 + \cos(\dfrac{\pi f_r}{A f_{r\text{-NY}}})] & \text{for } |f_r| \le A f_{r\text{-NY}} \ (A<1) \cup |f_r| \le f_{r\text{-NY}} \ (A>1) \\ 0 & \text{for } A f_{r\text{-NY}} < |f_r| \le f_{r\text{-NY}} \end{cases} \tag{5.12}$$

For $|f_r| > f_{\text{r-NY}}$, the SA filter replicates at multiples of $2f_{r\text{-NY}}$ and the maximum amplitude is unity. In the present study, A = 1.5 was selected, which results in $H_{\mathrm{SA}}(f_{r\text{-NY}}) = 0.25$.

The ST filter is applied in the z- direction only and will be incorporated in Stage 4 when the 2-D information is transferred to 3-D. The ST filter (H_{ST}) with relative window width B is given by a Hanning window function:

$$H_{ST}(f_z)=\begin{cases}0.5[1+\cos(\dfrac{\pi f_z}{Bf_{r-NY}})] & \text{for } |f_z| \le Bf_{r\text{-}NY} \text{ and } |f_z| \le \tan(\theta) f_{r\text{-}NY} \\ 0 & \text{elsewhere}\end{cases} \tag{5.13}$$

where $f_z = f_r \sin(\theta_i)$. The ST filter presents a 1-D function of f_z. A detailed discussion of the ST filter was provided in Refs.[14, 57] During reconstruction the ST filter is implemented on each projection image (with angle θ_i) individually by multiplication in the frequency domain. The difference of the ST from the SA filter is that the modulation to the projection is both frequency and angle dependent.

Because voxel driven backprojection was used in the reconstruction, a bilinear interpolation filter, H_{IN}, was applied in both r- and y- directions. The filter function, $H_{IN}(f_r, f_y)$, associated with bilinear interpolation is a sinc^2 function, is related to the pixel size in the r- and y- directions through:

$$H_{IN}(f_r, f_y) = \text{sinc}(af_r)^2 \text{sinc}(af_y)^2 \tag{5.14}$$

where a is the square pixel size (85 μm) of the projection image(shown in Table 5.1).

To investigate the effect of filter functions, four different filter schemes, as summarized in Table 5.2, were incorporated in the model: 1) simple backprojection (SBP) reconstruction without any filters; 2) Ramp filter H_{RA} only; 3) Ramp H_{RA} and SA H_{SA} (A=1.5) filter, 4) Ramp H_{RA} with SA H_{SA} (A=1.5) and ST H_{ST} (B = 0.1) filter. H_{IN} was applied in all schemes because voxel driven backprojection was used throughout the reconstruction. The discussion for the selection of B value will be provided in Stage 5 with aliasing.

Table 5.2 Summary of the four filter schemes for reconstruction.

Filter scheme 1	Simple backprojection (SBP) reconstruction
Filter scheme 2	Ramp H_{RA} only
Filter scheme 3	H_{RA} x H_{SA} (A=1.5)
Filter scheme 4	H_{RA} x H_{SA}(A=1.5) x H_{ST}(B = 0.1)

The frequency response curves of different filters are shown in Figure 5.6. The RA filter, which increases linearly with frequency, reduces low frequency response of the projection images. Both the SA and IN filters reduce the high frequency response, resulting in a combined response of 0.1 at $f_{r\text{-NY}}$. However in y-direction, the IN filter is the only means to reduce high frequency response.

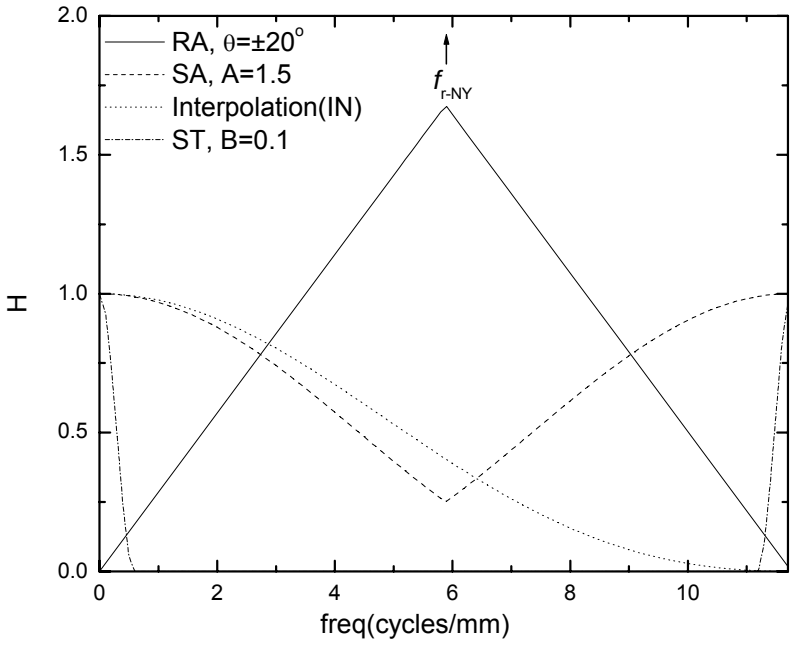

Figure 5.6 Reconstruction filters plotted as a function of frequency with full detector resolution, which corresponds to f_{NY} = 5.88 cycles/mm. The angular range is ±20°, and the filter parameters are listed in Table 5.2.

After propagation through all the filter functions, the signal and noise power spectra became:

$$\Phi_h(f_r,f_y)=\Phi_l(f_r,f_y)\times H_{\mathrm{RA}}(f_r)\times H_{\mathrm{SA}}(f_r)\times H_{\mathrm{IN}}(f_r,f_y)$$
$$S_h(f_r,f_y)=S_l(f_r,f_y)\times H_{\mathrm{RA}}{}^2(f_r)\times H_{\mathrm{SA}}{}^2(f_r)\times H_{\mathrm{IN}}{}^2(f_r,f_y) \quad (5.15)$$

4. Conversion from 2-D to 3-D

The filtered signal and noise power spectra for each projection image at angular position θ_i are mapped into the 3-D space using the Fourier slice theorem, similar to the method used for CT[75]. The difference is that in CT, backprojection extends 1-D spectra to 2-D[75, 76, 81]. Whereas in tomosynthesis, just like in CBCT[78]. the spectra are extended from 2-D to 3-D. For tomosynthesis acquisition with angular range θ and view number *N*, the output 3-D signal spectrum Φ_b, signal power spectrum Ψ_b and noise power spectrum S_b can be calculated using:[75]

$$\Phi_b(f_r,f_z)=\Phi_h(f_r,f_y)\sum_{i=1}^{N}\delta(f_x\sin(\theta_i)-f_z\cos(\theta_i))\times H_{\mathrm{ST}}(f_z)$$
$$\Psi_b(f_r,f_z)=\Psi_h(f_r,f_y)\sum_{i=1}^{N}\delta(f_x\sin(\theta_i)-f_z\cos(\theta_i))\times H_{\mathrm{ST}}{}^2(f_z) \quad (5.16)$$
$$S_b(f_r,f_z)=S_h(f_r,f_y)\sum_{i=1}^{N}\delta(f_x\sin(\theta_i)-f_z\cos(\theta_i))\times H_{\mathrm{ST}}{}^2(f_z)$$

where $\delta(f_x\sin(\theta_i)-f_z\cos(\theta_i))$ is incorporated to map the spectra of each projection image along angle θ_i in the 3-D frequency domain. It represents the "spoke" along θ_i in polar coordinates(Figure 5.2). The signal power spectrum Ψ_b is listed as a separate parameter to facilitate the calculation of DQE. It is given by Φ_h^2, and is similar to the variable defined as "deterministic NPS" in the work of Siewerdsen et al.[78] When converting the 3-D spectra in Eq. 5.16 from polar coordinates to Cartesian coordinates, the values should be normalized by the "spoke density", which follows $1/f_r$. This aspect has been explained in detail for the derivation of CT NPS.[76, 82]

In CT and CBCT, more than 300 views are usually acquired with a full angular range of 180 degrees, resulting in an angular sampling interval of $\frac{\theta}{N} < 1^o$ with $\theta = 180^o$. The propagation of presampling signal and noise power spectra are given by:[76, 78]

$$\begin{aligned}
\Phi_b(f_r, f_z) &= \frac{N}{\theta f_r} \times \frac{1}{N} \times \Phi_h(f_r, f_y) \\
\Psi_b(f_r, f_z) &= \frac{N}{\theta f_r} \times (\frac{1}{N})^2 \times \Psi_h(f_r, f_y) \\
S_b(f_r, f_z) &= \frac{N}{\theta f_r} \times (\frac{1}{N})^2 \times S_h(f_r, f_y)
\end{aligned} \tag{5.17}$$

where $\frac{N}{\theta f_r}$ is the spoke density. Since in CT the result of reconstruction is normalized by the view number N to obtain the linear attenuation coefficients, the signal and noise power spectra are normalized accordingly.

The normalization factors for tomosynthesis were determined based on Eq. 5.17 as:

$$\begin{aligned}
\Phi_b(f_r, f_z) &= \frac{N}{\theta f_r} \times \Phi_h(f_r, f_y) \times H_{\mathrm{ST}}(f_z) \\
\Psi_b(f_r, f_z) &= \frac{N}{\theta f_r} \times \Psi_h(f_r, f_y) \times H_{\mathrm{ST}}{}^2(f_z) \\
S_b(f_r, f_z) &= \frac{N}{\theta f_r} \times S_h(f_r, f_y) \times H_{\mathrm{ST}}{}^2(f_z)
\end{aligned} \tag{5.18}$$

The image value for each voxel in our FBP reconstruction was not normalized by the view number N since tomosynthesis does not provide accurate reconstruction of the linear attenuation coefficients of materials due to the limited angle. Compared with CT and CBCT, the angular sampling interval is usually larger in tomosynthesis, ranging from 1^o~3^o, e.g. 1.8^o for 25 views with $\theta = \pm 20^o$. In the present investigation, our model predicts the average system performance assuming sufficiently small angular sampling interval. We found this assumption to be reasonable for angular separation of $< 2^o$

between views. In the limit of large angular separation, streaks will appear in the NPS (x-z plane). This factor is ignored in our model, which generates smooth curves.

5. 3-D sampling

The 3-D sampling associated with finite voxel spacing in the backprojection process is the final stage of our cascaded linear system model. The 3-D NPS is replicated at multiples of $2f_{\text{NY}}$ in each direction. Noise aliasing is introduced in this stage and the output aliased NPS, S_{v}, is given by:

$$S_v(f_x, f_y, f_z) = \sum_{i,j,k} S_b(f_x, f_y, f_z)\delta(f_x - \frac{i}{d_x}, f_y - \frac{j}{d_y}, f_z - \frac{k}{d_z}) \quad (I, j, k \text{ as integer}) \qquad (5.19)$$

The Nyquist frequencies in each direction is determined by the voxel dimension $d_{\text{x}} = d_{\text{y}} =$ 0.085 mm, and $d_{\text{z}} = 1$ mm.

With the large voxel dimension in z-direction, aliasing would be significant without the application of ST filter, as shown in Figure 5.7(a). The information beyond $f_{z\text{-NY}}$ replicates at $2f_{z\text{-NY}}$ and folds back to below $f_{z\text{-NY}}$, which causes aliasing in z-direction (in darker grey). The ST filter, which limits frequency components beyond $f_{z\text{-NY}}$, prevents noise aliasing (Figure 5.7b-c). B = 0.085 corresponds to a ST filter Hanning window width of $f_{z\text{-NY}} = 0.5$ cycles/mm and completely eliminates noise aliasing. By varying B value or choosing different filter functions, an optimal compromise can be achieved between the detection of small objects (high frequency) and the reduction of noise aliasing. For the present chapter, B = 0.1 was selected because the Hanning window decreases abruptly when approaching the window width. The slightly larger B value helps preserve high frequency information without significant increase in noise aliasing. The response of the ST filter is 10% at $f_{z\text{-NY}}$.

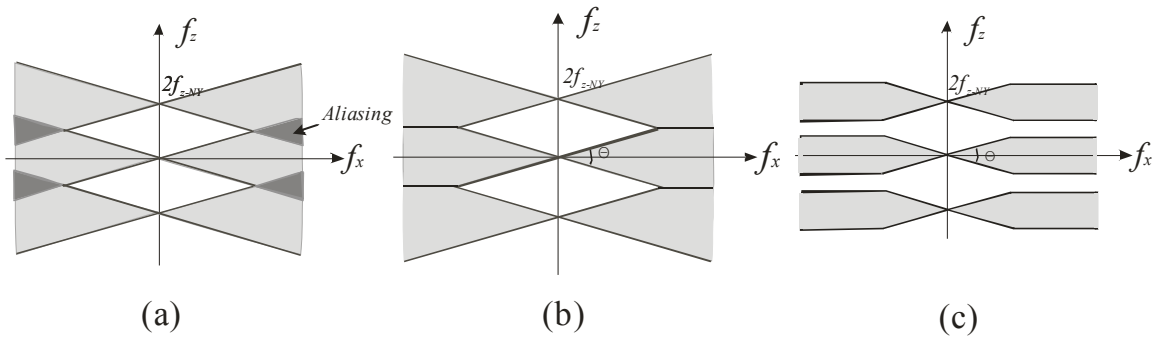

Figure 5.7 Schematic diagrams showing aliased NPS after backprojection: (a) without ST filter; (b) with ST filter (B = 0.085); and (c) with ST filter (B < 0.085). The frequency space in white is not sampled by tomosynthesis, the area shaded in light grey is the sampled frequency space, and the area shaded in darker grey has aliased NPS.

The final 3-D NPS, MTF and DQE can be obtained from the signal and noise power spectra propagated through the cascaded stages. Due to the coarse z-direction sampling, the reconstructed tomosynthesis volume are usually viewed as a sequence of in-plane images parallel to the detector by the radiologists or computer-aided detection (CAD) algorithms[83]. Image quality metrics for in-plane images, including MTF and NPS were also derived from the 3-D parameters.

5.4 NPS

The final 3-D aliased NPS was obtained directly from the output of the cascaded process (S_v in Eq. 5.19). The in-plane (i.e. x-y plane) NPS, $S_{\text{in-plane}}$, was calculated by integrating S_v along z-axis:

$$S_{\text{in-plane}}(f_x, f_y) = \int_{\pm f_{z-\text{NY}}} S_v(f_x, f_y, f_z) df_z \tag{5.20}$$

5.4.1 3-D NPS

From the above theory of linear system analysis, 3-D NPS in tomosynthesis is affected by the following factors: 1) the aliased NPS of projection images, which has

been included in the detector model; 2) reconstruction filters H(f); 3) angular sampling of tomosynthesis acquisition; 4) 3-D sampling and noise aliasing in the backprojection process. In this section, the effects of the last three factors will be discussed.

Figure 5.8 shows the 3-D NPS before and after noise aliasing, S_b and S_v respectively, for filter scheme 3. The results are plotted up to f_{NY} in each direction ($f_{x\text{-}NY} = f_{y\text{-}NY} = 5.88$ cycles/mm, $f_{z\text{-}NY} = 0.5$ cycles/mm). The gray scale of the NPS images was chosen to display the maximum contrast. The shape of the NPS in the y-direction is due to the interpolation filter only. The aliasing of the NPS at high frequencies is clearly visible in S_v. To facilitate comparison, the aliased in-depth NPS (S_v) are replotted in Figure 5.9.

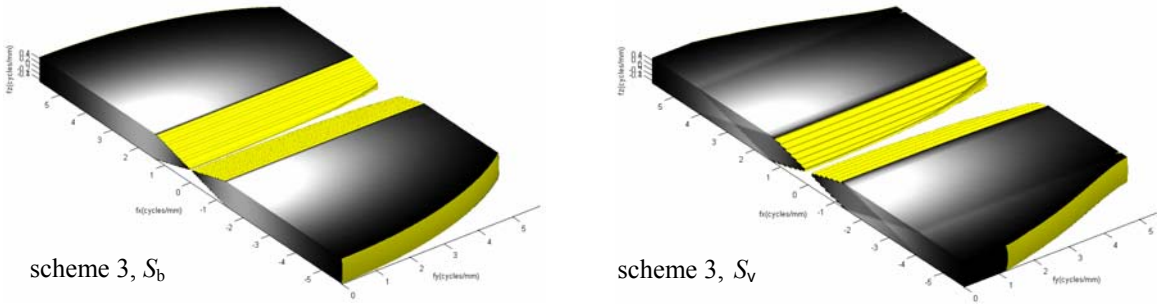

scheme 3, S_b scheme 3, S_v

Figure 5.8 3-D NPS before(S_b) and after(S_v) aliasing reconstructed with scheme 3. The NPS is plotted up to f_{NY} in each direction ($f_{x\text{-}NY} = f_{y\text{-}NY} = \pm 5.88$ cycles/mm and $f_{z\text{-}NY} = \pm 0.5$ cycles/mm). Half of the y- axis is plotted. Lighter shade indicates higher noise intensity.

Figure 5.9(a) shows the aliased in-depth NPS, i.e., the 2-D slice of the 3-D S_v at $f_y = 0$, for all four filter schemes. The NPS are plotted up to f_{NY} in each direction. Due to the limited angular range ($\pm 20^o$), only a fraction of the Fourier space is filled and the remainder is not sampled, seen as the black triangles in the center. Due to 3-D sampling, the NPS is replicated at multiples of $2f_{z\text{-}NY}$ (1 cycles/mm) and $2f_{x\text{-}NY}$, which introduces noise aliasing. The result for scheme 1 (SBP) shows that the NPS is the highest at zero frequency, which is caused by lack of RA filter. Since the high frequency component is

not effectively reduced by the IN filter, aliasing is introduced from the f_z components higher than $f_{z\text{-NY}}$. With the RA filter, as shown for filter schemes 2 and 3 in Figure 5.9(a), the NPS is zero at zero frequency and increases with frequency. Consequently noise aliasing at high frequencies also becomes more significant. With the application of the ST filter in scheme 4, noise aliasing is practically eliminated.

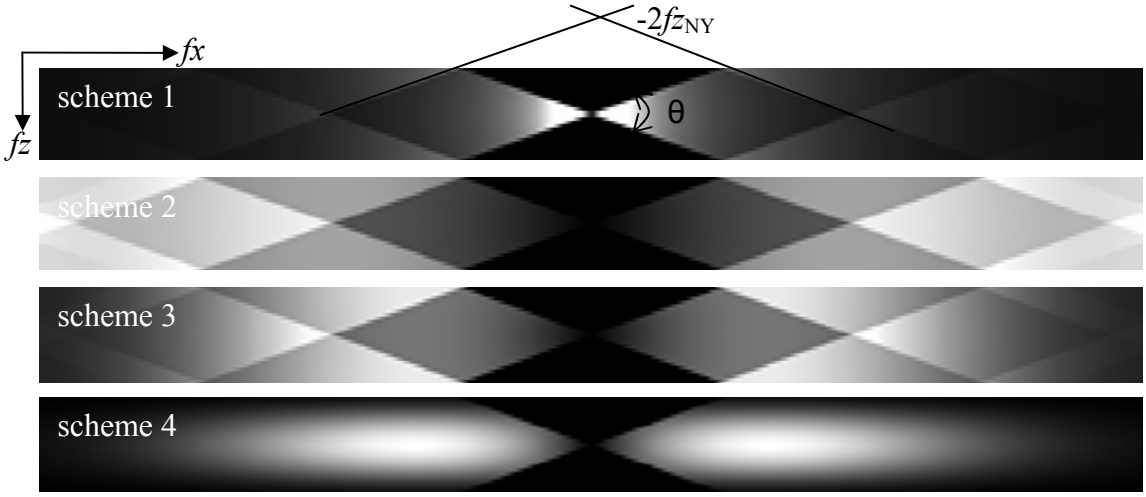

(a)

Figure 5.9 a)in-depth NPS (at $f_y = 0$) for scheme 1-4 with angular range of ±20°. The NPS is plotted up to f_{NY} in each direction ($f_{x\text{-NY}} = \pm 5.88$ cycles/mm and $f_{z\text{-NY}} = \pm 0.5$ cycles/mm).

To facilitate quantitative comparison between different filter schemes, the in-depth NPS at $f_z = 0$ is plotted in Figure 5.9(b) for all four schemes. It shows that for scheme 1, the NPS drops rapidly as frequency increases because of the normalization by spoke density (Eq. 5.18). For schemes 2-4, NPS near zero frequency is proportional to f as a result of the RA filter and the normalization by spoke density. The increase in NPS at high frequencies for schemes 1-3 is due to noise aliasing. Since the NPS replicates at multiples of $f_{z\text{-NY}}$, the adjacent NPS intersects with the x-axis at multiples of $2f_{z\text{-NY}}/\tan(\theta/2)$, i.e. 2.75 and 5.5 cycles/mm. As a result, an abrupt increase in NPS occurs at these frequencies. The NPS for scheme 4 has the lowest magnitude with no aliasing due to the additional ST filter.

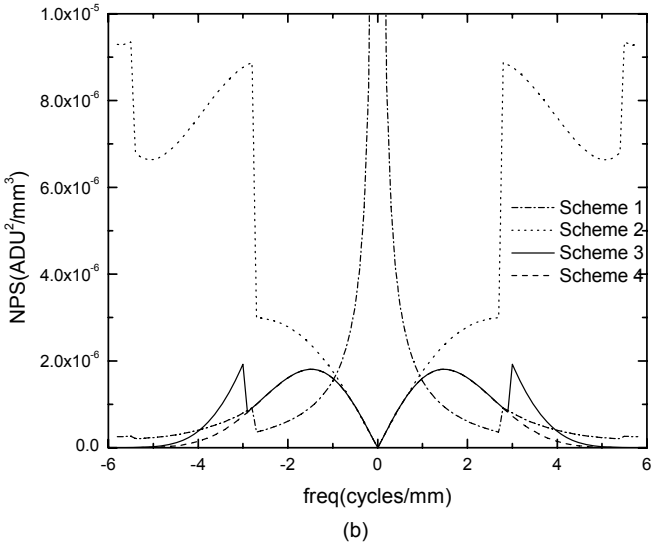

Figure 5.9 b)in-depth NPS at $f_z = 0$ for scheme 1-4. Angular range = ±20°

NPS also depends on the angular range of tomosynthesis acquisition and the reconstructed voxel size. Shown in Figure 5.10 is the NPS calculated for three different angular ranges: 20° (±10 °), 40 °(±20 °), 180 °(±90 °), all reconstructed into anisotropic voxel size (0.085 x 0.085 x 1 mm^3) with scheme 3. With the increase in angular range, the frequency space for NPS is better sampled, especially at low frequencies. However since the wider angular range introduces more frequency components into the region above f_z-$_{NY}$, aliasing in NPS is more severe.

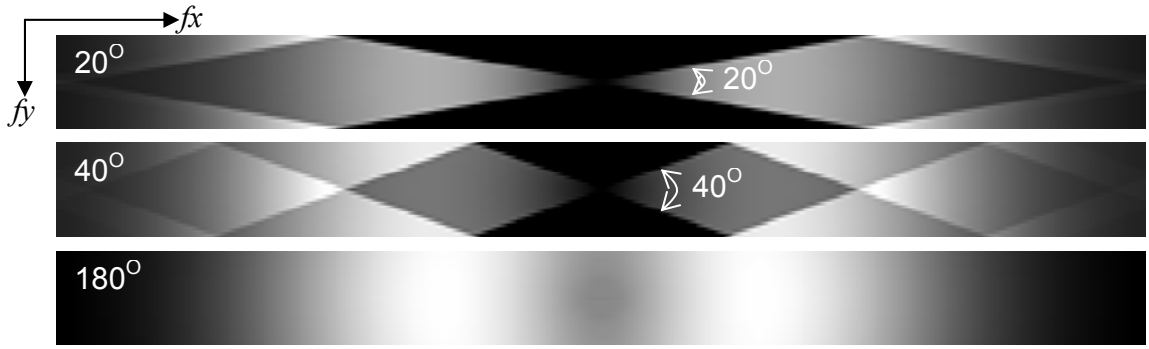

Figure 5.10 The in-depth NPS for three angular ranges (20°, 40°, 180°) with filter scheme 3 and anisotropic voxel size (0.085x0.085x1mm^3). The NPS is plotted up to f_{NY} in each direction ($f_{x\text{-}NY}$ = ±5.88 cycles/mm and $f_{z\text{-}NY}$ = ±0.5 cycles/mm).

To illustrate the effect of 3-D sampling on aliasing, Figure 5.11 shows the in-depth NPS with isotropic voxel size (0.085 x 0.085 x 0.085 mm^3). The small voxel dimension in z-direction essentially eliminates aliasing for all angular ranges. The complete sampling of frequency space (180 ^{o}) corresponds to CT, and the drop in NPS at low frequencies is due to RA filter[75].

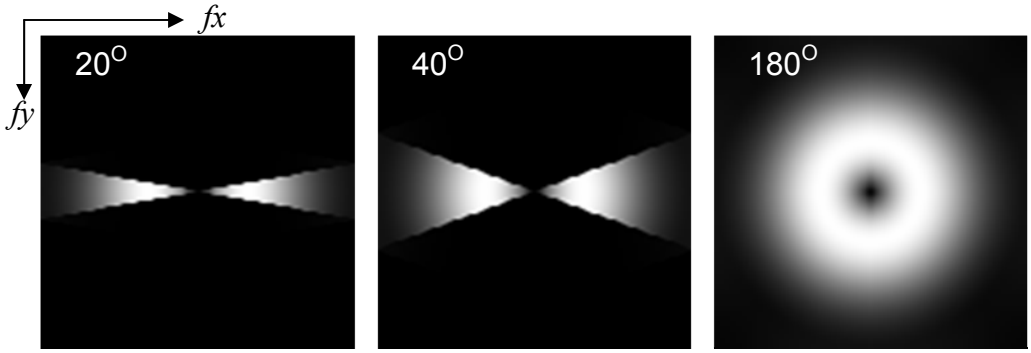

Figure 5.11 In-depth NPS for the different angular ranges (20^o, 40^o, 180^o), reconstructed with scheme 3 and isotropic voxel size (0.085 x 0.085 x 0.085 mm^3). The NPS is plotted up to f_{NY} in each direction ($f_{x\text{-}NY}$ = ±5.88 cycles/mm and $f_{z\text{-}NY}$ = ±5.88 cycles/mm).

5.4.2 In-plane NPS

Figure 5.12(a) shows the in-plane NPS images for all four filter schemes obtained using Eq. 5.20, and the corresponding 1-D plots at $f_y = 0$ are shown in Figure 5.12(b). The NPS of scheme 1 is isotropic, and the drop of NPS with f, as shown in Figure 5.12(b), is not as rapid as seen in the in-depth NPS, This is because the in-plane NPS is equal to the integration of the 3-D NPS along z-direction, which cancels out the effect of spoke density and leaves the IN filter the only factor affecting the NPS. For schemes 2-4 with the RA filter, the in-plane NPS at low frequencies is essentially proportional to f^2. This is because the f dependent 3-D NPS is integrated in the z-direction over a triangular shaped region of data sampled in tomosynthesis. It is interesting to point out that the noise

aliasing pattern seen in the 3-D NPS for filter schemes 1-3 is not observed in Figure 5.12(a) and (b). This is because the integration of aliased NPS along z-direction within $f_{z\text{-}NY}$ is equivalent to that the integration of presampling NPS over all f_z.

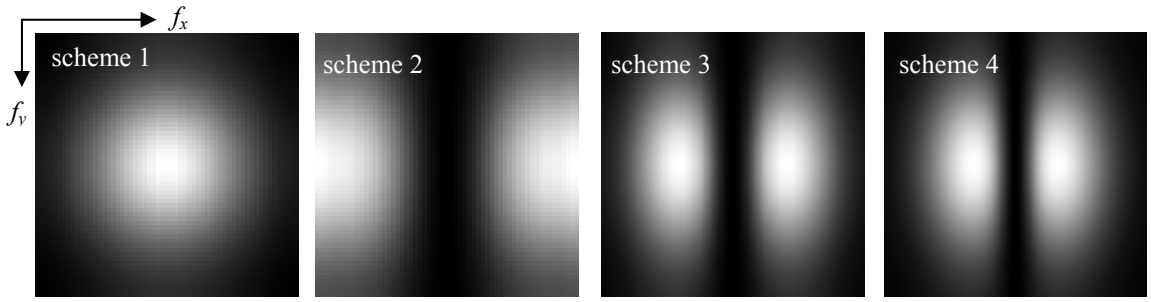

a)

Figure 5.12 a) In-plane NPS for scheme 1-4 with angular range of ±20°. The NPS is plotted up to f_{NY} in each direction ($f_{x\text{-}NY} = f_{y\text{-}NY} = \pm 5.88$ cycles/mm).

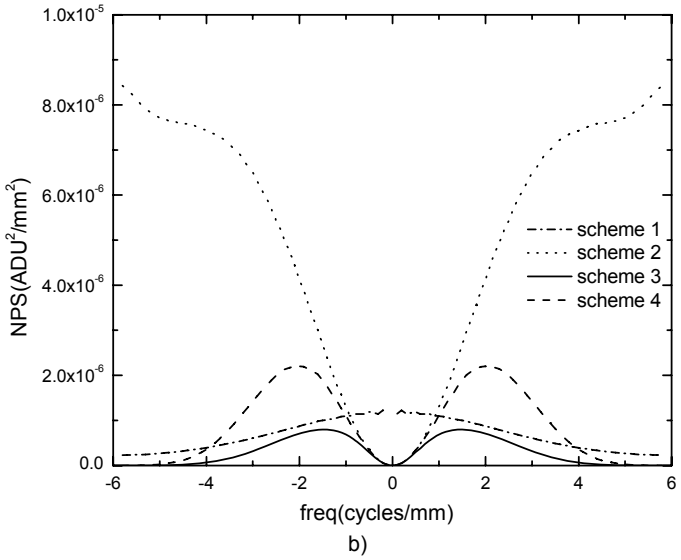

b)

Figure 5.12 b) In-plane NPS at $f_y = 0$ for scheme 1-4. Angular range = ±20°.

5.5 MTF

The presampling 3-D MTF (T_b) was obtained by normalizing the output signal spectrum:

$$T_b(f_x, f_y, f_z) = \Phi_b(f_x, f_y, f_z) / \Phi_b(0,0,0) \tag{5.21}$$

In previous studies, the resolution was usually investigated by placing a thin edge or slit phantom in a particular plane, and deriving the 1-D MTF from the in-plane image.[57, 84, 85] In a 3-D perspective, these phantoms have infinitesimal dimension in z-direction. To predict the in-plane MTF measured using this method, the 3-D MTF will have to be aliased and then integrated in z-direction as:

$$T_v(f_x, f_y, f_z) = \sum_k T_b(f_x, f_y, f_z)\delta(f_z - \frac{k}{d_z}) \quad (k \text{ is integer}) \tag{5.22}$$
$$T_{in-plane}(f_x, f_y) = \int_{\pm f_{z\text{-NY}}} T_v(f_x, f_y, f_z) df_z$$

where T_v is the aliased MTF. This method of in-plane MTF calculation assumes that the phantom is placed at the center of the slice, and it provides the maximum MTF achievable for in-plane MTF measurement.[86, 87]

5.5.1 3-D MTF

The major factors affecting the presampling 3-D MTF are: 1) projection MTF of the detector; 2) focal spot blur; 3) reconstruction filters H(*f*); and 4) angular range of tomosynthesis acquisition. The results in this section will address the effects of factors 2-4 because they are unique to tomosynthesis.

Shown in Figure 5.13 are the 3-D presampling MTF plotted up to $2f_{NY}$ in each direction for scheme 3. The 3-D MTF is for a limited angular range of $\pm 20^o$. Unlike the 3-D NPS (Figure 5.8), which is proportional to *f* at low frequencies, the 3-D MTF at zero spatial frequency is unity for the sampled frequency space because as shown in Eq. 5.17, the *f* dependence of the RA filter and the spoke density normalization factor cancel out.

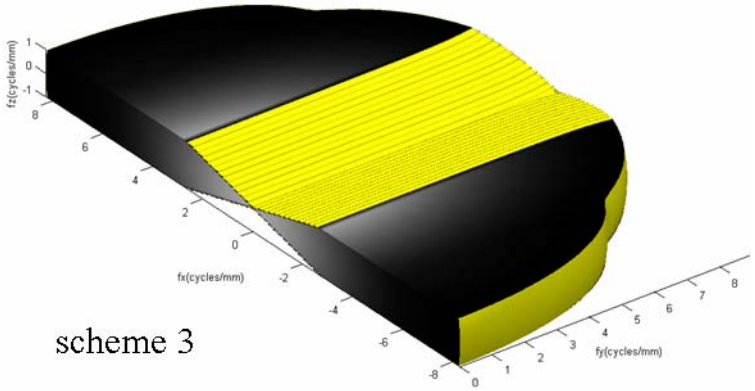

Figure 5.13 3-D presampling MTF with scheme 3, The MTF is plotted up to $2f_{NY}$ in each direction ($2f_{x\text{-}NY}$ = ±11.8 cycles/mm, $2f_{z\text{-}NY}$ = ±1 cycles/mm). Half of the y- axis is plotted. Lighter shade indicates higher value.

To facilitate the comparison of different filter schemes, the in-depth MTF (with f_y= 0) for all schemes are plotted in Figure 5.14(a). The MTF only has values within the angular

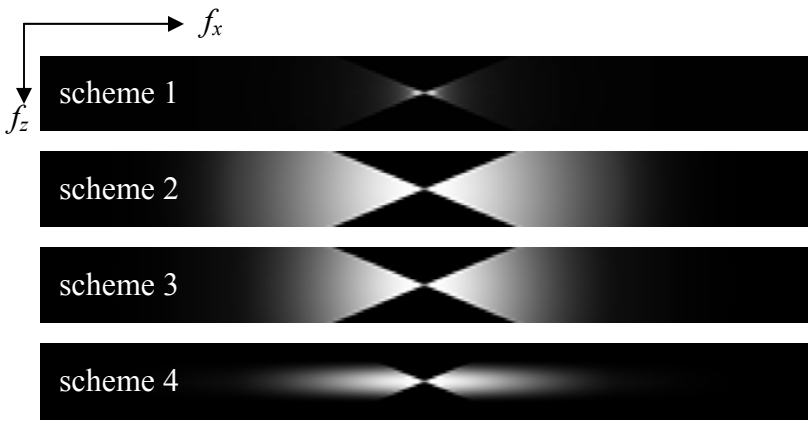

(a)

Figure 5.14 a) in-depth MTF for the four filter schemes. Angular range = ±20°. The MTF is plotted up to $2f_{NY}$ in each direction ($2f_{x\text{-}NY}$ = ±11.8 cycles/mm, $2f_{z\text{-}NY}$ = ±1 cycles/mm).

range of tomosynthesis acquisition. For scheme 4, the presampling MTF does not extend beyond $f_{z\text{-}NY}$ = ±0.5 cycles/mm due to the application of the ST filter. The quantitative comparison of MTF can be better visualized using the 1-D MTF plot shown in Figure 5.14(b) for $f_y = f_z = 0$. The MTF for scheme 1 drops rapidly with normalization by spoke

density. Its poor high frequency response predicts poor detection of calcifications. The MTF for schemes 2 and 3 mainly differ in the high frequency response due to the application of the SA filter. Since the ST filter affects the response in the *z*-direction only, the 1-D MTF plot for schemes 3 and 4 essentially overlap.

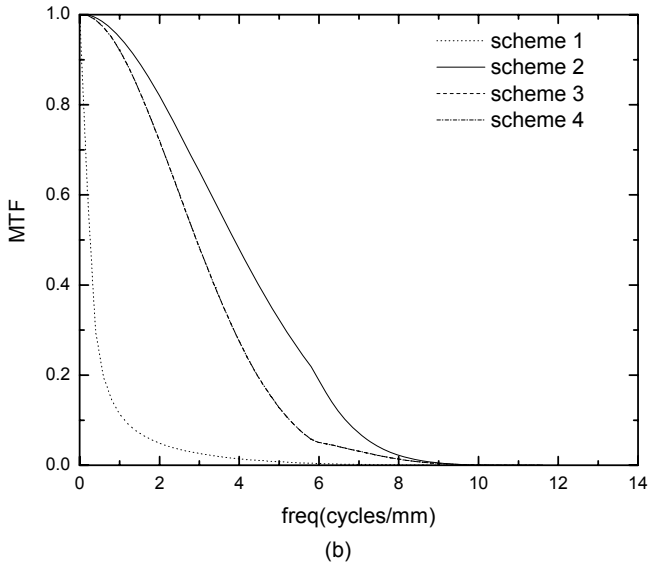

Figure 5.14 b) in-depth MTF at $f_z = 0$ for the four filter schemes. Angular range = ±20°. The curves for scheme 3 and 4 overlap because the response of the ST filter is unity at $f_z = 0$.

5.5.2 In-plane presampling MTF

Shown in Figure 5.15(a) is the presampling in-plane MTF for all four filter schemes calculated by integrating the 3-D MTF (Figure 5.13) in z-direction using Eq. 5.22. The result corresponds to the in-plane presampling MTF measured with a point, slit or edge with infinitesimal dimension in z-direction. The in-plane MTF are shown for frequencies up to $\pm 2f_{NY}$ (11.8 cycles/mm) in each direction. The shape of the MTF in y-direction is similar because the IN filter is identical for all cases. Due to the triangular shape of the sampled x-z frequency space (Figure 5.14a) and the integration along the z-direction, the

in-plane presampling MTF in x-direction also has a triangle shape at low frequencies for schemes 2-4. This is shown more clearly in the 1-D MTF plot in Figure 5.15(b) with f_y = 0.

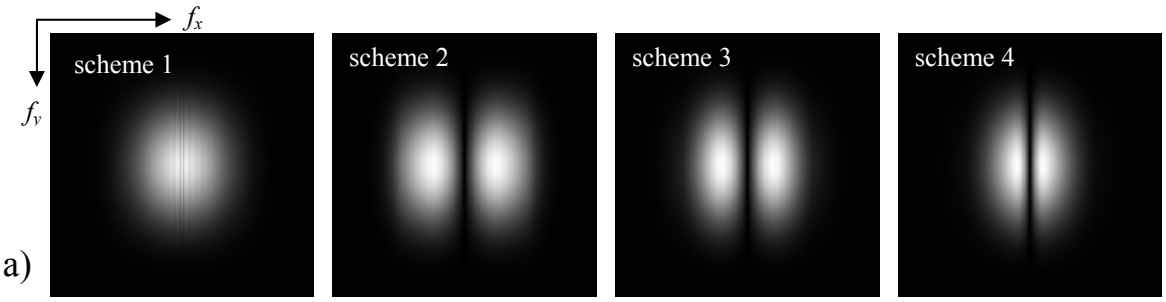

Figure 5.15 a) in-plane presampling MTF for different reconstruction filters. Angular range = ±20°. The MTF is plotted up to $2f_{NY}$ in each direction ($2f_{x\text{-}NY} = 2f_{y\text{-}NY}$ = ±11.8 cycles/mm).

The in-plane MTF for scheme 1 resemble the original MTF of the projection images because the effect of z-direction integration cancels out that due to spoke density. The high frequency decrease in MTF is due to the combined high frequency response of different filters, with scheme 4 having the lowest values. To quantify the effect of additional FSB due to tube motion, the in-plane MTF with and without FSB are shown in comparison in Figure 5.15(b).

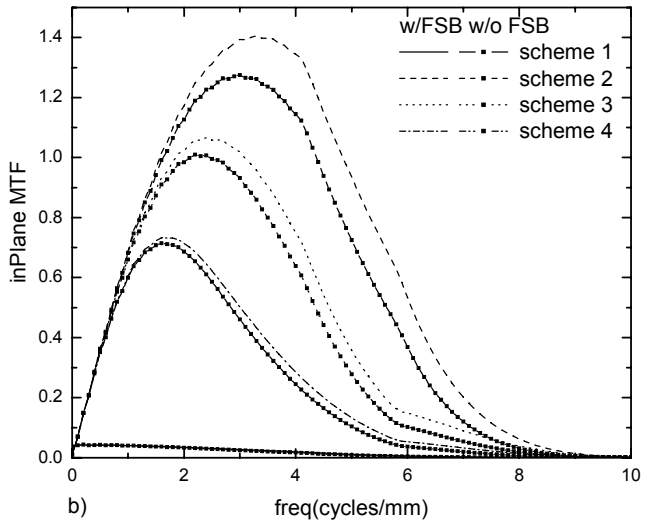

Figure 5.15 b) in-plane presampling MTF at f_y = 0 cycles/mm for the four filter schemes with and without FSB. Angular range = 40°.

The relative effect of FSB is less significant for schemes 3 and 4 compared to scheme 2 due to their poorer high frequency response to begin with. This is consistent to our previous study using a computer simulation platform.[57] Since FSB does not introduce correlation in NPS, DQE would be degraded by the square of the MTF.

Figure 5.16(a) shows the dependence of the in-plane MTF on angular range (±10°, ±20°, ±90°) for filter scheme 3. A voxel dimension of $d_x = d_y = 0.085$ mm and $d_z = 1$ mm was used for all cases. With complete data sampling (±90°), the low frequency drop in MTF disappears. To better visualize the effect of limited angular range, the in-plane MTF at $f_y = 0$ is plotted in Figure 5.16(b) for five different angular ranges. The low frequency response increases with the increase in angular range while the high frequency response remains unchanged. The low frequency drop in MTF due to limited angular range is the main reason for the edge enhancement and decrease in object contrast seen in the images of mass in breast tomosynthesis.[14, 57]

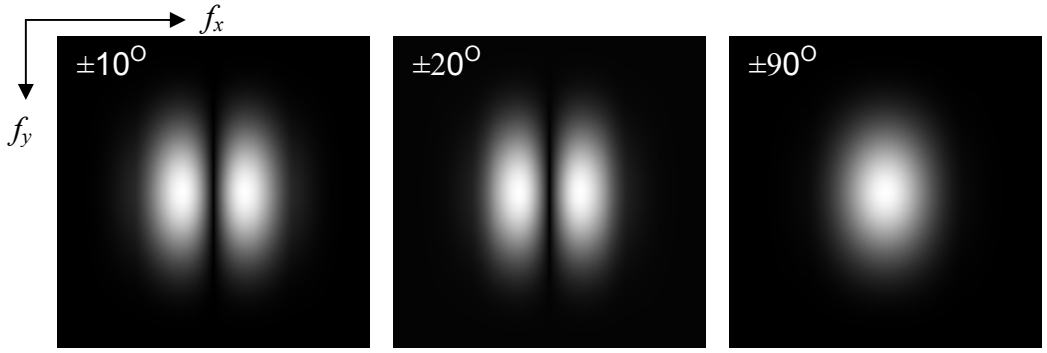

(a)

Figure 5.16 a) in-plane presampling MTF at three angular ranges using reconstruction scheme 3 and anisotropic voxel size (0.085 x 0.085 x 1 mm^3). The MTF is plotted up to $2f_{NY}$ in each direction ($2f_{x\text{-}NY} = 2f_{y\text{-}NY} = \pm 11.8$ cycles/mm).

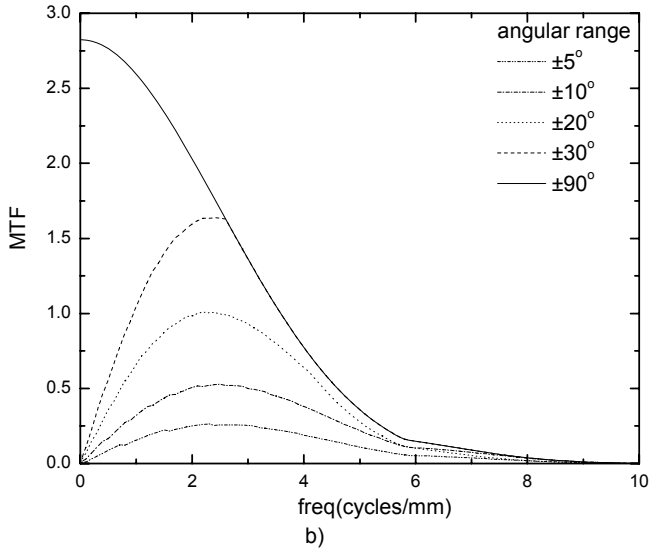

Figure 5.16 b) in-plane presampling MTF at f_y = 0 at various angular range, using reconstruction scheme 3 and anisotropic voxel size (0.085 x 0.085 x 1 mm^3).

5.6 DQE

The 3-D DQE was calculated as the ratio between the squared 3-D SNR at the output and that at the input,[15]

$$DQE_v(f_x, f_y, f_z) = \frac{\Psi_b(f_x, f_y, f_z)}{S_v(f_x, f_y, f_z) \times q_0} \tag{5.23}$$

where q_0 is the incident number of photons per view.

The 3-D DQE was calculated using Eq. 5.23 and the output signal and noise power spectra, Ψ_b and S_v, respectively. The results for schemes 3 and 4 are shown in Figure 5.17(a). The DQE are given up to f_{NY} in each direction. For scheme 3, the DQE exhibits a pattern that resembles the aliasing in NPS (S_v, Figure 5.8). To facilitate comparison, the 1-D DQE at $f_y = f_z = 0$ are plotted in Figure 5.17 (b). Without the ST filter (scheme 3), DQE drops by 50% at ~2.7 cycles/mm due to noise aliasing. With the ST filter (scheme

4), the DQE is not degraded from the projection DQE (Figure 5.3b). This demonstrates that the ST filter eliminates 3-D noise aliasing and preserves 3-D DQE. Also shown in Figure 5.17(b) are the calculated DQE with FSB. At f_{NY} = 5.88 cycles/mm, the additional drop of DQE due to FSB is 50%. This is because DQE is proportional to the square of the FSB blur function.

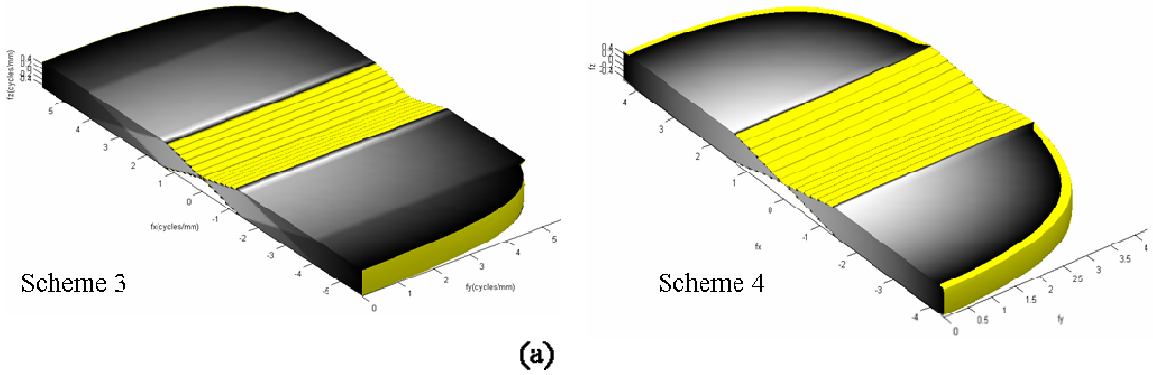

Figure 5.17 (a) 3-D DQE with scheme 3 and 4, The DQE is plotted up to f_{NY} in each direction ($f_{x\text{-}NY} = f_{y\text{-}NY}$ = ±5.88 cycles/mm and $f_{z\text{-}NY}$ = ±0.5 cycles/mm). Half of the y- axis is plotted. Lighter shade indicates higher value.

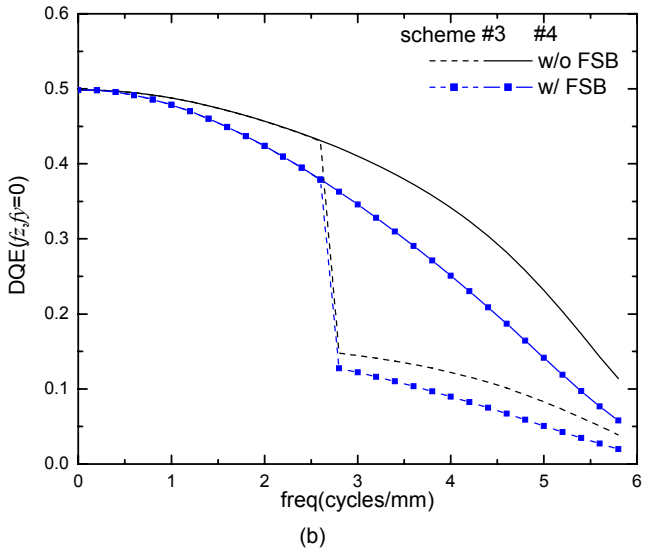

Figure 5.17 (b) 3-D DQE at $f_y = f_z = 0$ with scheme 3 and 4 with and without FSB.

5.7 Conclusions

The spatial frequency characteristics (in the form of 3-D NPS, MTF and DQE) of a breast tomosynthesis system were analyzed with a 3-D linear system model to investigate the dependence on acquisition geometry and reconstruction parameters. The low frequency response for in-plane MTF is limited due to incomplete sampling in tomosynthesis, and it can be improved by increasing the angular range. Both SA and ST filters help reduce high frequency noise. The ST filter eliminates 3-D noise aliasing, resulting in improved 3-D DQE.

Chapter 6

A Three-dimensional Linear System Analysis Framework for Optimization of Breast Tomosynthesis: Experimental validation

In Chapter 5, we developed a cascaded linear system model for tomosynthesis using similar methods as that developed for CT and CBCT. Using this systematic approach, the effects of imaging geometry, reconstruction filter, detector performance and radiation dose on 3-D imaging performance metrics can be integrated into the same analysis frame work. In this chapter, the experimental measurements of breast tomosynthesis imaging metrics were performed using a prototype system. The measured 3-D NPS and in-plane MTF were compared with results from our theoretical model. An ACR phantom was also imaged to investigate the impact of acquisition geometry and reconstruction filters.

6.1 Introduction

The reconstructed image quality in breast tomosynthesis depends on many factors. To achieve the best clinical outcome it is crucial to understand the fundamental imaging characteristics of this technology. Resolution and noise transfer characteristics are essential metrics for image quality assessment for 2-D radiography and 3-D tomography. Both MTF and NPS have been used as important parameters for detector characterization in projection imaging[19, 20]. These image quality metrics have also been extended to 3-D for conventional CT or CBCT. In CT the MTF was usually characterized using the PSF derived from the cross-sectional image of a wire placed in the longitudinal direction of a CT scanner[88]. Methods for measuring the presampling MTF were also developed using

the slanted edge (for CT)[89], or a wire[90] and sphere[91] (for CBCT). The theoretical model and experimental measurement of 3-D NPS were conducted for both CT[75] and CBCT[78]. It was found that the NPS is asymmetrical and dependent on reconstruction filters[75] [78].

Quantitative measurements of image quality for tomosynthesis, in terms of resolution and noise, have been performed mainly using in-plane images, i.e. the plane parallel to the detector. Chen *et al* measured the in-plane NPS and NEQ with scattered radiation and three reconstruction methods[72]. The in-plane spatial resolution was studied by different investigators through simulated images of a point[73, 92] and a wire[57], or experimental measurements using edge[84] and wire[85] phantoms. Previously we built a computer simulation platform to study the effect of imaging geometry and reconstruction methods[57]. The in-plane presampling MTF was calculated from the reconstructed images of a slanted W wire. It was found that the in-plane MTF was determined by reconstruction filter as well as imaging geometry. The determination of resolution in the thickness direction has been quantified by artifact spread function (ASF)[55, 57, 93, 94] and slice sensitivity profile (SSP)[84, 95] in the spatial domain. The quality of phantom[13, 93] and patient images[10, 55, 71] was investigated as a function of reconstruction algorithms and imaging conditions at a given glandular dose. Due to the limited view number and angular range of tomosynthesis acquisition, previous investigations were mainly focused on the effects of reconstruction methods. There is a lack of comprehensive measurement on the 3-D noise characteristics of breast tomosynthesis.

6.2 System operation

The experimental measurements were performed on a prototype breast tomosynthesis system which has been described in detail in Chapter 4. Two imaging modes were used in the present investigation, and their image acquisition and reconstruction parameters are summarized in Table 6.1. In mode 'x25', 25 views were acquired with full detector resolution within 20.8 s. In mode 'x25bin', 25 views were acquired in detector binning (2x1) mode, which reduces the acquisition time to 12.7 s. In this mode, a software-binning in the y- direction (perpendicular to the tube moving direction) was applied on the projection image before reconstruction to form an effective pixel size of 170 μm. One consequence of reduced scan time is the increase in FSB due to a larger tube travel distance during x-ray exposure[79]. The effects of degraded spatial resolution on the detection of high frequency information, e.g. calcification, will be investigated.

Table 6.1 Image acquisition and reconstruction parameters for the two tomosynthesis imaging modes used in our experimental investigation.

Imaging protocol		x25	x25bin
Acquisition parameters	Detector operation mode	full resolution	2x1 binning
	Angular range	$\pm 20^{o}$	$\pm 20^{o}$
	View number	25	25
	Scanning time	20.8s	12.7s
	Total mAs	144 mAs	144 mAs
Reconstruction parameters	Softbinning(2x2)	No	Yes
	Nyquist frequency($f_{x\text{-NY}}$)	5.88 cycles/mm	2.94 cycles/mm
	A (SA window width)	1.5 (8.8 cycles/mm)	1.5 (4.4 cycles/mm)
	B (ST window width)	0.1 (0.59 cycles/mm)	0.2 (0.59 cycles/mm)

The image reconstruction was performed with FBP algorithm described in detail previously[14] and in Chapter 5. The *A* and *B* values, window width factors respectively for the SA and ST filter for the two imaging modes are listed in Table 6.1. To investigate

the effects of image reconstruction on tomosynthesis image quality, four different filter schemes were applied for each acquisition mode, and the details are summarized in Table 6.2.

Table 6.2. Summary of the filter schemes for FBP reconstruction

Filter scheme 1	Simple backprojection (SBP)
Filter scheme 2	Ramp H_{RA} only
Filter scheme 3	H_{RA} x H_{SA}
Filter scheme 4	H_{RA} x H_{SA} x H_{ST}

Since most of the images in our present investigation were uniform noise images or for small phantoms, a small reconstructed volume of interest (VOI) containing 40 slices was used for all images in our investigations. The number of in-plane pixels varied from 512x512 (for noise and MTF measurement) to 1000x1000 (phantom study). The projection image for each view was cropped according to the VOI prior to the application of filters to minimize the reconstruction time. The slice thickness was 1 mm, and the in-plane pixel size was 0.085 x 0.085 mm^2, resulting in an anisotropic voxel size of 0.085 x 0.085 x 1 mm^3. The same voxel size was used for both acquisition modes to facilitate comparison despite their difference in projection image resolution.

6.3 3-D NPS

6.3.1 Measurement setting

The experimental method for 3-D NPS measurement is depicted in Figure 6.1. To avoid the effect of scattered radiation on the NPS measurements, a 3.95 cm thick Lucite block was placed at the x-ray tube output during image acquisition. The uniform noise images were acquired using both ‘x25’ and ‘x25bin’ modes at four different exposure levels ranging from 72 to 576 mAs, corresponding to a total detector entrance exposure

of 0.59-4.71 mR. As a reference for comparison, 144 mAs is equivalent to a mean glandular dose of 1.7 mGy to a 4 cm breast with average density (50/50).

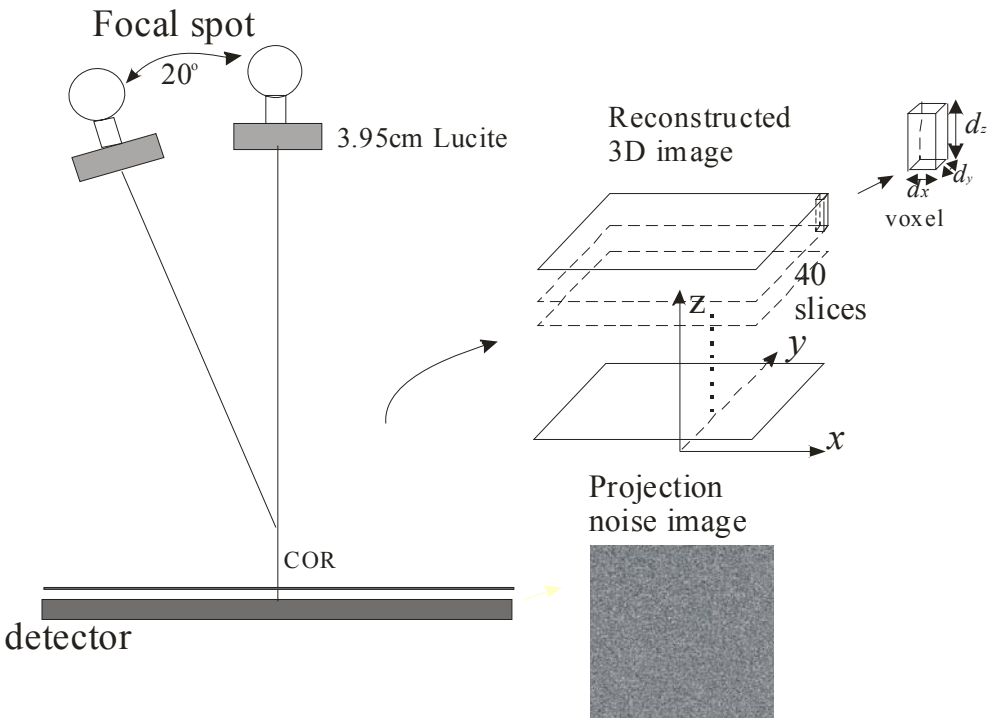

Figure 6.1 Diagram showing the imaging geometry for NPS measurement (left). An example of project image with uniform noise is shown in lower right, and the dimension of the reconstructed volume is shown in upper right.

The reconstructed 3-D images contained only noise, and the VOI of 512 x 512 x 40 voxels was divided into 16 sub-images, each containing 128 x 128 x 40 voxels. One realization of 3-D NPS was calculated from each sub image by taking the 3-D Fourier transform of the mean subtracted volume data. The final NPS, $S(f_x, f_y, f_z)$, was obtained as the ensemble average of all the NPS realizations:

$$S(f_x, f_y, f_z) = \frac{d_x d_y d_z}{N_x N_y N_z} < | FT[I(x,y,z) - \bar{I}(x,y,z)] |^2 > \qquad (6.1)$$

where N_x, N_y and N_z are the number of voxels in the x, y and z directions, respectively, for each sub-image I, and d_x, d_y and d_z are the voxel dimension in the corresponding

directions (Figure 6.1). The voxel noise variance (σ_v^2) in the spatial domain could be determined as the integral of the 3-D NPS as:

$$\sigma^2_v = \iiint S(f_x, f_y, f_z) df_x df_x df_z \tag{6.2}$$

After the 3-D NPS was calculated, an evaluation of the in-plane 2-D NPS for any selected slice, $S_{avg}(f_x, f_y)$, could be obtained by integrating the 3-D NPS along the z- direction up to $f_{z\text{-NY}}$:

$$S_{avg}(f_x, f_y) = \int_{-f_{z-\text{NY}}}^{f_{z-\text{NY}}} S(f_x, f_y, f_z) df_z \tag{6.3}$$

In a stationary system, $S_{avg}(f_x, f_y)$ from Eq. 6.3 should be equal to the 2-D NPS calculated using any slice of the reconstructed image. However since our prototype system uses a cone beam, it is not strictly stationary. To test the assumption of stationarity in our linear system model, we compared the $S_{avg}(f_x, f_y)$ obtained using Eq. 6.3 with the 2-D NPS calculated using individual reconstructed slices. In our tomosynthesis geometry with limited angular range, the top slice (z = 40) is expected to deviate the furthest from a parallel beam assumption. Therefore its NPS (S_{40}) was used for comparison, and the values were calculated using the standard method for 2-D projection images:

$$S_{40}(f_x, f_y) = \frac{d_x d_y}{N_x N_y} < | FT[I(x, y, z = 40) - \bar{I}(x, y, z = 40)] |^2 > \tag{6.4}$$

6.3.2 Results

For ease of comparison and visualization of results, the 3-D NPS measurements are evaluated using three methods: (1) the integrated voxel variance to quantify the overall perception of noise in the reconstructed images; (2) in-depth NPS, which is the 3-D NPS

in the x-z plane to visualize the effect of reconstruction filters and angular range; (3) in-plane NPS, which is directly related to the slice-by-slice viewing of reconstructed tomosynthesis images.

1. Voxel variance

Shown in Figure 6.2 is the voxel variance calculated using Eq. 6.2 as a function of total mAs. Filter Scheme 3 was used for both 'x25bin' and 'x25' modes.

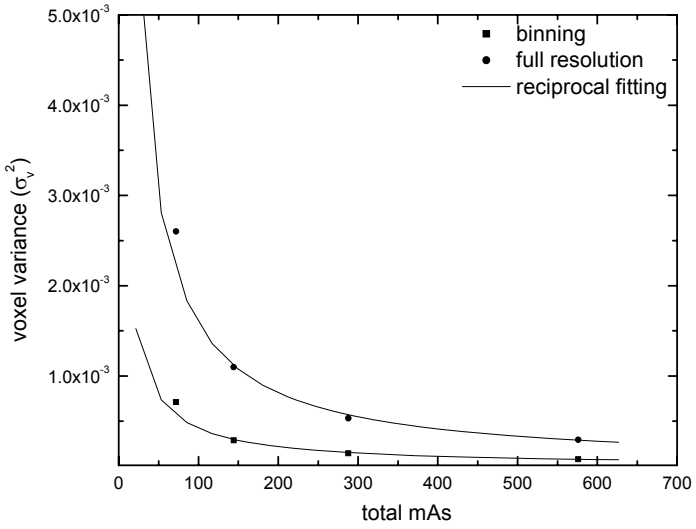

Figure 6.2 Voxel variance as a function of total mAs with reconstruction scheme 3 in full resolution ('x25') and binning ('x25bin') mode. The variance versus exposure curves were fitted with reciprocal relationship.

Figure 6.2 shows that the variances is inversely proportional to mAs, this is consistent with the behavior of FBP for CT. Because the detector performance is dominated by x-ray quantum noise at the exposure level used in each scan[79]. the pixel variance of the projection image after logarithm transformation is inversely proportional to the mean of the projection image, and hence to the entrance exposure. Figure 6.2 also shows that the variance in full resolution mode is approximately four times that in binning mode. This is

consistent with the high intrinsic resolution of a-Se detectors, which leads to a quadruple increase in the number of x-ray quanta detected per pixel after 2x2 softbinning.

2. In-depth NPS

Figure 6.3 shows the comparison between measured and modeled in-depth (x-z) NPS (with $f_y = 0$) for 'x25' mode using all four filter schemes. The total exposure used for the acquisition was 144 mAs. The center of each NPS image is the zero frequency, and the results are shown up to f_{NY} in each direction ($f_{x\text{-}NY} = \pm 5.88$ cycles/mm and $f_{z\text{-}NY} = \pm 0.5$ cycles/mm). The modeled and measured NPS results show essentially identical pattern, which proves that the Fourier slice theorem can be used in the linear system model to fill data in the 3-D frequency space. Near the origin (zero frequency), only a small angular range of the frequency space is filled, which is consistent with the angular range ($\theta = \pm 20^o$) used in our tomosynthesis acquisition. Figure 6.3a shows that the 3-D NPS with SBP is simply the projection NPS replicated at different angles, therefore the intensity of NPS is the highest at the origin. Noise aliasing is manifested as increased NPS intensity at high frequencies due to the replication of NPS at multiples of $2f_{NY}$. With the application of the RA filter, as shown in Figure 6.3b, the NPS decreases at low frequencies, and increases at high frequencies, causing the noise aliasing to be more visible. The application of SA filter (Figure 6.3c) reduces the magnitude of high frequency noise. The main difference with the application of ST filter (Figure 6.3d) is that it essentially eliminated the frequency components above $f_{z\text{-}NY}$, hence noise aliasing is negligible.

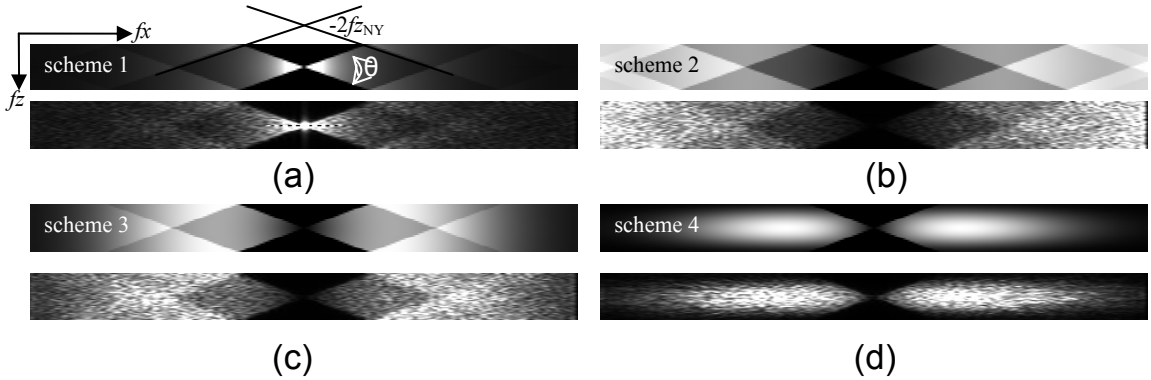

Figure 6.3 Comparison between modeled (top) and measured (bottom) NPS for mode 'x25' using all four reconstruction schemes listed in Table 6.2. Figures a, b, c, and d are for filter schemes 1, 2, 3 and 4, respectively. The total exposure used for the acquisition was 144 mAs. The NPS is shown up to f_{NY} in each direction ($f_{x\text{-}NY}$ = ±5.88 cycles/mm and $f_{z\text{-}NY}$ = ±0.5 cycles/mm)

Shown in Figure 6.4 are the calculated and measured in-depth NPS for 'x25bin' mode. The main difference, compared to the results in Figure 6.3, is the reduced frequency response in the x- direction due to pixel binning, which formed an effective pixel size of 170 μm. Since the voxel dimension of the reconstructed images is the same as in full resolution (85 μm), the f_{NY} of the reconstructed images is unchanged. Although binning helps reduce high frequency noise, the degraded frequency response affects the detection of different objects. Qualitative evaluation for this effect will be addressed in the phantom study.

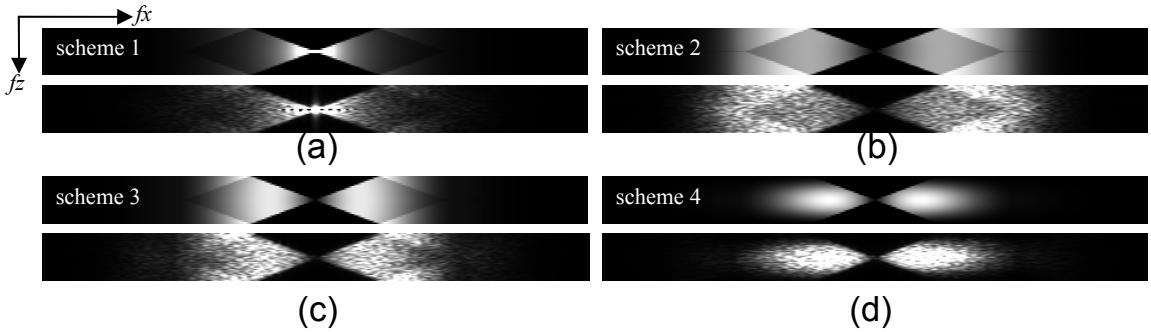

Figure 6.4 Comparison between modeled (top) and measured (bottom) NPS for mode 'x25bin' using all four reconstruction schemes listed in Table 6.2. Figures a, b, c, and d are for filter schemes 1, 2, 3 and 4, respectively. The total exposure used for the acquisition was 144 mAs. The NPS is shown up to f_{NY} in each direction ($f_{x\text{-}NY}$ = ±5.88 cycles/mm and $f_{z\text{-}NY}$ = ±0.5 cycles/mm)

To demonstrate the effect of angular range, the noise images were reconstructed using a subset of the projection images with an angular span of ±10°. The resulted in-depth NPS are shown in Figure 6.5 for reconstruction schemes 3 and 4, and the results for the full angular range (Figure 6.3) are replotted for comparison. The total dose for the two angular ranges was comparable. Figure 6.5 (a) shows the sampled area at low frequencies decreases with decrease in angular span. At high frequencies, the noise aliasing with wider angular span is more severe. After the ST filter is applied, as shown in Figure 6.5 (b), the aliasing at high frequencies is eliminated. The limited sampling at low frequencies for smaller angular range is unchanged. Angular range will affect the detection of low frequency objects, i.e., masses, as will be discussed in the phantom study (Section 6.5)

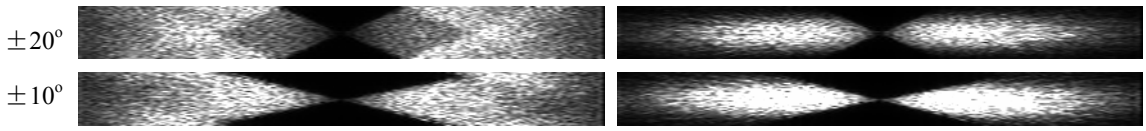

Figure 6.5 Measured in-depth NPS with two angular ranges: ±20° (top) and ±10° (bottom) for: (a) filter scheme 3; and (b) filter scheme 4. The detector was operated in full resolution mode, and the total mAs used for each scan was ~144 mAs. The NPS is shown up to f_{NY} in each direction ($f_{x\text{-}NY}$ = ±5.88 cycles/mm and $f_{z\text{-}NY}$ = ±0.5 cycles/mm)

3. In-plane NPS

Shown in Figure 6.6 (a) and (b) are the modeled and measured in-plane NPS for modes 'x25' and 'x25bin', respectively. The top row of each figure shows the modeled results for all four filter schemes. Shown in the middle row are the experimental results derived from the 3-D NPS measurement using Eq. 6.3, which provides an estimate of the average in-plane NPS of all slices. Shown in the bottom row are the 2-D NPS of the top slice. The in-plane 2-D NPS are shown up to $f_{x\text{-}NY} = f_{y\text{-}NY}$ = ±5.88 cycles/mm. The

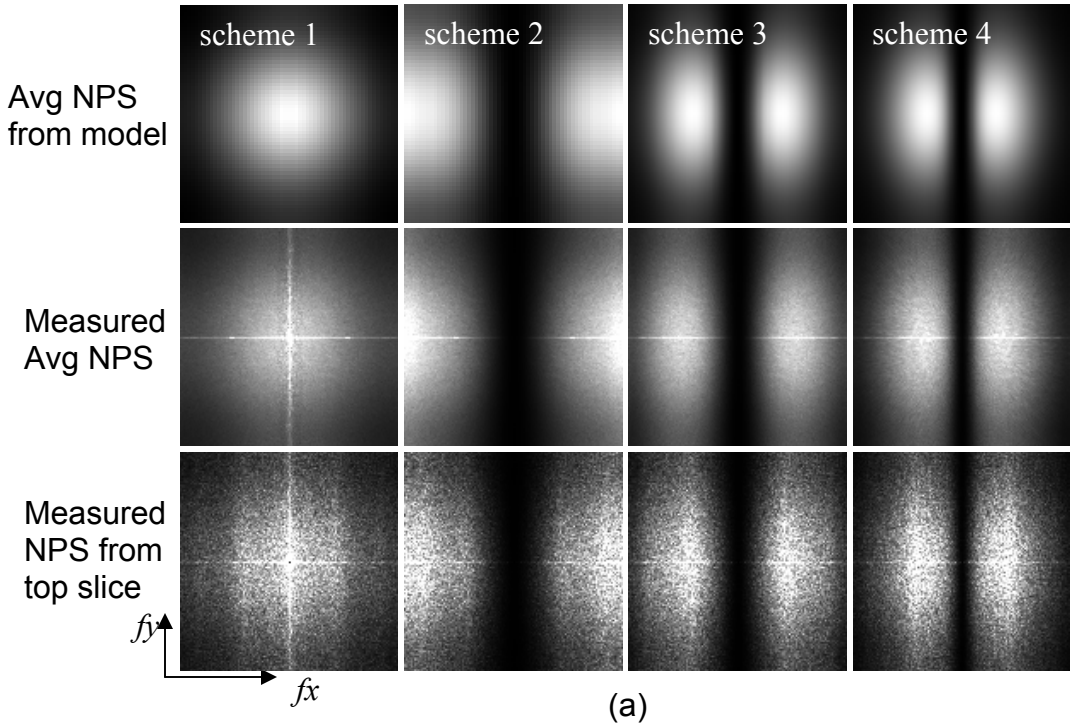

Figure 6.6 (a) In-plane NPS for 'x25' mode with all four reconstruction schemes (column 1-4 from the left for filter schemes 1-4) The top row is the in-plane NPS calculated using the model; the middle row is the average in-plane NPS from the measurement; and the bottom row is the measured NPS of the top slice.

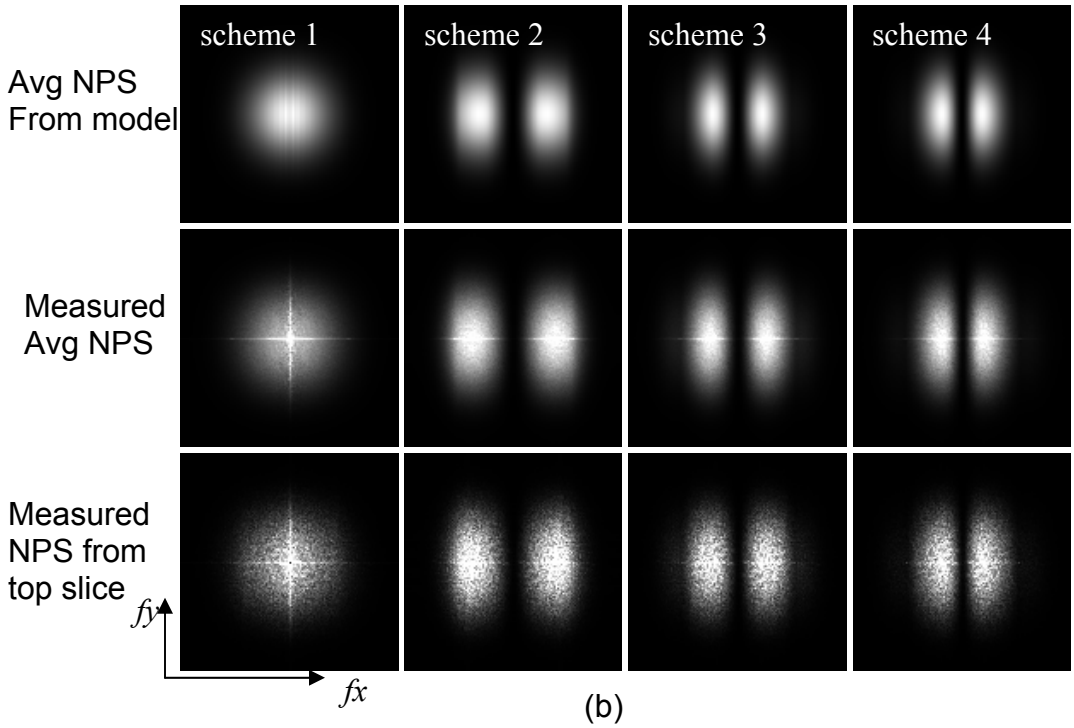

Figure 6.6 (b) In-plane NPS for 'x25bin' mode with all four reconstruction schemes (column 1-4 from the left for filter schemes 1-4) The top row is the in-plane NPS calculated using the model; the middle row is the average in-plane NPS from the measurement; and the bottom row is the measured NPS of the top slice.

measured NPS contains higher noise on the zero frequency axes, which is caused by the non-uniformity in the 3-D images. Figure 6.6 shows that except for filter scheme 1 with SBP reconstruction, all FBP schemes have anisotropic in-plane NPS. The decrease in NPS in y- direction is due to the interpolation filter used in our voxel-driven FBP reconstruction. The NPS at high frequencies is lower for 'x25bin' mode due to pixel binning in both directions before FBP reconstruction.

To facilitate quantitative comparison, the measured and modeled NPS in x-direction at f_y = 0 cycles/mm, i.e. the central slice of the 2-D NPS in Figure 6.6, are plotted in Figure 6.7. Due to the high noise on central axes in the measured data, four lines on either side of f_y = 0 cycles/mm were used to compute the results. Figure 6.7 (a) shows the results for 'x25' mode and filter schemes 3 and 4. The parabolic shape of the NPS is due to the reconstruction filters. The low frequency drop is due to the RA filter, and the high frequency drop is due to the combined effects of the SA and ST filters, both of which degrade high frequency response[75]. The results show excellent agreement between the model and the two measurements, which represent the average and the top slice. This confirms the validity of our model and shows that the assumption of shift-invariance is reasonable. Shown in Figure 6.7 (b) are the results for 'x25bin' mode and filter schemes 2-4. The NPS level is the highest for scheme 2, and the measured NPS for all filter schemes agree well with the model. Due to pixel binning, the high frequency noise is much lower than that in full resolution mode.

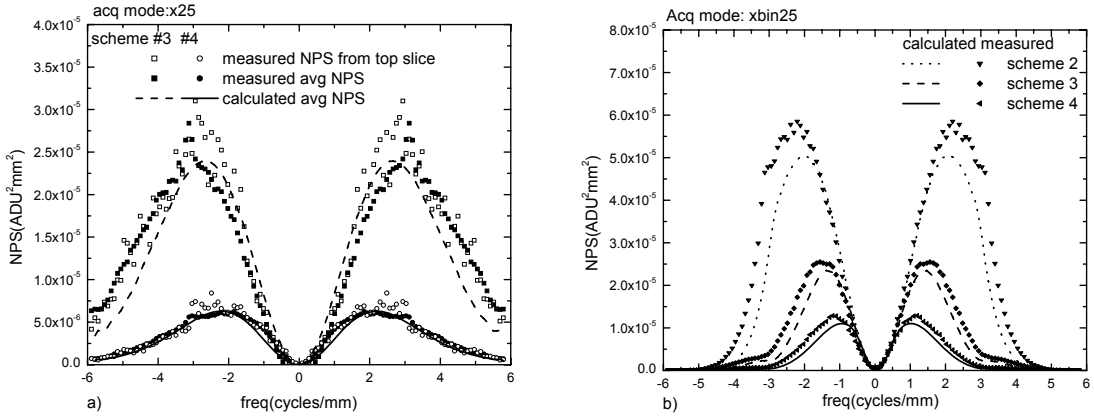

Figure 6.7 a) Comparison between modeled and measured in-plane NPS in the x-direction (with f_y = 0 cycles/mm) for filter schemes 3 and 4 in mode 'x25'. b) Comparison between modeled and measured in-plane NPS in the x-direction for filter schemes 2-4 in mode 'x25bin'.

6.4 Spatial Resolution

6.4.1. Measurement setting

The spatial resolution of the system was characterized using its in-plane presampling MTF, which was measured with the slanted edge method[62-64]. An aluminum (Al) edge phantom with 0.2 mm thickness was made using 99% pure Al sheet. This particular thickness was chosen for the following reasons: 1) The shadow created by the thickness of the edge at the maximum tube angle (20^o) should not introduce any error in the MTF measurement; 2) the projection radiographic contrast of the edge phantom should be reasonably small so that the logarithmic transformation before FBP reconstruction can be regarded as a linear process. As shown in Figure 6.8, the edge was placed 4 cm above the center of the detector surface near the chest wall side, and at a small angle ($2\text{-}5^o$) from the gate line (y-) direction of the detector. The projection images were acquired using 'x25' mode with a total exposure of 144 mAs, corresponding to a total raw detector exposure of 523 mR. The measurement of the in-plane MTF was performed using the reconstructed

image slice for the plane where the edge was placed. It has the highest image contrast for the edge. Figure 6.8 shows an example of the reconstructed edge image, from which the ESF was deduced. As shown in Figure 6.8, the ESF shows a strong edge enhancement, which is the characteristic of FBP reconstruction with limited angular range.

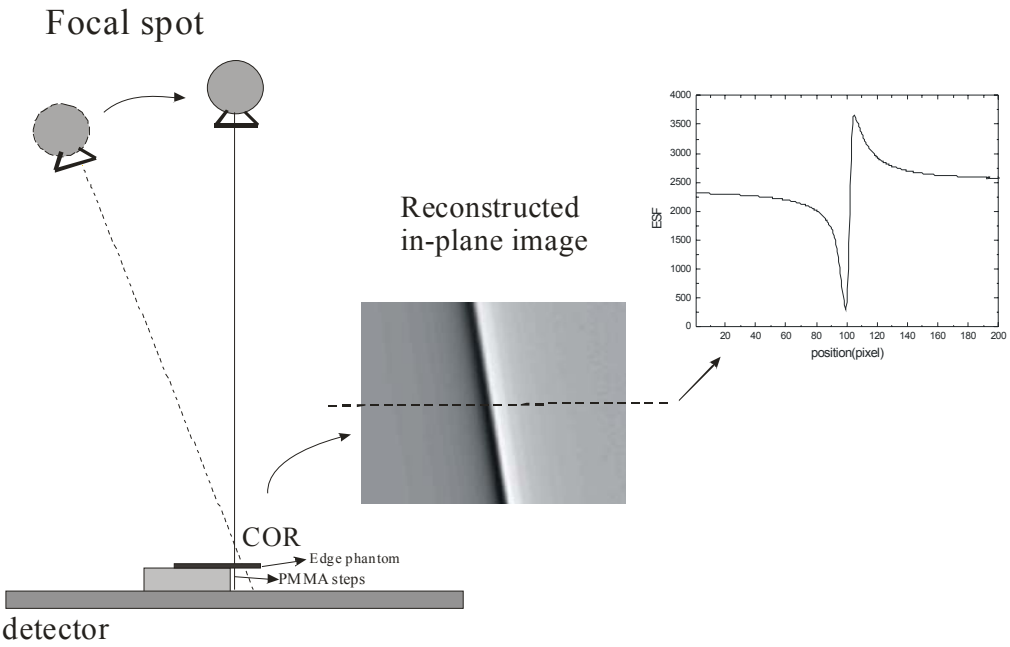

Figure 6.8 Diagrams showing the method for experimental measurement of in-plane MTF: Experimental setting for the measurement of in-plane MTF using an edge phantom and a PMMA block was used to elevate the edge phantom to a given distance (left); an example of reconstructed in-plane edge image (center); and the ESF function derived from the edge image (right).

6.4.2 In-plane MTF

Shown in Figure 6.9 (a) are the measured in-plane presampling MTF for all four reconstruction filter schemes. Since the zero spatial frequency response after reconstruction is not always the highest, the in-plane MTF for each reconstruction scheme is normalized by its own maximum response. The decrease in MTF at low spatial frequencies for filter schemes 2-4 is due to the RA filter and the incomplete angular sampling in tomosynthesis. This phenomenon is not observed in CT or CBCT with

complete angular sampling[89]. The peak of the MTF curves shift toward lower frequencies from schemes 2-4 due to the application of SA and ST filter that reduce high

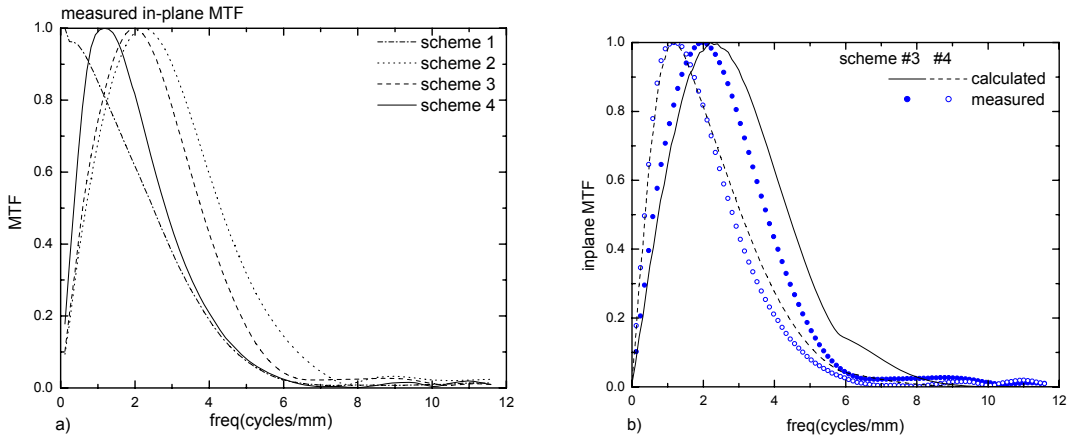

Figure 6.9 (a) Measured in-plane presampling MTF with the four reconstruction schemes for acquisition mode 'x25', b) The comparison between measurement and model for filter scheme 3-4

frequency response. Shown in Figure 6.9 (b) are the comparisons between measured and modeled in-plane MTF for filter schemes 3-4, which are most frequently used in our study for noise reduction purposes. Reasonable agreement between model and measurement was observed for both filter schemes. Compared with modeled results, the measured MTF is lower at higher frequencies. The discrepancy is more pronounced in scheme 3 when more high frequency component is allowed through. This is mainly due to discrepancy between model assumption and measurement conditions: (1) the modeled in-plane MTF was calculated by integrating the 3-D MTF in z-direction (Chapter 5), which is valid for an edge phantom with infinitesimal thickness. The finite thickness (0.2 mm) of the edge phantom in our measurement leads to reduced high frequency components in z-direction and hence a lower in-plane MTF. However with the application of ST filter, this factor should be negligible since the thickness of the edge is only 1/5 of the slice thickness. (2) the MTF measurement is phase dependent because the

slice thickness is larger than the phantom thickness[86, 87]. The calculation assumes the edge phantom in perfect alignment with the center of the slice. In practice, this is difficult to do and there is usually a slight shift, which results in a measured in-plane MTF that is position dependent and could be lower than the modeled result. Since the ST filter removes aliasing in z-direction, it makes the in-plane MTF phase independent. Therefore the agreement between measured and modeled results is better with filter scheme 4.

Shown in Figure 6.10 are the comparisons of the measured in-plane presampling MTF with filter schemes 3 and 4 for two different angular ranges of ±10° and ±20°. It

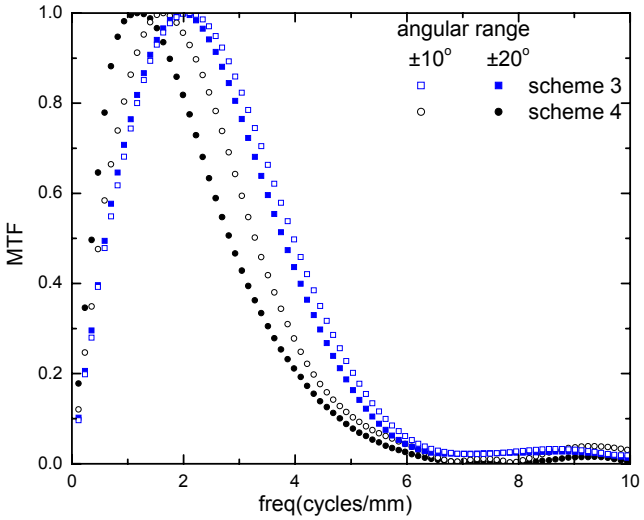

Figure 6.10 Measured in-plane presampling MTF with filter scheme 3-4 for two angular ranges: ±10° and ±20°.

shows that increased angular range improves the MTF at low frequencies because of the increased coverage of sampled space, as depicted clearly in the in-depth NPS figure (Figure 6.5). This is consistent with the results from model calculation in Chapter 5. Further increase of angular range in breast tomosynthesis is difficult due to the limitation in hardware design: (1) a larger fraction of the x-ray projection will fall outside of the

stationary detector; (2) larger focal spot blur if the number of views and scan time are kept the same.

6.5 Phantom Study

6.5.1 Phantom Imaging Experiment

The above frequency domain image quality metrics provide quantitative evaluation of the imaging performance, and facilitate the fundamental understanding of the effects of system parameters on breast tomosynthesis. In this section, we will investigate the image characteristics of different objects after tomosynthesis reconstruction, and relate the results to spatial frequency domain image quality metrics. An ACR mammography accreditation phantom was imaged with different acquisition modes and reconstruction filters. Two angular spans were used: 1) $\pm 20^{o}$; and 2) $\pm 10^{o}$ with the same angular separation and total glandular dose (~1.7 mGy). The second configuration was achieved by doubling the total mAs for the tomosynthesis scan and reconstructing the 3-D image using half (13) of the acquired images. Since two detector operational modes can be used for each angular span, a total of four tomosynthesis imaging modes were resulted: (1) binning mode ('x25bin') with $\pm 20^{o}$; (2) binning mode ('x25bin') with $\pm 10^{o}$, (3) full resolution ('x25') with $\pm 20^{o}$; and (4) full resolution ('x25') with $\pm 10^{o}$. The reconstructed image slice for the plane that contains the wax insert of the ACR phantom, where the images of all the objects are in sharp focus, was used for image quality evaluation. For comparison, the ACR phantom was also imaged using the screening mode on the prototype tomosynthesis system, i.e. one exposure from the 0 degree tube angle. The

image was acquired with the same x-ray spectrum and comparable total exposure (140 mAs) as in breast tomosynthesis.

1. Calcifications

The reconstructed image intensity profile of the largest calcification specks, i.e. Cal-1 with diameter d = 0.54 mm) was examined to investigate the effect of image acquisition and reconstruction parameters on the detection of small and high contrast object. The profile was taken across the center of Cal-1 and normalized by the maximum intensity. This method facilitates quantitative comparison between the contrast and sharpness of the detection of calcifications.

2. Mass

The reconstructed image quality of mass was quantified using the signal difference to noise ratio (SDNR). The SDNR for the two largest masses: Mass-1 with d = 2 mm and Mass-2 with d = 1 mm, was calculated using:

$$SDNR = (\rho_{mass} - \rho_{bak}) / \sigma_{bak} \tag{6.5}$$

where ρ_{mass} and ρ_{bak} are the mean reconstructed in-plane pixel intensity values for the mass and the background, respectively, and σ_{bak} is the standard deviation of the background. The value for ρ_{mass} was computed from a circular region of interest (ROI) with 50-pixel diameter in the center of the mass image. The background was chosen as an ROI with 100-pixel diameter in the center of the phantom where no object was present.

The image quality of each object was investigated as a function of the following two tomosynthesis parameters: a) filter schemes as listed in Table 6.2; and b) angular range and detector operation mode as listed in Table 6.1.

6.5.2 Results

Shown in Figure 6.11 is a projection image of the ACR phantom. The circles highlight the location of the mass and calcification features used in our quantitative analysis (Cal-1, Mass-1, and Mass-2).

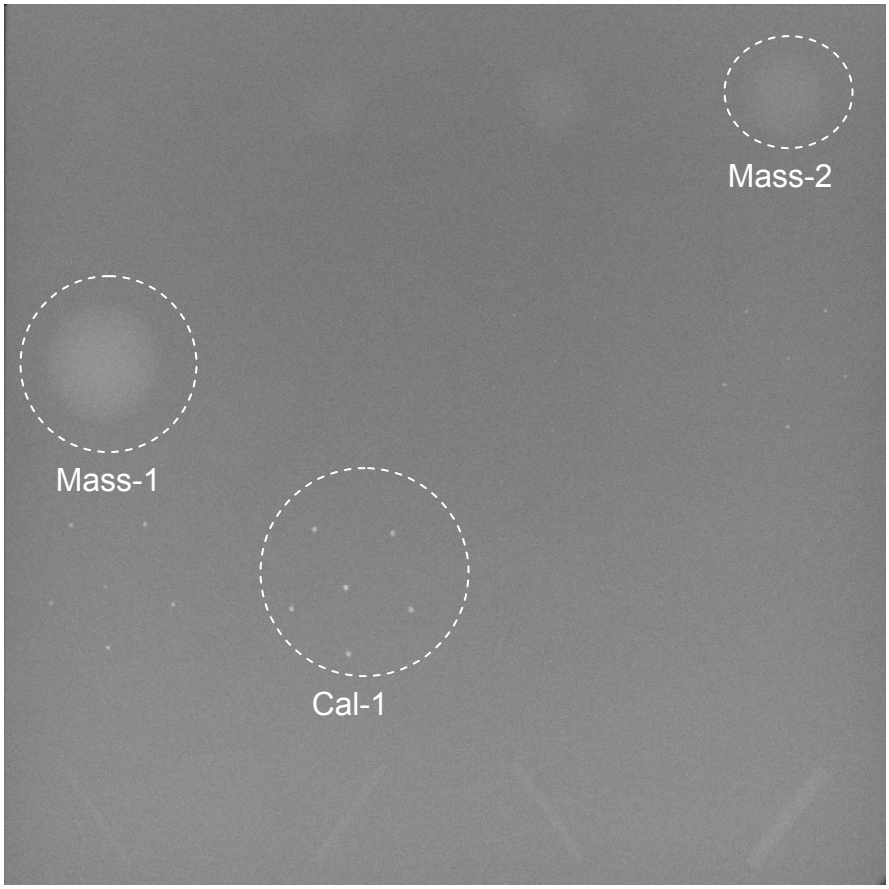

Figure 6.11 ACR phantom image obtained using the screening mode of the prototype tomosynthesis system with 28 kVp W/Rh and 140 mAs.

In this section, we will first present the dependence of ACR phantom images on reconstruction filters, and then on tomosynthesis acquisition parameters, i.e. angular range and detector operational modes.

1. Dependence on reconstruction filters

Shown in Figure 6.12 (a) are the comparisons of the in-plane images of the ACR features using four different filter schemes with 'x25bin' mode. It shows that the image obtained using filter scheme 1 is blurry, leading to difficulty in the detection of the third

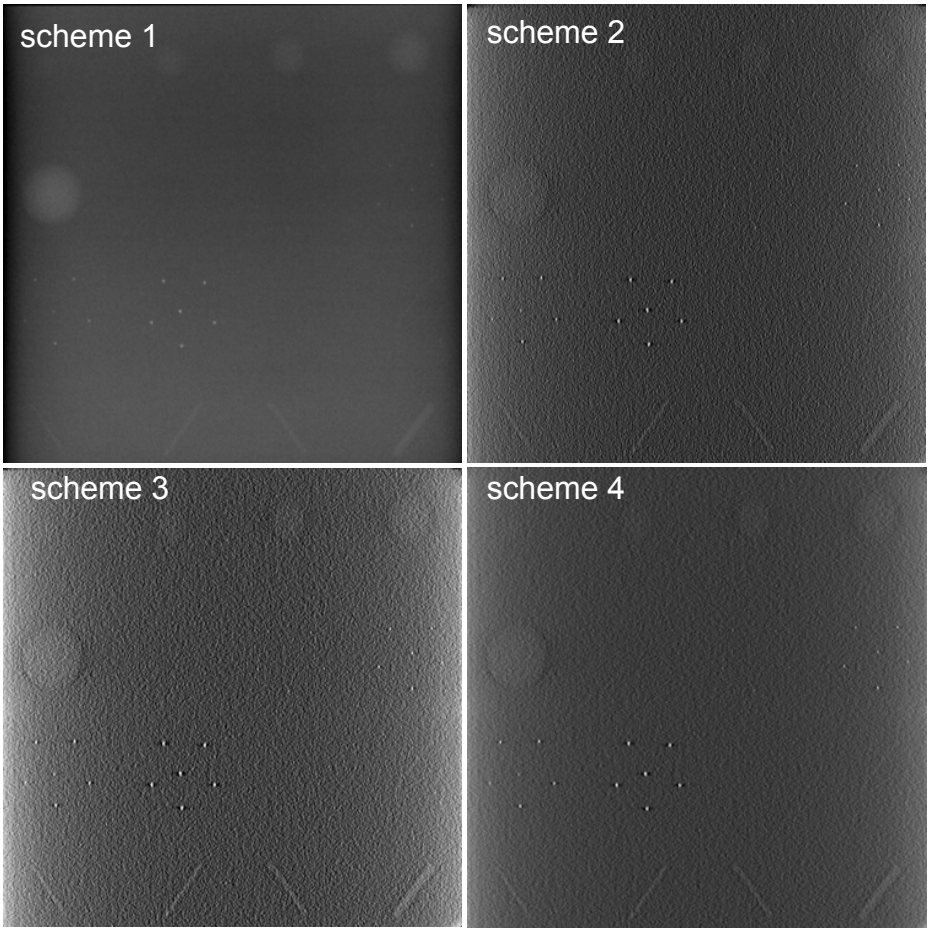

(a)

Figure 6.12 (a) ACR phantom image reconstructed with the four schemes. The acquisition mode was 'x25bin' with total 144 mAs. The scan direction is along the horizontal direction of the image.

group of calcification specks. Using the other filter schemes (2-4), all the features that are visible in screening mammography (Figure 6.11) can be seen in the reconstructed in-plane image. The reconstructed images of the mass with filter schemes 2-4 show a clear edge enhancement along the tube travel direction (horizontal direction in the image). This is due to the application of RA filter to the image data acquired with a limited angular range, and has been seen quantitatively in the model and measurement of the in-plane MTF (Figure 6.9). Compared with schemes 3 and 4, the noise level is higher in scheme 2, which is expected from the lack of noise reduction at high frequencies.

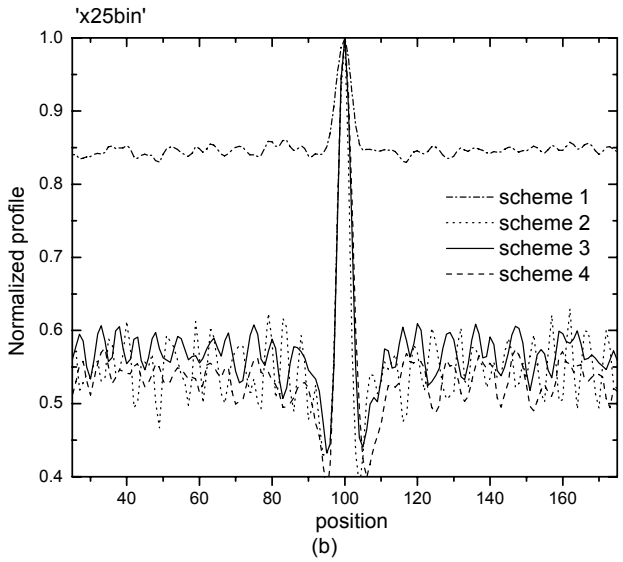

Figure 6.12 (b) Normalized profile for Cal-1 for the four filter schemes. The acquisition mode was 'x25bin' with total 144 mAs,

a. Calcifications

Plotted in Figure 6.12 (b) are the normalized profiles of Cal-1 for the four reconstruction schemes. Edge enhancement (shown as undershoot and overshoot) is observed for schemes 2-4, but not for scheme 1. The signal amplitude with scheme 1 is poor due to the poor high frequency response associated with SBP. The profiles for filter

scheme 2-4 are similar in shape, however their noise levels differ. The noise is the highest in Scheme 2 due to the lack of Hanning windows to limit high frequency noise.

b. Mass

The measured SDNR for the two mass features with different reconstruction filters are listed in Table 6.3. Since SDNR changes as a function of both signal difference and noise, the background noise level σ_{bak} (Eq. 6.5) is also listed in Table 6.3 to facilitate comparison. The SDNR for Mass-1 is larger than that for Mass-2, as expected from the higher inherent contrast in Mass-1. Scheme 1 has the highest SDNR in all reconstruction schemes due to two reasons: (1) mass contains mainly low frequency information, where scheme 1 (SBP) has the highest response; (2) the poor high frequency response of scheme 1 effectively reduces noise. With the application of the SA and ST filters for schemes 3 and 4, there is significant improvement in SDNR compared to scheme 2 due to the suppression of noise. The background noise σ_{bak} decreases ~50% from scheme 2 to scheme 4. In addition to the SDNR, the edge enhancement of the mass features is expected to help the detection with tomosynthesis.

Table 6.3 SDNR and background noise for Mass-1 and Mass-2 for the four reconstruction schemes acquired in 'x25bin' with total 144 mAs.

SDNR	Filter scheme 1	Filter scheme 2	Filter scheme 3	Filter scheme 4
Mass-1	9.921	0.995	1.615	2.535
Mass-2	6.390	0.727	1.260	1.970
σ_{bak}	21.28	93.49	70.58	58.54

2. Dependence on the angular range and detector operational mode

The reconstructed images with four different combinations of angular range and detector operational mode are shown in Figure 6.13(a). All the images were acquired with comparable total exposure (144-149 mAs) and reconstructed with filter scheme 4.

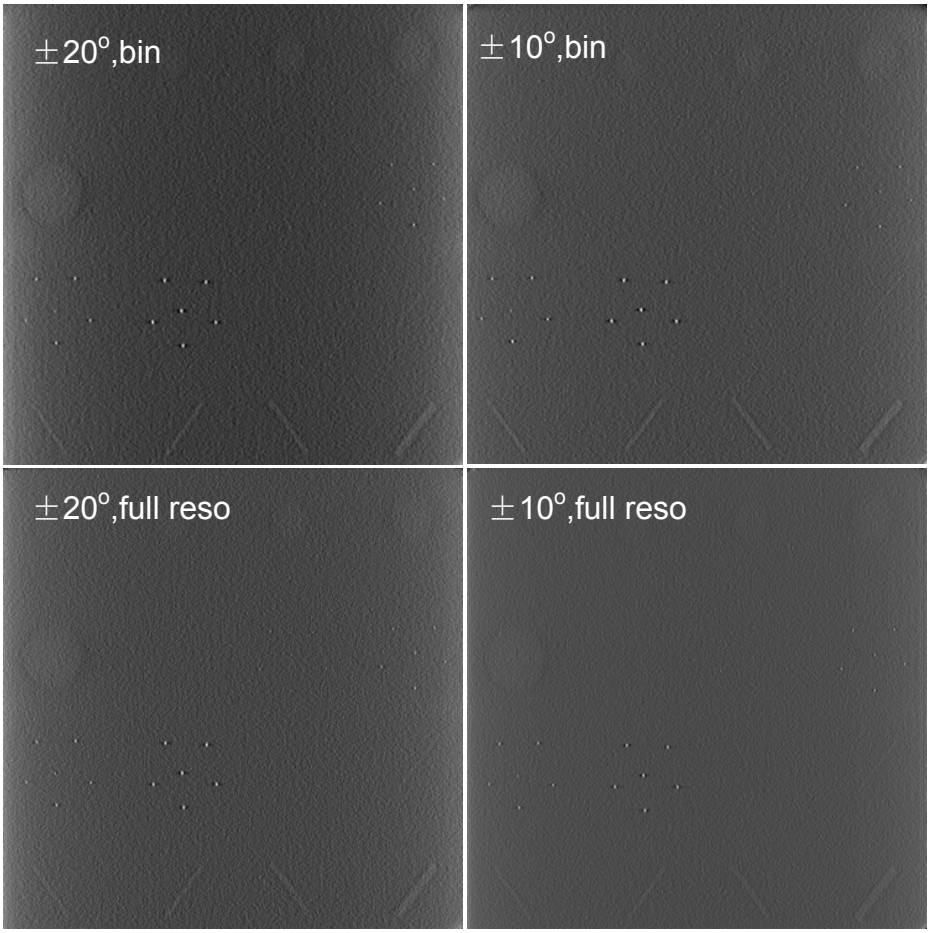

(a)

Figure 6.13 (a) ACR phantom image reconstructed obtained with four acquisition modes: 1) binning mode with ±20°; 2) binning mode with ±10°; 3) full resolution with ±20°; 4) full resolution with ±10°. The images are with same angular separation between views, comparable total mAs (144-149 mAs) and were reconstructed using filter scheme 4.

a. Calcification

The pixel intensity profiles for the images of Cal-1 in Figure 6.13(a) are shown in Figure 6.13 (b). Since the plots overlap significantly, only the results for the full

resolution mode are shown for clarity. It shows that wider angular range improves contrast. The present study of the tradeoff between full resolution and binning mode is limited by the ACR phantom, which is designed for screening mammography. The calcification feature is made from aluminum oxide (Al_2O_3), whose attenuation is lower than the actual microcalcifications in the breast. The smallest calcifications visible on screen mammography using 28 kVp W/Rh spectrum is 0.24 mm, which was detectable by tomosynthesis in both full resolution and binning modes.. A wider range of calcification sizes is needed to further investigate possible advantages of full resolution versus binning mode in the detection of small objects.

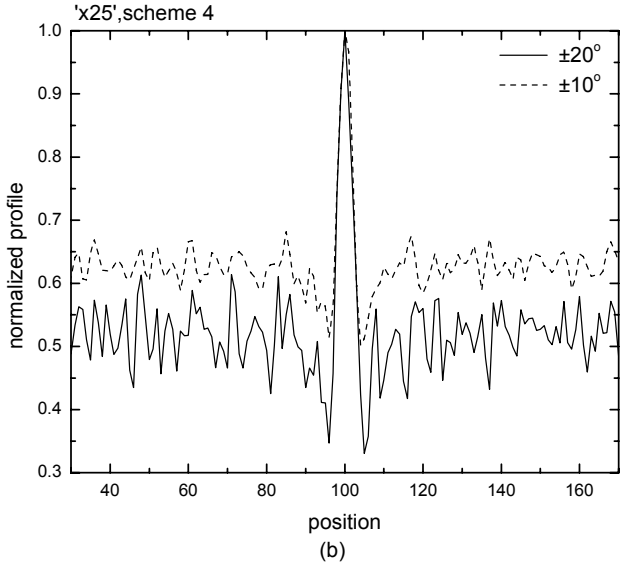

Figure 6.13 (b) Normalized profile for Cal-1 for two angular ranges, ±10° and ±20°, reconstructed using filter scheme 4. The acquisition mode was 'x25' with total exposure of 144 mAs

b. Mass

The calculated SDNR and background noise for Mass-1 and Mass-2 are shown in Table 6.4. Doubling of the angular range to ±20° increases the SDNR by ~30% despite its higher background noise level. This indicates that the image quality of large, low

contrast objects such as mass can be improved by increasing the angular range, which improves the low frequency response. This result is consistent with the MTF measurement in Figure 6.10. The SDNR in binning mode is almost three times that of the full resolution mode. This is mainly due to the two fold decrease in σ_{bak} by pixel binning,[79] and the combined effects of binning and reconstruction filters on the signal spectrum of the objects.

Table 6.4 SDNR and background noise for Mass-1 and Mass-2 with four tomosynthesis imaging modes with comparable total mAs (144-149 mAs) and filter scheme 4.

SDNR	x25bin, ±20^o	x25bin, ±10^o	x25, ±20^o	x25, ±10^o
Mass-1	2.535	1.392	0.827	0.599
Mass-2	1.970	1.349	0.683	0.496
σ_{bak}	58.54	44.53	120.05	81.31

6.6 Conclusions

We investigated the spatial frequency domain image quality metrics for a prototype tomosynthesis system. The 3-D NPS and in-plane presampling MTF were investigated as a function of acquisition geometry, detector operational mode and reconstruction filters. The measured NPS and MTF have reasonable agreement with theoretical calculation using a cascaded linear system model for tomosynthesis. The image characteristics of the objects (mass and calcifications) on an ACR phantom show good correlation with the quantitative measurement of NPS and MTF. The detection of mass can be improved by binning and increasing the angular range. Improvement in mass detection can also be achieved by the application of the SA and ST filters, which reduces high frequency noise and eliminates aliasing.

Chapter 7

Resolution in Thickness Direction

7.1 Introduction

In breast tomosynthesis only several projection views are acquired within a limited angular range to reconstruct 3-D images. As a result artifacts appear in reconstructed image slices that do not contain the actual object. These artifacts could lead to difficulty in diagnosis[69, 71, 96]. As shown in Figure 7.1, the artifact in breast tomosynthesis is a blurred version of the in-plane image feature. The intensity of the artifact is higher as the plane gets closer to the actual object. The artifact is manifested as several "ghosts" in the tube travel (x-) direction of the image, and the number of ghosts is equal to the number of views.

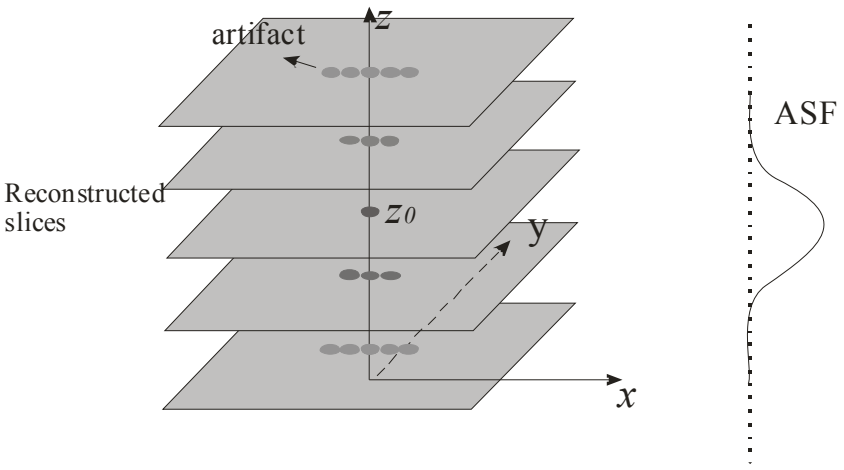

Figure 7.1 Diagram showing artifacts in breast tomosynthesis(left) and the measurement of ASF(right) .

From the imaging theory point of view, these artifacts are due to the limited resolving power of tomosynthesis in z-direction. The z-direction resolution has been quantified

using ASF[55, 57, 93, 94] and SSP[84, 95], both of which are defined in the spatial domain. Wu *et al* first proposed ASF to quantify the intensity of artifact spreading in z-direction[55]. and has been adopted by other investigators for similar studies[57, 93]. ASF is defined as the normalized amplitude of the artifact as a function of the distance from the object location:

$$ASF(z) = \frac{\rho_a(z) - \rho_b(z)}{\rho_o(z_0) - \rho_b(z_0)} \tag{7.1}$$

where z_0 and z are the locations of the object and the artifacts, respectively. ρ_o and ρ_b are the average pixel intensities of the object (or its ghost) and the background, respectively. ASF with wider spread represents worse object resolving power in the z-direction. It depends on imaging geometry, reconstruction methods (e.g., filters for FBP), and the size of the object[55, 57, 93, 94].

ASF of a small object is essentially a measure of the PSF in z-direction, which can be obtained theoretically from the inverse Fourier transform of the 3-D MTF. In the next section, the theoretical foundation of ASF will be established from the linear model. Model validation using CT simulation and tomosynthesis measurement will then be presented.

7.2 Theory

From the linear system model, the 3-D PSF can be calculated as the inverse Fourier transform of the 3-D MTF:

$$
\begin{aligned}
&T_v(f_x,f_y,f_z)=\sum_{i,j,k}T_b(f_x,f_y,f_z)\delta(f_x-\frac{i}{d_x},f_y-\frac{j}{d_y},f_z-\frac{k}{d_z}) \quad \text{(i, j, k as integer)}\\
&PSF(x,y,z)=\text{iFFT}(T_v(f_x,f_y,f_z)) \qquad \text{for } |f_x|\le f_{\text{x-NY}},|f_y|\le f_{\text{y-NY}},|f_z|\le f_{\text{z-NY}} \qquad (7.2)\\
&ASF=PSF(0,0,z)
\end{aligned}
$$

where $T_b(f_x,f_y,f_z)$ is the presampling MTF and d_x, d_y, d_z are the an reconstructed voxel dimensions. Since artifact only occurs in z-direction, the model calculation can be simplified and limited to x-z (in-depth) plane:

$$
\begin{aligned}
&T_v(f_x,f_z)=\sum_{i,k}T_b(f_x,f_z)\delta(f_x-\frac{i}{d_x},f_z-\frac{k}{d_z}) \quad \text{(i, k as integer)}\\
&PSF(x,z)=\text{iFFT}(T_v(f_x,f_z)) \qquad \text{for } |f_x|\le f_{\text{x-NY}},|f_z|\le f_{\text{z-NY}} \qquad (7.3)\\
&ASF=PSF(0,z)
\end{aligned}
$$

The approximation of ASF by PSF assumes the object to be a perfect point. In practice, ASF is always related to an object with certain size, e.g. a 100 μm microcalcification[57]. The model calculation was extended from Eq. 7.2 to incorporate the spatial frequency components of the object. The object is assumed to have a circular shape (in the x-z-plane). It is represented by a first order Bessel function in the spatial frequency domain:[97]

$$
S(f_x,f_z)=\frac{2}{d}\frac{J_1(\pi d\sqrt{f_x^2+f_z^2})}{\sqrt{f_x^2+f_z^2}} \qquad (7.4)
$$

where d is the object diameter in mm, and J_1 is the first order Bessel function. The ASF for this object can be calculated using:

$$
\begin{aligned}
&TS_b(f_x,f_z)=T_b(f_x,f_z)S(f_x,f_z)\\
&TS_v(f_x,f_z)=\sum_{i,k}TS_b\delta(f_x-\frac{i}{d_x},f_z-\frac{k}{d_z}) \qquad \text{(i, k as integer)}\\
&PSF_{\text{o}}(x,z)=\text{iFFT}[TS_v(f_x,f_z)] \qquad \text{for } |f_x|\le f_{\text{x-NY}},|f_z|\le f_{\text{z-NY}} \qquad (7.5)\\
&ASF=PSF_{\text{o}}(0,z)
\end{aligned}
$$

7.3 Demonstration using computer simulation

Computer simulations for CT were performed using Matlab. There are two functions that perform the basic CT reconstruction: 1) R = radon(I, θ) returns the Radon transform R of the intensity image I at projection angle θ, 2) I = iradon(R, θ, filter parameters) reconstructs the image I from projection data at angle θ into the 2-D array R. Selected reconstruction filters, i.e., RA, Hanning (width up to unity) can be applied for FBP reconstruction. Bilinear interpolation is applied to calculate the reconstructed image values. The reconstructed pixel has to be square and identical to projection image. The angle θ here is either a single arbitrary angle or an array of individual angles. Therefore it is capable of limited angle/limited view FBP reconstruction into isotropic voxel size.

A noise free image containing a point source in the center was simulated as the PSF image. Each simulated image has a matrix size of 235x235 with a uniform background of equal intensity at unity. The point source (one pixel) has intensity of 10. The pixel size of the image is 0.085 mm. In order to investigate the effect of angular range and view number, four acquisition (Acq) conditions were simulated: 1) $\pm 20^{o}$ with 25 views, 2) $\pm 20^{o}$ with 7 views, 3) $\pm 10^{o}$ with 25 views, and 4) $\pm 10^{o}$ with 7 views. The angular separation between views for these conditions varied from 0.8-6 degrees. The filters applied during reconstruction were RA and Hanning (with window width of 1) and linear interpolation was used.

Shown in Figure 7.2 are reconstructed PSF images in the spatial domain (left) and their Fourier transform (right) for Acq 1(Figure 7.2a) and Acq 2(Figure 7.2b) from simulation and model data. The results from model calculation have similar image pattern as those from the computer simulation. The MTF images show that only areas within the

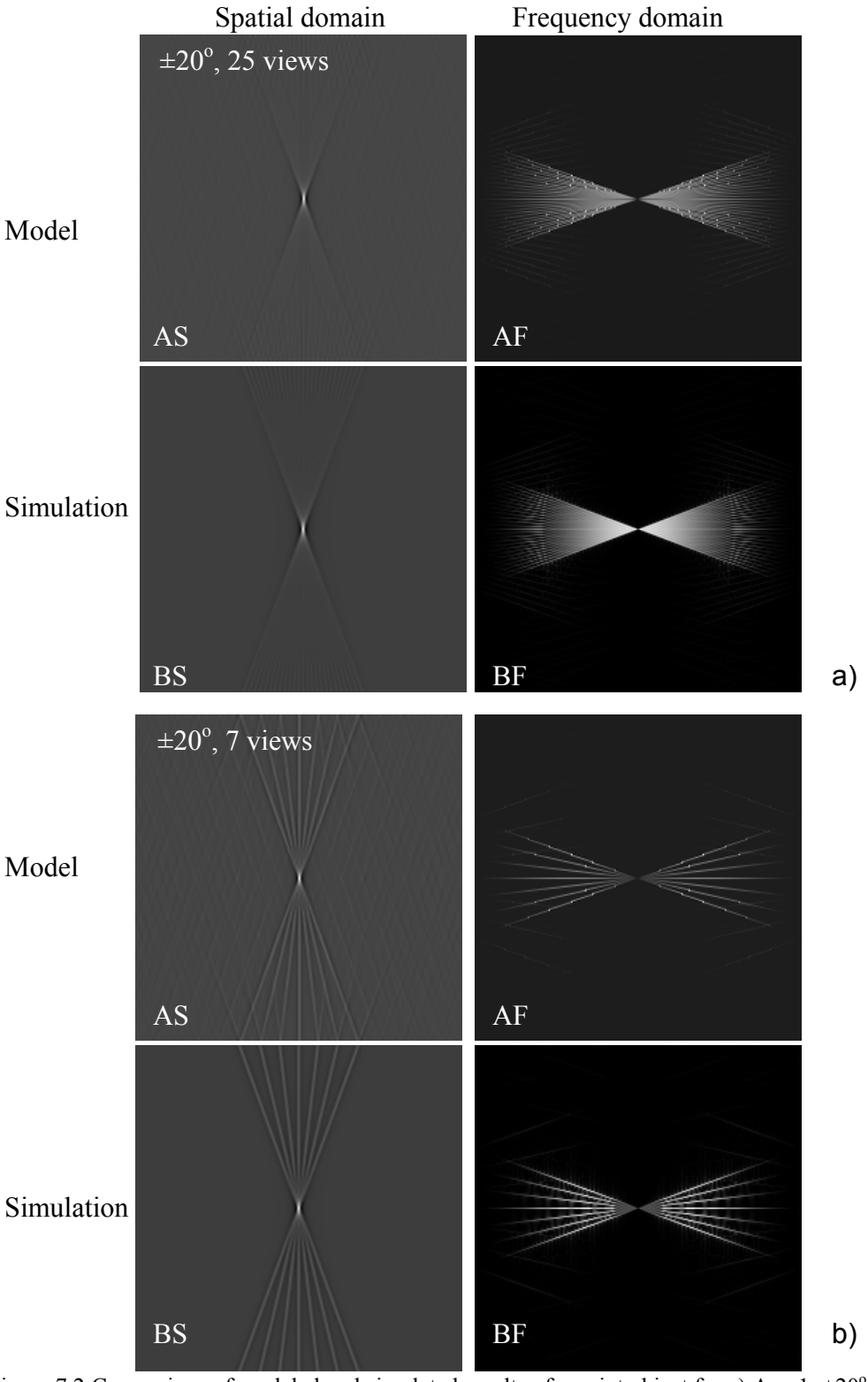

Figure 7.2 Comparison of modeled and simulated results of a point object for a) Acq 1: ±20° with 25 views and b) Acq 2: ±20° with 7 views. Subimages: AS) calculated PSF, AF) calculated MTF, BS) PSF from simulation, BF) MTF from simulation.

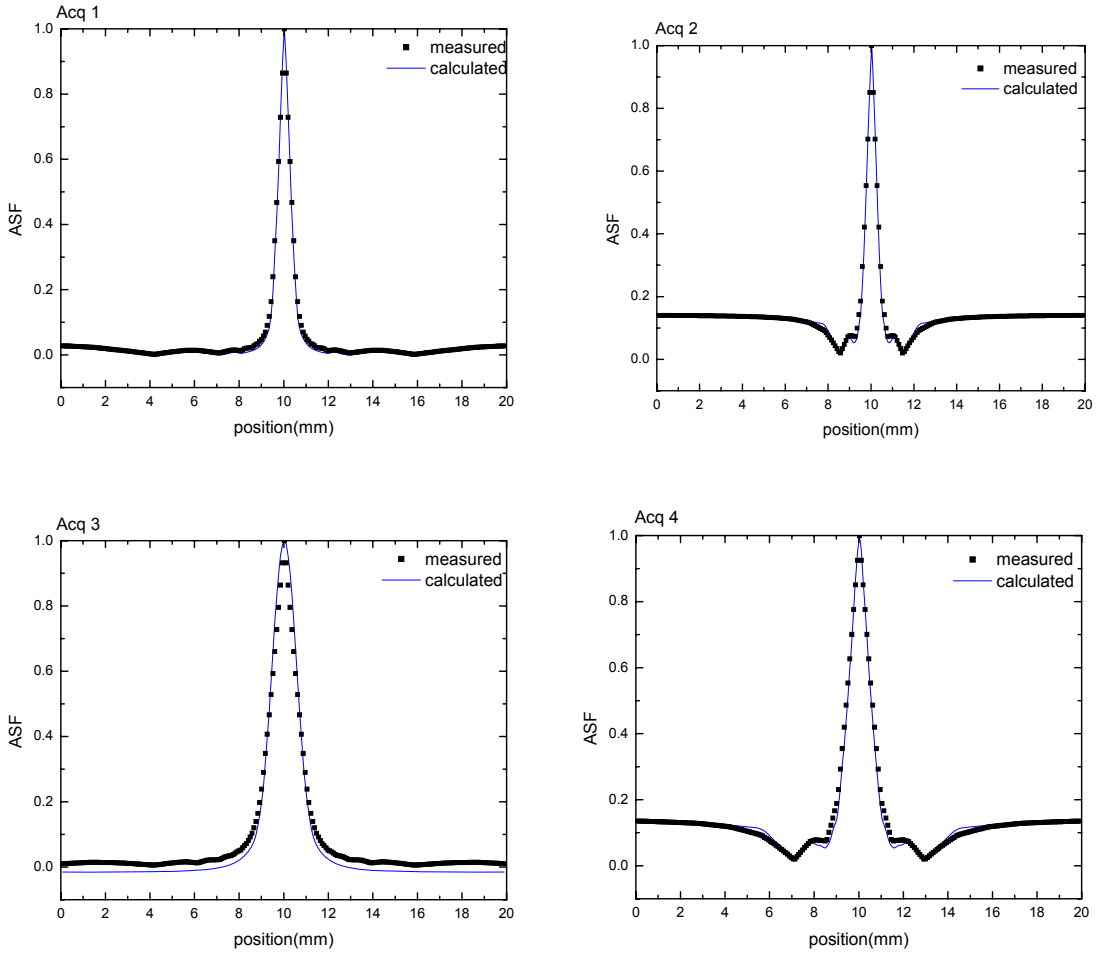

Figure 7.3. ASF of modeled and simulated results for Acq: 1) ±20^{o} with 25 views, 2) ±20^{o} with 7 views, 3) ±10^{o} with 25 views, 4) ±10^{o} with 7 views.

angular range (±20^{o}) were sampled. The sufficient angular separation (0.8 degree) in Acq 1 results in good uniformity for the reconstructed PSF image. With Acq 2, seven individual spokes corresponding to the projection views comprise the reconstructed PSF image. The reconstructed images show edge enhancement due to the combined effect of the RA filter and limited angular range. Shown in Figure 7.3 are the ASF curves calculated using the pixel values along the vertical(z-) axis of the PSF images in Figure 7.2. The comparisons between model and simulation result are given for all four acquisitions. The ASF is normalized by the signal intensity at the in-focus plane. The

model agrees well with simulations for all acquisitions. The small angular separation between views (Acq 1 and 3) results in ASF decreasing monotonously with distance from in-focus plane. With sparse sampling between views (Acq 2 and 4), ASF improves at the cost of ringing as the distance increases, shown as the undershoot and overshoot. Increasing angular range improves the sharpness of ASF. The HWHM (half width at half maximum) doubles when the angular range decreases from $\pm 20^o$ (Acq 1-2) to $\pm 10^o$ (Acq 3-4).

7.4 Demonstration in prototype breast tomosynthesis system

The measurement of ASF was performed on a prototype breast tomosynthesis system described in Chapter 4. A ball-bearing bead (BB) with 0.4 mm diameter was placed at 2 cm above the detector surface. Projection images were acquired in 'x49' mode (Chapter 4), where 49 views were acquired with an angular range of $\pm 20^o$. The projection images were reconstructed into a 3-D volume size of 240x240x40 with an anisotropic voxel size of $0.085 \times 0.085 \times 1 mm^3$. Four reconstruction schemes were implemented: 1) SBP, 2) with Ramp filter only, 3) with Ramp and Hanning filter (A=1), 4) with Ramp, Hanning (A = 1) and ST filters (B = 0.085). The description of the application of reconstruction filters and filter parameters is provided in Chapter 5 and 6.

Since the dimension (d = 0.4mm) of the BB is much larger than the pixel size of the detector in y-direction, the ASF can be approximated by the x-z plane response of the system (with $f_y = 0$). Therefore we simplified the 3-D object spectrum for the BB into 2-D in in-depth. With the simplified x-z plane model, the 2-D object spectrum for the BB was calculated using Eq. 7.4 and shown in Figure 7.4.

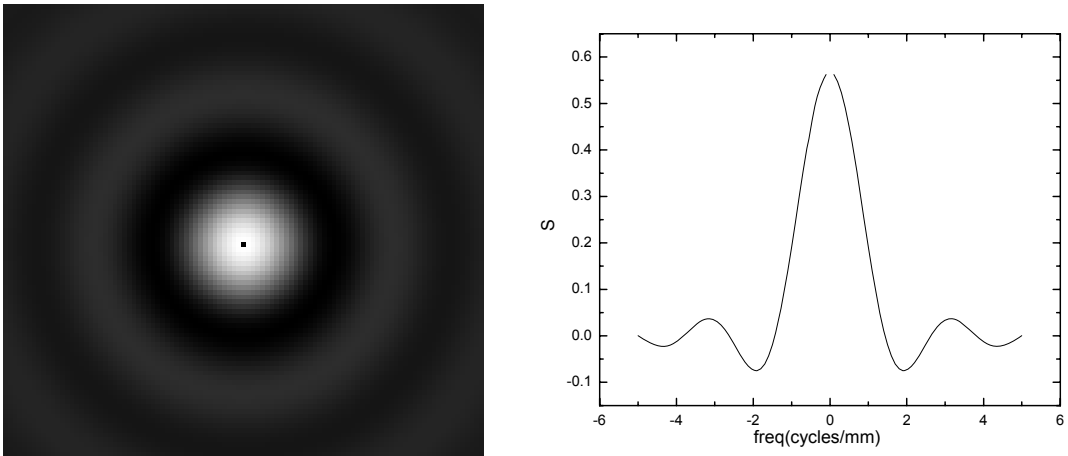

a) b)

Figure 7.4 Object spectrum (with d = 0.4 mm) in frequency domain, a) 2-D object spectrum, b) 1-D plot of object spectrum at $f_y = 0$.

The intensity of the out-of-plane artifact was measured using the central "ghost" of the bead artifact and Eq. 7.1. The results for all four filter schemes are plotted in Figure 7.5 in comparison to those from the model. The measurement and model results have excellent agreement. Scheme 1 (SBP) has the worst ASF due to lack of reconstruction filters. There is no significant difference between ASF for scheme 2 and 3. The application of ST filter (scheme 4) increases the spread of ASF. This is because the effective aperture function in z-direction is modified by the ST filter. Since the ST filter window width is much smaller than that of the original aperture function of the pixel size (1 mm) in z-direction, the resolution in z-direction is degraded.

7.5 Conclusions

The linear system model can predict the resolution in z-direction for breast tomosynthesis, which was usually quantified as ASF in previous studies. The model prediction was validated by CT computer simulation and ASF measurement of BB performed using a prototype breast tomosynthesis system. The resolution in z-direction

depends on reconstruction filters and acquisition geometry. Application of reconstruction filters modifies the shape of the ASF. ASF can be improved by increasing angular range.

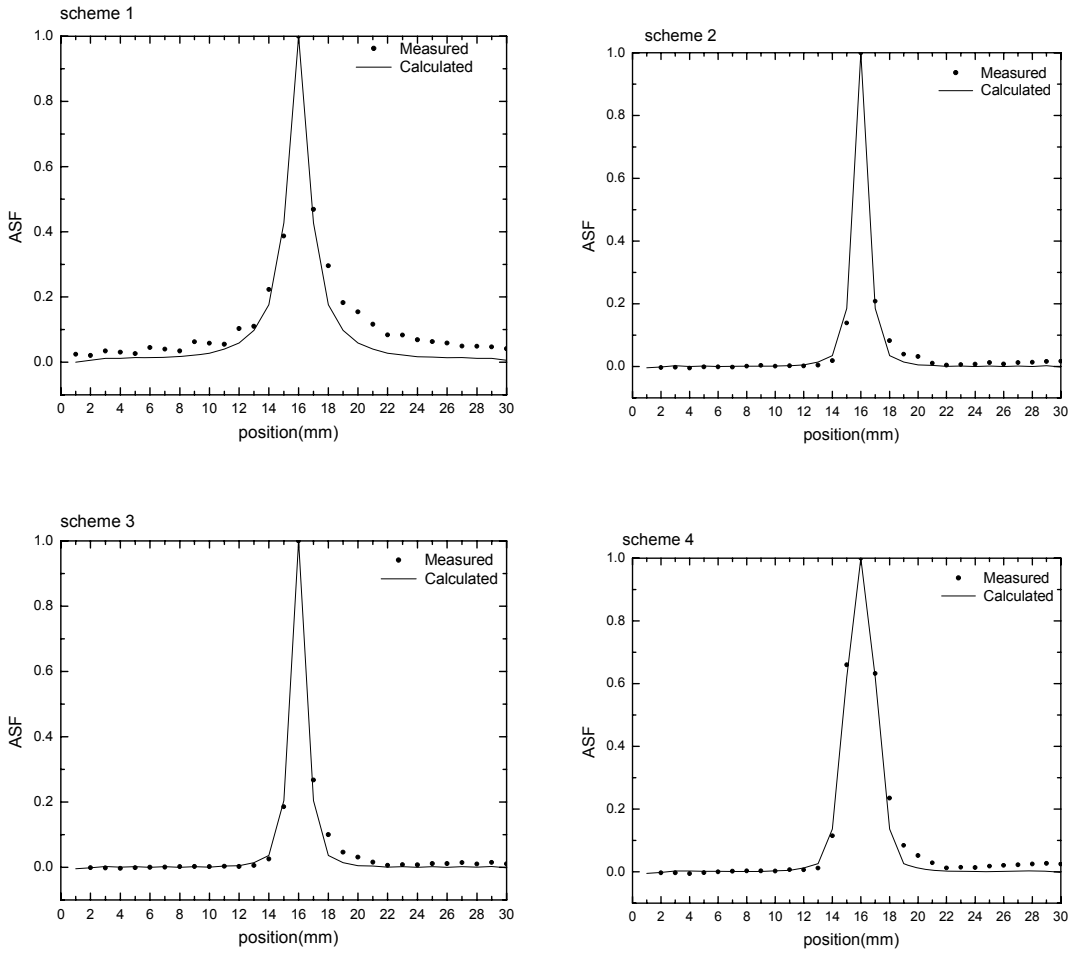

Figure 7.5, ASF measured using BB and calculated from model in four reconstruction schemes. 1) SBP: simple backprojection reconstruction, 2) with Ramp filter only, 3) with Ramp and Hanning filter (A = 1), 4) with Ramp, Hanning filter (A=1) and ST filter (B=0.085)

Chapter 8

Future Work

8.1 Improvements on the model

The modeled in-plane MTF was calculated by integrating the 3-D MTF in z-direction (Chapter 5). This calculation assumes the edge phantom in perfect alignment with the center of the reconstructed slice, however the measured in-plane MTF is usually position (phase) dependent[86, 87]. The phase dependent in-plane MTF will be investigated in future work. The model calculation will follow the phase averaged MTF calculation described for 2-D projection imaging[86].

The ASF model calculation (Chapter 7) was simplified to be a 2-D problem, and the object was approximated by a 2-D disk. In measurement, a 3-D spherical object was used. In future work a 3-D object spectrum will be incorporated into the linear model to fully reveal the dependence of ASF on object shape and size.

8.2 System optimization using SNR of detection tasks

Cascaded linear system analysis has been applied extensively to detector optimization using DQE as the figure of merit (FOM). However DQE alone is not sufficient to predict the system performance for a detection task, or for comparison across different imaging modalities[18]. According to signal detection theory, imaging performance assessment should incorporate the physical characteristics of imaging systems, the imaging task and the observer response. ICRU Report 54 suggested task based imaging performance

evaluation using detectability index[98], which is essentially a form of SNR. For x-ray imaging systems, it is determined by the frequency domain definition of imaging task and the DQE. A 3-D task-based linear system model was developed to calculate the ideal observer SNR for CBCT under signal-known-exactly, background-known-exactly (BKE) condition[99]. The FOM used for evaluation was the detectability index. By incorporating the imaging task function, the linear system model can be used to maximize object detectability through optimization of the reconstruction filters and acquisition parameters. The 3-D task function will incorporate the shape, size and contrast of the object.

8.3 Other aspects

As mentioned in Chapter 6, the ACR phantom used to investigate the image quality of breast tomosynthesis has inherent limitations in the contrast and size of calcifications. Calcification features with attenuation coefficients comparable to actual microcalcifications in the breast are needed for further investigation and optimization of calcification detection with breast tomosynthesis.

Although preliminary results provide strong evidence that mass detection will be improved with breast tomosynthesis over projection mammography, the detection of clustered microcalcifications may not be as good as mammography[100]. One method proposed by Nishikawa et al[101] is to divide the total dose unequally between the views. Specifically, one projection, i.e., the center view, uses at least half of the dose and the remaining dose is divided equally over the rest of the views. Study using computer simulation has proved better detection of the cal features; however this method may not

be practical due to the dynamic range of the detector. Optimal acquisition geometry needs to be investigated. Proposed acquisition geometry includes nonuniform angular spacing and nonuniform exposure distribution per view.

APPENDIX A: Signal and noise propagation through logarithmic transformation

The logarithmic transformation can be regarded as a gain stage. Assuming the NPS of the projection image is S_p, and the average pixel intensity is $k_p = KX$, where X is the entrance exposure and K is the x-ray sensitivity per pixel. The logarithmic transformation changes the mean signal to $k_l = \log(k_p)$. The gain associated with this process is x-ray exposure dependent, and is given by the first derivative of k_l with respect to k_p. :

$$g = \frac{dk_l}{dk_p} = \frac{1}{KX} \tag{A1}$$

Since g depends on exposure, the logarithmic transformation can only be treated as a linear process within a small range of exposure, i.e. for NPS and low contrast signal. The signal and noise power spectra after the gain stage associated with logarithmic transformation are given by:

$$\begin{aligned} \Phi_l(f_r, f_y) &= g\,\Phi_f(f_r, f_y) = \frac{1}{KX}\Phi_f(f_r, f_y) \\ S_l(f_r, f_y) &= g^2\, S_p(f_r, f_y) = \frac{S_p(f_r, f_y)}{(KX)^2} \end{aligned} \tag{A2}$$

Since there is no additional noise associated with the gain stage, the DQE is not degraded.

Bibliography

[1] "Cancer Facts and Figures 2007 " *American Cancer Society,* 2007.

[2] M. J. Yaffe, "Digital Mammography," in *Categorical Courses in Diagnostic Radiology Physics: Physics Aspect in Breast Imaging-Current and Future Considerations*, 1999, pp. 229-238.

[3] A. Karellas, S. Vedantham, and S. Suryanarayanan, "Digital Mammography Image Acquisition Technology," in *Categorical Courses in Diagnostic Radiology Physics: Advances in Breast Imaging: Physics, Technology, and Clinical Applications*, E. b. A. K. a. M. L. Giger, Ed., 2004, pp. 87-101.

[4] J. Yorkston and J. Rowlands, "Flat panel detectors for digital radiography " in *Handbook of Medical Imaging, Volume 1. Physics and Psychophysics* J. B. Edited by Richard L. Van Metter, Harold L. Kundel Ed., 2000, pp. 225-328.

[5] W. Zhao and J. A. Rowlands, "X-ray imaging using amorphous selenium: Feasibility of a flat panel self-scanned detector for digital radiology," *Medical Physics,* vol. 22, pp. 1595-1604, 1995/10/00/ 1995.

[6] J. M. Fitzpatrick and M. Sonka, *Handbook of Medical Imaging, Volume 2. Medical Image Processing and Analysis* vol. 2. Bellingham: SPIE, 2000.

[7] T. Wu, Richard H. Moore, AB, Elizabeth, A. Rafferty, and D.B. Kopans, "Breast Tomosynthesis: Methods and Applications," in *Categorical Courses in Diagnostic Radiology Physics: Advances in Breast Imaging: Physics, Technology, and Clinical Applications*, A. Karellas, and Maryellen L. Giger, Ed., 2004, pp. 149-165.

[8] J. M. Boone, "Breast CT: Its Prospect for Breast Cancer Screening and Diagnosis," in *Categorical Courses in Diagnostic Radiology Physics: Advances in Breast Imaging: Physics, Technology, and Clinical Applications*, E. b. A. K. a. M. L. Giger, Ed., 2004, pp. 165-177.

[9] L. T. Niklason, B. T. Christian, L. E. Niklason, D. B. Kopans, D. E. Castleberry, B. H. Opsahl- Ong, C. E. Landberg, P. J. Slanetz, A. A. Giardino, R. Moore, D. Albagli, M. C. DeJule, P. F. Fitzgerald, D. F. Fobare, B. W. Giambattista, R. F. Kwasnick, J. Liu, S. J. Lubowski, G. E. Possin, J. F. Richotte, C. Y. Wei, and R. F.

Wirth, "Digital tomosynthesis in breast imaging," *Radiology,* vol. 205, pp. 399-406, November 1, 1997 1997.

[10] B. Ren, C. Ruth, J. Stein, A. Smith, I. Shaw, and J. Zhenxue, "Design and performance of the prototype full field breast tomosynthesis system with selenium based flat panel detector," in *Proc. SPIE*, San Diego, CA, USA, 2005, pp. 550-561.

[11] W. Zhao, R. Deych, and E. Dolazzab, "Optimization of Operational Conditions for Direct Digital Mammography Detectors For Digital Tomosynthesis," in *Proc. SPIE*, San Diego, CA, USA, 2005, pp. 1272-1281.

[12] J. T. Dobbins and D. J. Godfrey, "Digital x-ray tomosynthesis: current state of the art and clinical potential," *Physics in Medicine and Biology,* vol. 48, pp. R65-R106, Oct 7 2003.

[13] M. Bissonnette, M. Hansroul, E. Masson, S. Savard, S. Cadieux, P. Warmoes, D. Gravel, J. Agopyan, B. Polischuk, W. Haerer, T. Mertelmeier, J. Y. Lo, Y. Chen, J. T. Dobbins III, J. L. Jesneck, and S. Singh, "Digital breast tomosynthesis using an amorphous selenium flat panel detector," in *Proc. SPIE*, San Diego, CA, USA, 2005, pp. 529-540.

[14] T. Mertelmeier, Jasmina Orman, Wolfgang Haerer, and Mithun K. Dudam "Optimizing filtered backprojection reconstruction for a breast tomosynthesis prototype device " in *Proc. SPIE*, 2006, p. 61420F

[15] J. C. Danty, and Shaw, R, *Image Science, principle, anlyasis and evaluation of photographic-type imaging processing*: Academic Press, 1974.

[16] A. Rose, "The sensitivity performance of the human eye on an absolute scale " *J. Opt. Soc. Am.,* vol. 38, p. 196, 1948.

[17] J. Beutel, Harold L. Kundel, and Richard L. Van Metter *Handbook of Medical Imaging, Volume 1. Physics and Psychophysics*: SPIE, 2000.

[18] R. F. Wagner and D. G. Brown, "Unified SNR analysis of medical imaging systems," *Physics in Medicine and Biology,* vol. 30, pp. 489-518, 1985.

[19] B. Zhao and W. Zhao, "Characterization of a direct full-field flat-panel digital mammography detector," in *Proc. SPIE*, San Diego, CA, USA, 2003, pp. 157-167.

[20] W. Zhao and J. A. Rowlands, "Digital radiology using active matrix readout of amorphous selenium: Theoretical analysis of detective quantum efficiency," *Medical Physics,* vol. 24, pp. 1819-1833, 1997/12/00/ 1997.

[21] W. Zhao, W. G. Ji, and J. A. Rowlands, "Effects of characteristic x rays on the noise power spectra and detective quantum efficiency of photoconductive x-ray detectors," *Medical Physics,* vol. 28, pp. 2039-2049, 2001/10/00/ 2001.

[22] W. Zhao, I. Blevis, S. Germann, J. A. Rowlands, D. Waechter, and Z. Huang, "Digital radiology using active matrix readout of amorphous selenium: Construction and evaluation of a prototype real-time detector," *Medical Physics,* vol. 24, pp. 1834-1843, 1997/12/00/ 1997.

[23] W. Zhao, W. G. Ji, A. Debrie, and J. A. Rowlands, "Imaging performance of amorphous selenium based flat-panel detectors for digital mammography: Characterization of a small area prototype detector," *Medical Physics,* vol. 30, pp. 254-263, 2003.

[24] H. Fujta, D. Tsai, Titoh, K. Doi, J. Morishata, K. Uedo and A. Ohtsuka, "A simple method for determining the modulation transfer function in digital radiography," *IEEE Thans. Medical Imaging,* vol. 11, pp. 34-39, 1992.

[25] R. A. Street, S.E. Ready, L. Melkhov, J. Ho, A. Zuck and B. Breen, "approaching the theoretical x-ray sensitivity with HgI2 direction image sensors," in *Proc. SPIE*, pp. 414-422.

[26] G. Pang, W. Zhao, and J. A. Rowlands, "Digital radiology using active matrix readout of amorphous selenium: Geometrical and effective fill factors," *Medical Physics,* vol. 25, pp. 1636-1646, 1998/09/00/ 1998.

[27] J. A. Seibert, J. M. Boone, K. K. Lindfors, "Flat-field correction technique for digital detectors," *Proc. SPIE,* vol. 3336, pp. 348-354, 1998.

[28] J. P. Moy, "How does real offset and gain correction affect the DQE in images from x-ray flat detectors," *Proc. SPIE,* vol. 3659, pp. 90-97, 1999.

[29] D. L. Lee, Brian Rodricks, Michael G. Hoffberg, Cornell L. Williams, Kelly P. Golden and Lothar S. Jeromin, "Filtered-gain calibration and its effect on frequency-dependent DQE and image quality in Se-based general radiography and full-field mammographic digital imaging," in *Proc. SPIE*, 2001, pp. 121-126

[30] J. T. Dobbins III, D. L. Ergun, L. Rutz, D. A. Hinshaw, H. Blume, and D. C. Clark, "DQE(f) of four generations of computed radiography acquisition devices," *Medical Physics,* vol. 22, pp. 1581-1593, 1995.

[31] M. J. Tapiovaara, R. F. Wagner,, "SNR and DQE analysis of broad spectrum x-ray imaging," *Phys. Med. Biol.,* vol. 30, pp. 519-529 1985.

[32] R. M. Nishikawa, M. J. Yaffe, "Signal-to-noise properties of mammographic film-screen systems," *Med. Phys.,* vol. 12, pp. 32-39, 1985.

[33] E. Samei, M. J. Flynn, H. G. Chotas, J. T. Dobbins, III, "DQE of direct and indirect digital radiographic systems," *Proc. SPIE,* vol. 4320, pp. 189-197 2001.

[34] J. M. Boone, T. R. Fewell, and R. J. Jennings, "Molybdenum, rhodium, and tungsten anode spectral models using interpolating polynomials with application to mammography," *Medical Physics,* vol. 24, p. 1863, 1997.

[35] J. Boone, "Spectral modeling and compilation of quantum fluence inn radiography and mammography," in *Proc, SPIE* 1998, pp. 592-601.

[36] R. M. Nishikawa, G. E. Mawdsley, A. Fenster and M. J. Yaffe, "Scanned-projection digital mammography," *Med. Phys. ,* vol. 14, pp. 717-727, 1987.

[37] W. Zhao, Giovanni DeCrescenzo, and John A. Rowlands "Investigation of lag and ghosting in amorphous selenium flat-panel x-ray detectors " in *Proc. SPIE* 2002, pp. 9-19.

[38] V. Loustauneau, M. Bissonnette, S. Cadieux and M. Hansnouf "Imaging performance of a clinical selenium flat-panel detector for advanced applications in full-field digital mammography," in *SPIE*, 2003, pp. 1010-1020

[39] C. Schroeder, T. Stanescu, S. Rathee and B.G. Fallone, "Lag measurement in an a-Se active matrix flat-panel imager," *Med. Phys.,* vol. 31, pp. 1203-1209, 2004.

[40] S. Steeciw, T. Standescu, S. Rathee and B. G. Fallone, "Sensitivity reduction in biased amorphous selenium photoconductors," *J.Phys D: Appl. Phys,* vol. 35, pp. 2716-2722 2002.

[41] B. Zhao and W. Zhao, "Temporal performance of amorphous selenium mammography detectors," *Medical Physics,* vol. 32, pp. 128-136, 2005/01/00/ 2005.

[42] B. Polischuk and K. W. H. Rougeot, A. Debrie, E. Poliquin, J. P. Martin, T. T. Truong, M. Choquette, L, Laperri and Z. Shuki, "Direct conversion detector for digital mammography," in *Proc, SPIE*, 1999, pp. 417-425.

[43] M. F. Stone, W. Zhao, B. V. Jacak, P. O'Connor, B. Yu, and P. Rehak, "The x-ray sensitivity of amorphous selenium for mammography," *Medical Physics,* vol. 29, pp. 319-324, 2002/03/00/ 2002.

[44] A. Brauers, T. Buchkremer, G. Frings and P. Quaflieg, "charge collection in a Se photoconductor on a thin film transistor array during x-ray imaging," in *Mat. Res. Soc. Proc*, 1997, pp. 919-924.

[45] B. Polischuk, Z. Shukri, A. Legros and H. Rougeot, "Selenium direct converter structure for static and dynamic x-ray detection in medical imaging application," in *Proc. SPIE* 1998, pp. 494-504

[46] D. C. Hunt, S. S. Kirby and J. A. Rowlands, "X-ray imaging with amorphous selenium: X-ray to charge conversion gain and avalanche multiplication gain," *Med. Phys.,* vol. 29, pp. 2464–2471 2002.

[47] S. O. Kasap, *Optoelectronics & Photonics: Principles & Practices* Englewood Cliffs, NJ: Prentice Hall,, 2003.

[48] M. Abkowitz, "Density of states in a-Se from combined analysis of xerographic potentials and transient traport data," *Philos. Mag. Lett. ,* vol. 58, pp. 53-57, 1988.

[49] W. Zhao, G. DeCrescenzo, S. O. Kasap, and J. A. Rowlands, "Ghosting caused by bulk charge trapping in direct conversion flat-panel detectors using amorphous selenium," *Medical Physics,* vol. 32, pp. 488-500, 2005.

[50] S. O. Kasap, M. Z. Kabir, M. Yunus and G. Belev, "Dependence of X-Ray Sensitivity of Direct Conversion Detectors on X-Ray Exposure and Exposure History," in *Proc. SPIE*, 2004, pp. 170-176.

[51] M. Overdick, T. Solf and H. Wischmann, "Temporal artifacts in flat-dynamic x-ray detectors," in *Proc. SPIE*, 2001, pp. 47-58.

[52] F. Busse, W. Rutten, B. Sandkamp, P. L. Alving, R. Bastiaens and T. Ducourant, "Design and performance of a high-quality cardiac flat-panel detector," in *Proc SPIE*, 2002, pp. 819-827.

[53] S. Adachi, N. Hori, K. Sato, S. Tokuda, T. Sato, K. Uehara, Y. Izumi, H. Nagata, Y. Yoshimura and S. Yamada, "Experimental evaluation of a-Se and CdTe flat-panel x-ray detectors for digital radiography and fluoroscopy," in *Proc. SPIE*, 2000, pp. 38-47.

[54] M. Flynn, C. Dodge, D. Peck and A. Swinford, "Optimal radiographic techniques for digital mammograms obtained with an amorphous selenium detector," *Proc. SPIE*, 2003, pp. 147-156.

[55] T. Wu, R. H. Moore, E. A. Rafferty, and D. B. Kopans, "A comparison of reconstruction algorithms for breast tomosynthesis," *Medical Physics,* vol. 31, pp. 2636-2647, 2004/09/00/ 2004.

[56] S. Suryanarayanan, A. Karellas, S. Vedantham, S. P. Baker, S. J. Glick, C. J. D'Orsi, and R. L. Webber, "Evaluation of Linear and Nonlinear Tomosynthetic Reconstruction Methods in Digital Mammography," *Academic Radiology,* vol. 8, pp. 219-224, 2001/3 2001.

[57] J. Zhou, B. Zhao, and W. Zhao, "A computer simulation platform for the optimization of a breast tomosynthesis system," *Medical Physics,* vol. 34, pp. 1098-1109, 2007.

[58] W. Zhao and J. A. Rowlands, "Digital radiology using active matrix readout of amorphous selenium: theoretical analysis of detective quantum efficiency," *Med Phys,* vol. 24, pp. 1819-33, Dec 1997.

[59] J. G. Mainprize, A. K. Bloomquist, M. P. Kempston, and M. J. Yaffe, "Resolution at oblique incidence angles of a flat panel imager for breast tomosynthesis," *Med Phys,* vol. 33, pp. 3159-64, Sep 2006.

[60] G. Hajdok, J. Yao, J. J. Battista, and I. A. Cunningham, "Signal and noise transfer properties of photoelectric interactions in diagnostic x-ray imaging detectors," *Med Phys,* vol. 33, pp. 3601-20, Oct 2006.

[61] W. Que and J. A. Rowlands, "X-ray imaging using amorphous selenium: inherent spatial resolution," *Med Phys,* vol. 22, pp. 365-74, Apr 1995.

[62] E. Samei, M. J. Flynn, and D. A. Reimann, "A method for measuring the presampled MTF of digital radiographic systems using an edge test device," *Medical Physics,* vol. 25, pp. 102-113, 1998.

[63] A.-K. Carton, D. Vandenbroucke, L. Struye, A. D. A. Maidment, Y.-H. Kao, M. Albert, H. Bosmans, and G. Marchal, "Validation of MTF measurement for digital mammography quality control," *Medical Physics,* vol. 32, pp. 1684-1695, 2005.

[64] A. Maidment and M. Albert, "Conditioning data for calculation of the modulation transfer function," *Medical Physics,* vol. 30, pp. 248-253, 2003.

[65] R. L. Weisfield and N. R. Bennett, "Electronic noise analysis of a 127-mu m pixel TFT/photodiode array," in *Proc. SPIE*, San Diego, CA, USA, 2001, pp. 209-218.

[66] A. K. Bloomquist, M. J. Yaffe, E. D. Pisano, R. E. Hendrick, G. E. Mawdsley, S. Bright, S. Z. Shen, M. Mahesh, E. L. Nickoloff, R. C. Fleischman, M. B. Williams, A. D. A. Maidment, D. J. Beideck, J. Och, and J. A. Seibert, "Quality control for digital mammography in the ACRIN DMIST trial: Part I," *Medical Physics,* vol. 33, pp. 719-736, 2006.

[67] J. H. Siewerdsen and D. A. Jaffray, "A ghost story: spatio-temporal response characteristics of an indirect-detection flat-panel imager," *Med Phys,* vol. 26, pp. 1624-41, Aug 1999.

[68] J. H. Siewerdsen and D. A. Jaffray, "Cone-beam computed tomography with a flat-panel imager: Effects of image lag," *Medical Physics,* vol. 26, pp. 2635-2647, 1999.

[69] T. Wu, R. H. Moore, and D. B. Kopans, "Voting strategy for artifact reduction in digital breast tomosynthesis," *Medical Physics,* vol. 33, pp. 2461-2471, 2006.

[70] A. C. Kak, and Malcolm Slaney, *Principles of Computerized Tomographic Imaging* IEEE Press, 1988.

[71] T. Wu, A. Stewart, M. Stanton, T. McCauley, W. Phillips, D. B. Kopans, R. H. Moore, J. W. Eberhard, B. Opsahl-Ong, L. Niklason, and M. B. Williams, "Tomographic mammography using a limited number of low-dose cone-beam projection images," *Medical Physics,* vol. 30, p. 365, 2003.

[72] Y. Chen, J. Y. Lo, and J. T. Dobbins Iii, "Noise power spectrum analysis for several digital breast tomosynthesis reconstruction algorithms," in *Proc. SPIE*, San Diego, CA, USA, 2006, pp. 614259-8.

[73] Y. Chen, J. Y. Lo, and J. T. Dobbins Iii, "Impulse response analysis for several digital tomosynthesis mammography reconstruction algorithms," in *Proc. SPIE*, San Diego, CA, USA, 2005, pp. 541-549.

[74] J. H. Siewerdsen, L. E. Antonuk, Y. El-Mohri, J. Yorkston, W. Huang, J. M. Boudry, and I. A. Cunningham, "Empirical and theoretical investigation of the noise performance of indirect detection, active matrix flat-panel imagers (AMFPIs) for diagnostic radiology," *Medical Physics,* vol. 24, pp. 71-89, 1997.

[75] M. F. Kijewski and A. Judy, "The noise power spectrum of CT images," *Physics in Medicine and Biology,* vol. 32, p. 565, 1987.

[76] K. M. Hanson, "Detectability in computed tomographic images," *Medical Physics,* vol. 6, pp. 441-451, 1979.

[77] J. H. Siewerdsen, I. A. Cunningham, and D. A. Jaffray, "A framework for noise-power spectrum analysis of multidimensional images," *Med Phys,* vol. 29, pp. 2655-71, Nov 2002.

[78] J. H. Siewerdsen and D. A. Jaffray, "Three-dimensional NEQ transfer characteristics of volume CT using direct- and indirect-detection flat-panel imagers," in *Proc. SPIE*, San Diego, CA, USA, 2003, pp. 92-102.

[79] W. Zhao, B. Zhao, P. R. Fisher, P. Warmoes, T. Mertelmeier, and J. Orman, "Optimization of detector operation and imaging geometry for breast tomosynthesis," in *Proc. SPIE*, San Diego, CA, USA, 2007, pp. 65101M-12.

[80] B. Zhao, J. Zhou and W.Zhao, , "Focal spot blur in tomosynthestic systems," in *RSNA* 2005.

[81] S. J. Riederer, N. J. Pelc, and D. A. Chesler, "The noise power spectrum in computed X-ray tomography," *Physics in Medicine and Biology,* pp. 446-454, 1978.

[82] K. Faulkner and B. M. Moores, "Analysis of x-ray computed tomography images using the noise power spectrum and autocorrelation function," *Physics in Medicine and Biology,* vol. 29, pp. 1343-1352, 1984.

[83] M. L. Giger, "Computer-aided Diagnosis in Diagnostic Mammography and Multimodality Breast Imaging," in *RSNA Categorical Course in Diagnostic Radiology Physics: Advances in Breast Imaging—Physics, Technology, and Clinical Applications*, 2004, pp. 205-217.

[84] B. Li, G. B. Avinash, J. W. Eberhard, and B. E. H. Claus, "Optimization of slice sensitivity profile for radiographic tomosynthesis," *Medical Physics,* vol. 34, pp. 2907-2916, 2007.

[85] M. J. Flynn, R. McGee, and J. Blechinger, "Spatial resolution of x-ray tomosynthesis in relation to computed tomography for coronal/sagittal images of the knee," in *Proc. SPIE*, San Diego, CA, USA, 2007, pp. 65100D-9.

[86] J. T. Dobbins III, "Effects of undersampling on the proper interpretation of modulation transfer function, noise power spectra, and noise equivalent quanta of digital imaging systems," *Medical Physics,* vol. 22, pp. 171-181, 1995.

[87] J. A. Segui and W. Zhao, "Amorphous selenium flat panel detectors for digital mammography: Validation of a NPWE model observer with CDMAM observer performance experiments," *Medical Physics,* vol. 33, pp. 3711-3722, 2006.

[88] C. J. Bischof and J. C. Ehrhardt, "Modulation transfer function of the EMI CT head scanner," *Medical Physics,* vol. 4, pp. 163-167, 1977.

[89] J. M. Boone, "Determination of the presampled MTF in computed tomography," *Medical Physics,* vol. 28, pp. 356-360, 2001.

[90] K. Yang, A. L. C. Kwan, and J. M. Boone, "Computer modeling of the spatial resolution properties of a dedicated breast CT system," *Medical Physics,* vol. 34, pp. 2059-2069, 2007.

[91] M. Thornton, M. and Michael J. Flynn "Measurement of the spatial resolution of a clinical volumetric computed tomography scanner using a sphere phantom" in *Proc. SPIE*, 2006, p. 61421Z

[92] G. Avinash, K. Israni, and B. Li, "Characterization of point spread function in linear digital tomosynthesis: a simulation study," in *Proc. SPIE*, San Diego, CA, USA, 2006, pp. 614258-8.

[93] Y. Zhang, H.-P. Chan, B. Sahiner, J. Wei, M. M. Goodsitt, L. M. Hadjiiski, J. Ge, and C. Zhou, "A comparative study of limited-angle cone-beam reconstruction methods for breast tomosynthesis," *Medical Physics,* vol. 33, pp. 3781-3795, 2006.

[94] Y. Zhang, H.-P. Chan, B. Sahiner, J. Wei, J. Ge, L. M. Hadjiiski, and C. Zhou, "Investigation of the Z-axis resolution of breast tomosynthesis mammography systems," in *Proc. SPIE*, San Diego, CA, USA, 2007, pp. 65104A-8.

[95] T. Deller, K. N. Jabri, J. M. Sabol, X. Ni, G. Avinash, R. Saunders, and R. Uppaluri, "Effect of acquisition parameters on image quality in digital tomosynthesis," in *Proc. SPIE*, San Diego, CA, USA, 2007, pp. 65101L-11.

[96] T. Wu, J. Zhang, R. Moore, E. Rafferty, D. Kopans, W. Meleis, and D. Kaeli, "Digital tomosynthesis mammography using a parallel maximum-likelihood reconstruction method," in *Proc. SPIE*, San Diego, CA, USA, 2004, pp. 1-11.

[97] R. Aufrichtig, "Comparison of low contrast detectability between a digital amorphous silicon and a screen-film based imaging system for thoracic radiography," *Medical Physics,* vol. 26, pp. 1349-1358, 1999.

[98] *ICRU Report 54: Medical Imaging-The Assessment of Image Quality* International Commission 1996.

[99] J. H. Siewerdsen and D. A. Jaffray, "Unified iso-SNR approach to task-directed imaging in flat-panel cone-beam CT," in *Proc. SPIE,* San Diego, CA, USA, 2002, pp. 245-254.

[100] J. Y. Lo, S. Singh, J. T. Dobbins Iii, and E. Samei, "MO-D-L100F-03: New Developments in Digital Breast Tomosynthesis," *Medical Physics,* vol. 34, pp. 2518-2518, 2007.

[101] R. M. Nishikawa, I. Reiser, P. Seifi, and C. J. Vyborny, "A new approach to digital breast tomosynthesis for breast cancer screening," in *Proc. SPIE*, San Diego, CA, USA, 2007, pp. 65103C-8.